MOLECULAR SIMULATION OF BULK CARBON DISULPHIDE AND SALT-WATER SOLUTIONS IN BULK AND IN SILICA PORES

A thesis submitted in fulfillment
of the
requirements for the degree of
Doctor of Philosophy

P. A. Pavithra N. Prathiraja
BEng (Mechanical and Aerospace Engineering,
Nagoya University-Japan)

Applied Physics
School of Applied Sciences
College of Science, Engineering and Health
RMIT University
November 13, 2011

Declaration of the Candidate

I certify that except where due acknowledgement has been made, the work is that of the candidate alone. This body of work has not been submitted previously, in whole or in part, to qualify for any other academic award. The content of this thesis is the result of work which has been carried out since the official commencement date of the approved research program. Any editorial work, paid or unpaid, carried out by a third party is acknowledged.

P. A. Pavithra N.

Prathiraja

November 13, 2011

Acknowledgements

This dissertation would not have been possible without the guidance of several individuals, who contributed their valuable time in the preparation and completion of this study. It is a pleasure to thank the many people who made this thesis possible.

First and foremost, I would like to express my utmost gratitude to my supervisor, Professor Peter J. Daivis. His sincerity, encouragement, guidance and support from the beginning to the end, enabled me to develop a deep understanding of the subject. He has been my inspiration, as I overcame all obstacles in the completion of this research work.

I also owe my deepest gratitude to my co-supervisor, Professor Ian Snook, for his detailed and constructive comments, and for his important support throughout this work.

I warmly thank Professor Y. Ishida and Dr Zhang at Nagoya University, Japan for their concern and consideration regarding my academic requirements.

I wish to express my warm and sincere thanks to Professor Asseal for his expertise. Despite the distance, he has painstakingly e-mailed the information I needed.

I gratefully acknowledge the financial support of CSIRO.
I would like to thank the VPAC and RMIT cluster for usage of HPC, and also for their

help and support.

I would like to thank the library staff for making quality information and relevant literature easily accessible on campus. I greatly appreciate their efforts in trying to gather relevant old journals for this work.

My sincere thanks goes to Dr Michelle for the support she gave me when the going was tough (e.g. confused silica). I would also like to thank Dr Akin for help with VMD.

I wish to thank my best friends Dr Michelle, Dr Nevena, Dr Akin and Ms Anjani, in RMIT University for helping me get through the difficult times, and for all the emotional support, camaraderie, entertainment, and caring they provided.

And then there are all the other people who have made RMIT a very special place over my stay there: Tu, Masturina, Chris, Nick, Adrian, Sal, Ben, Patrio, A/Prof. Johan Du Plessis, Danieal, members of condensed matter theory group and members of materials modelling and simulation.

I owe my most sincere gratitude to Professor Julian Gale from Curtin University, Perth and his students who gave me the opportunity to work with them and gave me untiring help during my stay there.

Lastly and most importantly, I would like to express my utmost gratitude to my family. I would like to thank my husband, for creating an environment in which following this path seemed so natural, to my grandmother for her unconditional love and also to my parents who gave birth to me, brought me up, supported me, taught me, and loved me.

My Very Special Parents

I may no longer be that little child who always wanted another hug or minute with you
But I still miss you when we are apart.
I may no longer need your hand for every step I take
But I still need your acceptance and support of everything I do.
I may not be that little child who asked for all the things I ever wanted in the world
But that's because long ago you taught me How to go after my dreams.
I may no longer be that little child who looked to you to share every hurt, smile and tear
But I still feel like that child whenever I think of you
I'll always love you, Mom and Dad,
with the heart of that little child Grown to love you only more.

My Dear Grandma

You have a big heart - And you're quick to forgive
Always thinking of others - And always willing to give
How lucky I am to - Have a grandma like you
Someone who takes an - Interest in all that I do

My Loving Husband

I would be strong - If you are not wrong
I would be independent - If not let me dependent
I might be lazy - If you are not crazy
I might be unwise - If you are not wise

To them I dedicate this thesis ...

Table Of Contents

List of Tables

List of Figures

Chapter 1

Introduction

> There are no such things as applied sciences, only applications of science.
>
> *Louis Pasteur (1822 - 1895)*

Membranes for water purification are used in many applications and different types of membranes are being developed at the moment. No membrane can filter and purify water entirely, but improvements using novel kinds of membranes are still being made. Applications to desalination will continue to generate interest in membrane research at both fundamental and applied levels. The main challenge at the moment is to make membranes applicable to industrial processes which are more energy efficient and potentially much less expensive.

Recently many researchers are doing simulations of silica nano-pores using molecular dynamics to determine the macroscopic thermodynamic properties of porous systems. The realistic pore structures of membranes are not cylindrical and therefore the characteristics of the membrane may differ from pore shape to pore shape. Hence, it is worth while to examine the characteristics of the silica pore when the pore shape is not cylindrical. This

study examines the salt solution behavior in an equilibrated inhomogeneous silica pore system.

First, we used a simple model of linear triatomic molecule (CS_2) to improve our simulation program to include a constraint algorithm that was later used to simulate water molecules. Within this study, we computed the transport properties of CS_2 more accurately than previous studies. We were also able to describe the shear rate dependence of the internal energy and the pressure by a simple three parameter function.

Then we extended our program to calculate the viscosity of bulk water. Even though many papers have been published relating to liquid water models and properties, not many were able to calculate the viscosity accurately. After computing the temperature dependence of the viscosity of bulk water, we also performed molecular simulations to calculate the viscosity of salt solutions which had not been reported previously. Our results for these two systems agreed with existing experimental and simulation results. Here we were able to define a simpler and more accurate formula to predict the temperature dependence of the viscosity and the concentration dependence of the viscosity of salt solutions using existing experimental data.

Finally, we examined salt solutions in silica pores. Many applications of silica materials depend on their surface properties [4], which are largely determined by the functional groups on surfaces through various modification methods. Hydrophilic and hydrophobic functional group concentrations on the silica surfaces are the most important factor when liquid flows through the silica channel [5]. Therefore we change the surface silanol groups and get comparatively hydrophilic and hydrophobic surfaces to examine the characteristics of the equilibrium state. We introduce a new method to generate silica pores with varying pore shape characteristics.

Chapter 2

Simulation methodology

> As our own species is in the process of proving, one cannot have superior science and inferior morals. The combination is unstable and self-destroying.
>
> *- Arthur C. Clarke (1917 - 2008)*

2.1 Introduction

One of the principal tools in the theoretical study of assemblies of molecules in terms of their structure and the microscopic interactions between them is the method of molecular dynamics simulations (MD). This computational method calculates the time dependent behavior of a molecular system. From the microscopic state of the system, i.e. particle positions and momenta, macroscopic properties such as pressure and energy can be evaluated. This method allows one to observe how changes in the microscopic state affect macroscopic properties and vice versa. The main advantage of this method is that we can use it to test and improve existing theories. It may also be helpful to developing new theories too. MD is a very simple and powerful simulation technique that can be used for solving the equations of motion of a system of molecules without any limitations in principle. This technique can also be used to investigate the transport properties of

materials.

The MD simulation accuracy depends on two important factors: the intermolecular potential and the finite difference scheme. The intermolecular force between the particles determines all transport properties such as viscosity and thermal conductivities.

In the first part of this chapter, we discuss a commonly used potential energy calculation method using the Lennard-Jones potential, shear viscosity calculations using Green-Kubo relation and calculation of system temperature of molecular systems. In Section (2.6) we discuss an advanced and more accurate algorithm to calculate rigidly constrained bond lengths and angles. In Section (2.7) we describe a few important components of an MD simulation for molecular systems in both equilibrium and non-equilibrium states. We also describe electrostatic energy and force calculation using Ewald summation and the Wolf method in Section (2.8 and 2.9) respectively.

2.2 Lennard-Jones potential energy function

A form of the potential was first proposed in 1931 by John Edward Lennard-Jones. (He became Lennard-Jones after married Kathleen Lennard in 1926, adding his wife's surname to his own.) The Lennard-Jones potential (also referred to as the L-J potential, 6-12 potential, or 12-6 potential) is a mathematically simple model that approximates the interaction between a pair of neutral atoms or molecules. The Lennard-Jones pair potential function is defined as:

$$\phi(r) = 4\epsilon_{\alpha\beta}\left[\left(\frac{\sigma_{\alpha\beta}}{r}\right)^{12} - \left(\frac{\sigma_{\alpha\beta}}{r}\right)^{6}\right] \tag{2.1}$$

where r is the interatomic separation, $\epsilon_{\alpha\beta}$ is the potential well depth for interactions between species α and species β, and $\sigma_{\alpha\beta}$ is the value of r at which the potential is zero. The LJ potential generally is truncated at some fixed distance r_c (generally known as the

cut-off distance), with $r_c \leq L/2$ and L the length of the simulation cell. These parameters can be fitted to reproduce experimental data or accurate quantum chemistry calculations. Due to its computational simplicity, the Lennard-Jones potential is used extensively in computer simulations even though more accurate potentials exist.

2.3 Lorentz-Berthelot combining rules

Binary Lennard-Jones (LJ) mixtures are of fundamental interest in understanding mixture interactions and their effects upon thermophysical properties. Most studies of LJ mixtures have assumed the Lorentz-Berthelot (LB) combining rules for the cross interaction parameters. It is quite common to use an arithmetic mean for σ (the Lorentz rule) and a geometric mean for ϵ (the Berthelot rule):

$$\sigma_{\alpha\beta} = \frac{1}{2}\left(\sigma_{\alpha\alpha} + \sigma_{\beta\beta}\right) \tag{2.2}$$

$$\epsilon_{\alpha\beta} = \left(\epsilon_{\alpha\alpha}\epsilon_{\beta\beta}\right)^{\frac{1}{2}} . \tag{2.3}$$

2.4 Shear viscosity - Green-Kubo relation

The existence of microscopic local fluctuations in an equilibrated system makes equilibrium molecular dynamics (EMD) a possible way to compute the transport properties. In EMD, computation of the transport coefficients rely on time correlation functions, which can be obtained by measuring the decay of spontaneous fluctuations of the flux or by measuring the accumulated displacements in properties over time (Einstein relations). In this work the shear viscosity was calculated from the Green-Kubo relation.

$$\eta = \frac{V}{10k_BT}\int_0^\infty \left\langle \mathbf{P}^{0s}\left(\tau\right) : \mathbf{P}^{0s}\left(0\right)\right\rangle d\tau \tag{2.4}$$

where $\mathbf{P}^{0s}$ represents the traceless symmetric part of the pressure tensor and the angle brackets denote ensemble averaging over the equilibrium state, V is the volume of the system, and k_B the Boltzmann constant. Note that the factor of 10 appears because we take advantage of the isotropy of the equilibrium state and average over all symmetry-equivalent correlation functions that can be generated from the five independent components of the symmetric traceless stress tensor [6, 7]. This is similar to the way that the heat flux vector is averaged over the three independent correlation functions in Eq. 3.13.

The molecular form of the pressure tensor for molecules with LJ interactions between atoms was calculated using the expression:

$$\mathbf{P}V = \sum_{i=1}^{N_m} \frac{\mathbf{p}_i \mathbf{p}_i}{m_i} - \frac{1}{2} \sum_{i=1}^{N_m} \sum_{\alpha=1}^{N_s} \sum_{j \neq i}^{N_m} \sum_{\beta=1}^{N_s} \mathbf{r}_{ij} \mathbf{F}_{i\alpha j\beta}^{LJ}. \tag{2.5}$$

where $\mathbf{r}_{ij}$ is the minimum image centre of mass separation of molecules i and j, and $\mathbf{F}_{i\alpha j\beta}^{LJ}$ is the LJ force between site α on molecule i and site β on molecule j.
The more complicated electrostatic molecular form of the pressure tensor was calculated using the expression:

$$\mathbf{P}V = \sum_{i=1}^{N_m} \frac{\mathbf{p}_i \mathbf{p}_i}{m_i} - \frac{1}{2} \sum_{i=1}^{N_m} \sum_{\alpha=1}^{N_s} \sum_{j \neq i}^{N_m} \sum_{\beta=1}^{N_s} \mathbf{r}_{ij} \mathbf{F}_{i\alpha j\beta}^{short} + V\mathbf{P}^{(M)e,k} \tag{2.6}$$

where the short range force,

$$\mathbf{F}_{i\alpha j\beta}^{short} = \mathbf{F}_{i\alpha j\beta}^{LJ} + \frac{q_{i\alpha} q_{i\beta} \mathbf{d}_{i\alpha j\beta}}{d_{i\alpha j\beta}^2} \left(\frac{erfc\left(\kappa d_{i\alpha j\beta}\right)}{d_{i\alpha j\beta}} + \frac{2\kappa}{\sqrt{\pi}} exp\left(-\kappa^2 d_{i\alpha j\beta}^2\right) \right) \tag{2.7}$$

and $\mathbf{P}^{(M)e,k}$ is calculated from the Eq.(D.45). Both equations are explained in Appendix D.

2.5 System temperature

The molecular centre of mass kinetic temperature of a system can be defined as:

$$T_M = \frac{1}{k_B N_f} \Sigma_{i=1}^{N} \frac{\mathbf{p}_i^2}{M_i} \tag{2.8}$$

where i indicates the molecule index, M_i is the mass of molecule i, $\mathbf{p}_i = \Sigma \mathbf{p}_{i\alpha}$ is the centre of mass thermal momentum of molecule i, α is the atomic site index on molecule i, and N_f is the number of translational centre-of-mass degrees of freedom, which depends on the total number of constraints on the system. For the molecular systems with no external forces the momentum is conserved and thermal kinetic energy is held constant (one degree of freedom). Therefore the correct N_f for our work is $(3N_m - 4)$, where N_m is number of molecules in the system.

2.6 Constraint algorithm

The models that we have used for simulation have rigidly constrained bond lengths and angles. One way of dealing with this is to solve the equations of motion for the three centre of mass degrees of freedom and the three rotational degrees of freedom directly. This requires a special technique such as the method of quaternions, to solve the rotational equations of motion [8]. Another approach is to solve the equations of motion for each atom, using a constraint method to maintain the rigid-body structure of the molecule.

However, the constraint forces for linear triatomic molecules, such as carbon disulphide (Chapter 3), cannot be evaluated by applying independent distance constraints to the 1-2, 2-3 and 1-3 bonds, because this would lead to 6 unconstrained degrees of freedom for the molecule, rather than the required number, 5. This problem was solved by Ciccotti Ferrario and Ryckaert (CFM) [9], who suggested a method in which the molecule is divided into primary (or basic) particles and secondary particles. The equations of motion are solved for the primary particles, using the forces on all of the atoms, and the positions

of the secondary atoms are found by using the distance constraints and the positions of the primary particles. This method is usually applied in conjunction with the SHAKE or RATTLE constraint algorithms [10] but it is also possible to use the CFM method with "matrix" methods that exactly solve the constraint equations. Baranyai and Evans [11] (BE) have shown how the Edberg, Evans and Morriss (EEM) [12] constraint algorithm can be combined with the CFM method for dealing with molecules that are not fully specified by distance constraints. The BE method has the advantage that the constraint equations are solved exactly apart from numerical error. Numerical error leads to constraint drift, but BE have shown that this drift is easily controlled by a proportional feedback method.

In this work, we have implemented the BE method, because it allows us to solve the constrained equations of motion under equilibrium and nonequilibrium conditions and provides both the positions and the momenta to equal accuracy. The original BE paper contained some minor typographical errors. The main results of their method are briefly reviewed in the Appendix B.1.

2.7 Equation of motion

The central component of molecular dynamics is the solution of the classical equations of motion, which are Newton's Laws. In this section we generalize the atomic and molecular equations of motion to handle both the equilibrium state and non-equilibrium steady state.

2.7.1 Molecular system

In this chapter we describe a few important components of an MD program for a molecular system at equilibrium.

2.7.1.1 Equilibrium molecular dynamics

Molecular dynamics involves allowing a system of N particles to interact through a potential to determine the system's evolution through time. From the microscopic state of the system, i.e. particle positions and momenta, macroscopic properties such as pressure and energy can be evaluated. It allows one to observe how changes on the microscopic level affect macroscopic properties.

The equations of motion for equilibrium molecular dynamics simulation of a fluid can be written as two separate first order differential equations as follows,

$$\dot{\mathbf{r}}_{i\alpha} = \frac{\mathbf{p}_{i\alpha}}{m_{i\alpha}} \tag{2.9}$$

$$\dot{\mathbf{p}}_{i\alpha} = \mathbf{F}_{i\alpha}^{LJ} + \mathbf{F}_{i\alpha}^{C} - \zeta_M \frac{m_{i\alpha}}{M_i}\mathbf{p}_i. \tag{2.10}$$

Where, $\mathbf{r}_{i\alpha}$ are the atomic positions and $\mathbf{p}_{i\alpha}$ are the thermal momentum of site α of molecule i, $m_{i\alpha}$ is the site mass of a molecule i, M_i is the mass of the molecule i and ζ_M is the thermostating multiplier (Section: 2.7.2). Force superscripts 'LJ' and 'C' denote, respectively, Lennard-Jones pair forces and bond length constraint forces B.6 (more details in Appendix B.1).

2.7.1.2 Non-equilibrium molecular dynamics

The SLLOD equations of motion for non-equilibrium molecular dynamics simulations [12, 13] of flowing molecular fluids are given by:

$$\dot{\mathbf{r}}_{i\alpha} = \frac{\mathbf{p}_{i\alpha}}{m_{i\alpha}} + \mathbf{r}_i \cdot \nabla \mathbf{v} \tag{2.11}$$

$$\dot{\mathbf{p}}_{i\alpha} = \mathbf{F}_{i\alpha}^{LJ} + \mathbf{F}_{i\alpha}^{C} - \frac{m_{i\alpha}}{M_i}\mathbf{p}_i \cdot \nabla \mathbf{v} - \zeta_M \frac{m_{i\alpha}}{M_i}\mathbf{p}_i \tag{2.12}$$

where the subscript $i\alpha$ indicates site α on molecule i for the velocity ($\dot{\mathbf{r}}_{i\alpha}$), the momentum ($\dot{\mathbf{p}}_{i\alpha}$), site mass ($m_{i\alpha}$) and the components of the forces ($\mathbf{F}_{i\alpha}$). As discussed before the force superscripts "LJ" and "C" denote Lennard-Jones pair forces and bond length constraint forces respectively. M_i is the molecular mass and ζ_M is the molecular thermostat multiplier for the non-equilibrium state (Section: 2.7.2).

The magnitude of the streaming component of the velocity is determined by the position of the molecular center of mass using $\mathbf{r}_i \cdot \nabla \mathbf{v}$, where the center of mass, $\mathbf{r}_i$ is given by:

$$\mathbf{r}_i = \frac{\sum_{\alpha=1}^{n_c} m_{i\alpha} \mathbf{r}_{i\alpha}}{\sum_{\alpha=1}^{n_c} m_{i\alpha}}. \tag{2.13}$$

The centre of mass momentum of the molecule is given by:

$$\mathbf{p}_i = \sum_{\alpha=1}^{n_c} \mathbf{p}_{i\alpha}. \tag{2.14}$$

2.7.2 Thermostat multiplier

All the simulations have been carried out at a constant temperature. Therefore we use a thermostat multiplier, ζ_M, to keep the kinetic energy constant. We can use either a molecular thermostat multiplier (which thermostats only the center of mass of each molecule) or an atomic thermostat multiplier (which thermostats every single atom on every single molecule) to thermostat a molecular system. In our simulation we use a Gaussian thermostat multiplier for the molecular equations of motion to fix the kinetic energy of the system which is well explained by Evans and Morriss [13, 14]. The thermostat multiplier for the molecular systems can be determined by:

$$\zeta_M = \frac{\sum_{i=1}^{N_m} \left(\mathbf{F}_i \cdot \mathbf{p}_i - \mathbf{p}_i \cdot \nabla \mathbf{v} \cdot \mathbf{p}_i \right) / M_i}{\sum_{i=1}^{N_m} \mathbf{p}_i^2 / M_i}. \tag{2.15}$$

where $\mathbf{F}_i = \sum_{\alpha=1}^{n_c} \mathbf{F}_{i\alpha}$. This sum involves only intermolecular forces; the constraint forces

sum to zero.

In the equilibrium simulations, $\nabla \mathbf{v} = 0$, and for the planar shear non-equilibrium simulations, it is given by:

$$\nabla \mathbf{v} = \begin{bmatrix} 0 & 0 & 0 \\ \dot{\gamma} & 0 & 0 \\ 0 & 0 & 0 \end{bmatrix}. \tag{2.16}$$

2.8 Ewald summation

In condensed matter calculations and simulations, one of the most frequently occurring problems is the evaluation of the Coulomb potential, involving the slowly convergent r^{-1} summation. Paul Peter Ewald, proposed a method [15] which made the calculation feasible for any periodic system and has long been the most used for evaluating energies, forces, and stresses in the simulation of liquids and solids [15].
This section is based on unpublished notes of Daivis [16], and the books by Heyes and Allen and Tildesley [10] and also by Wheeler and Rowley [17]

The total electrostatic potential energy for each simulation box is given by the sum over all pairs of particles in the infinite periodic system, excluding interactions between a particle and itself.

$$\Phi^e = \frac{1}{2} \sum \prime_{n=-\infty}^{\infty} \left(\sum_{i=1}^{N} \sum_{j=1}^{N} \frac{q_i q_j}{|\mathbf{r}_{ij} + \mathbf{L_n}|} \right) \tag{2.17}$$

The vector, $\mathbf{n}$ denoting the position of the unit cell is given by:

$$\mathbf{L}_n = n_x L_x \mathbf{i} + n_y L_y \mathbf{j} + n_z L_z \mathbf{k} \tag{2.18}$$

where the unit vectors $\mathbf{i}, \mathbf{j}, \mathbf{k}$ are directed along x, y, z directions, the corresponding cell side-lengths are, L_γ, and the integers n_x, n_y, n_z range over $0, \pm 1, \pm 2, \ldots, \pm \infty$ to span

the entire lattice. This summation is very slowly convergent and it cannot be accurately computed by truncating to nearest image interactions only. In addition, the infinite sum is conditionally convergent, which means that the result may depend on the order in which the terms are added [18]. Therefore, special methods must be used to compute the sum.

The most common method is the Ewald summation [15]. The Ewald summation method expresses the original sum as two sums. One of these is rapidly convergent in real space and the other is rapidly convergent in reciprocal space.

For a polyatomic molecular fluid, the real space component is:

$$\Phi^r = \sum_{i=1}^{N_m} \sum_{\alpha=1}^{N_{s,i}} \sum_{j>i}^{N_m} \sum_{\beta=1}^{N_{s,i}} \frac{q_{i\alpha} q_{j\beta}}{d_{i\alpha j\beta}} erfc\left(\kappa d_{i\alpha j\beta}\right) \tag{2.19}$$

Note that interactions between different sites on the same molecule are excluded because we consider only small molecules with constraints between all sites. For larger molecules, another term allowing for intramolecular interactions would need to be included. For larger values of κ, the step of the complementary error function becomes more clearer and the real space part of the energy becomes shorter ranged.
The Fourier space term is given by:

$$\Phi^{e,F} = \Phi^f - \Phi^s - \Phi^b \tag{2.20}$$

$$2\Phi^f = \frac{4\pi}{V} \sum_{k\neq 0}^{\infty} k^{-2} exp\left[-k^{-2}/4\kappa^2\right] \left| \sum_{i=1}^{N_m} \sum_{\alpha=1}^{N_{s,i}} q_{i\alpha} exp\left(i\mathbf{k}\cdot\mathbf{r}_{i\alpha}\right) \right|^2 \tag{2.21}$$

$$\Phi^s = \frac{\kappa}{\sqrt{\pi}} \sum_{i=1}^{N_m} \sum_{\alpha=1}^{N_{s,i}} q_{i\alpha}^2 \tag{2.22}$$

$$\Phi^b = \sum_{i=1}^{N_m} \sum_{\alpha=1}^{N_{s,i}} \sum_{\beta>\alpha}^{N_{s,i}} \frac{q_{i\alpha} q_{i\beta}}{d_{i\alpha i\beta}} erf\left(\kappa d_{i\alpha i\beta}\right) \tag{2.23}$$

The first term is in an inconvenient form for computation of the heat flux vector, because we need to use the contribution of each atom to the internal energy in the heat flux vector. A more convenient form is found by expressing the complex modulus in the Fourier term as:

$$\left| \sum_{i=1}^{N_m} \sum_{\alpha=1}^{N_{s,i}} q_{i\alpha} exp\left(i\mathbf{k}\cdot\mathbf{r}_{i\alpha}\right) \right|^2 = \sum_{i=1}^{N_m} \sum_{\alpha=1}^{N_{s,i}} q_{i\alpha} exp\left(-i\mathbf{k}\cdot\mathbf{r}_{i\alpha}\right) \sum_{j=1}^{N_m} \sum_{\beta=1}^{N_{s,i}} q_{j\beta} exp\left(i\mathbf{k}\cdot\mathbf{r}_{j\beta}\right) \tag{2.24}$$

$$= \sum_{i=1}^{N_m} \sum_{\alpha=1}^{N_{s,i}} q_{i\alpha} Re\left[exp\left(-i\mathbf{k}\cdot\mathbf{r}_{i\alpha}\right) \sum_{j=1}^{N_m} \sum_{\beta=1}^{N_{s,i}} q_{j\beta} exp\left(i\mathbf{k}\cdot\mathbf{r}_{j\beta}\right) \right] \tag{2.25}$$

where we have used the fact that:

$$Im\left[\sum_{i=1}^{N_m} \sum_{\alpha=1}^{N_{s,i}} q_{i\alpha} exp\left(-i\mathbf{k}\cdot\mathbf{r}_{i\alpha}\right) \sum_{j=1}^{N_m} \sum_{\beta=1}^{N_{s,i}} q_{j\beta} exp\left(i\mathbf{k}\cdot\mathbf{r}_{j\beta}\right) \right] = 0 \tag{2.26}$$

A further simplification can be made by using the symmetry of the Fourier term with respect to inversion of $\mathbf{k}$. Then only half of the terms need to be computed, and the result is multiplied by two to get the final result. The final result, as it is computed, is:

$$\Phi^f = \frac{2\pi}{V} \sum_{k\neq 0}^{\infty} k^{-2} exp\left[-k^{-2}/4\kappa^2\right] \sum_{i}^{N_m} \sum_{\alpha}^{N_{s,i}} q_{i\alpha} Re\left[exp\left(-i\mathbf{k}\cdot\mathbf{r}_{i\alpha}\right) \sum_{j=1}^{N_m} \sum_{\beta=1}^{N_{s,i}} q_{j\beta} exp\left(i\mathbf{k}\cdot\mathbf{r}_{j\beta}\right) \right] \tag{2.27}$$

where the sum over wavevectors now only goes over those nonzero wavevectors with pos-

itive x-components.

The first self-energy term (Eq.2.22) accounts for the fact that the Fourier space energy includes the interaction energy between the Gaussian charge distribution and itself. These interactions should be excluded, because any given charge is not allowed to interact with itself. Such interactions are already excluded in the real space term. The second self-energy term (Eq.2.23-the self-bonded term) accounts for the fact that the Fourier space energy also includes the energy of interactions between bonded pairs of atoms within a molecule and atoms interacting through bending and dihedral potential energy functions. These electrostatic interactions are normally excluded. The real space term excludes them through a molecular interaction mask, but this does not apply to the Fourier space term, so a correction must be added.

The real space contribution to the force on site α of molecule i due to interactions with other charged sites is given by:

$$\mathbf{F}_{i\alpha}^{e,r} = \sum_{j}^{N} \sum_{\beta=1}^{N_{s,j}} \frac{q_{i\alpha} q_{i\beta} \mathbf{d}_{i\alpha j\beta}}{d_{i\alpha j\beta}^2} \left(\frac{erfc\left(\kappa d_{i\alpha j\beta}\right)}{d_{i\alpha j\beta}} + \frac{2\kappa}{\sqrt{\pi}} exp\left(-\kappa^2 d_{i\alpha j\beta}^2\right) \right) \tag{2.28}$$

The Fourier space term is:

$$\mathbf{F}_{i\alpha}^{e,k} = -\frac{4\pi}{V} \sum_{k\neq 0}^{\infty} \mathbf{k} k^{-2} exp\left[\frac{-k^2}{4\kappa^2}\right] q_{i\alpha} Im\left[exp\left(-i\mathbf{k}\cdot\mathbf{r}_{i\alpha}\right) \sum_{j=1}^{N_m} \sum_{\beta=1}^{N_{s,i}} q_{j\beta} exp\left(i\mathbf{k}\cdot\mathbf{r}_{j\beta}\right) \right] \tag{2.29}$$

Again, a correction to allow for non-interacting bonded atoms within a molecule must be added [17].

$$\mathbf{F}_{i\alpha}^{e,b} = -\sum_{\beta\in bonded}^{N_{s,j}} \frac{q_{i\alpha} q_{i\beta} \mathbf{d}_{i\alpha j\beta}}{d_{i\alpha j\beta}^2} \left(\frac{erfc\left(\kappa d_{i\alpha j\beta}\right)}{d_{i\alpha j\beta}} - \frac{2\kappa}{\sqrt{\pi}} exp\left(-\kappa^2 d_{i\alpha j\beta}^2\right) \right) \tag{2.30}$$

where $d_{i\alpha j\beta}$ is the minimum image separation of atoms $i\alpha$ and $j\beta$,

$$d_{i\alpha j\beta} = min(r_{j\beta} - r_{i\alpha}). \tag{2.31}$$

The summation extends over bonded sites within the same molecule. There is no contribution to the force made by the self-interaction term for the same sites because the potential energy term does not depend on the positions.

The Fourier series term of pressure tensor is given by:

$$V\mathbf{P}^{(M)e,k} = \sum_{k\neq 0}^{\infty} \phi_n \mathbf{B}_n - \sum_{i}^{N_m} \sum_{\alpha}^{N_{s,i}} \mathbf{r}_{i\alpha} \mathbf{F}_{i\alpha}^{e,k} - \sum_{i}^{N_m} \sum_{\alpha}^{N_{s,i}} \mathbf{r}_i \mathbf{F}_{i\alpha}^{e,k} \tag{2.32}$$

ϕ_n and $\mathbf{B}_n$ are defined in the Eq. D.42,and D.47 respectively.

2.8.1 Evaluation and optimization of the parameters

Eq. (2.28) gives the real space contribution to the force on site α of molecule i due to interactions with other charged sites and the Eq. (2.29) represent the reciprocal space term. The reciprocal space vectors $\mathbf{k}$ are defined with respect to the matrix of basis vectors $\mathbf{n}$ as:

$$\mathbf{k} = 2\pi(\mathbf{n}^{-1})^t \begin{pmatrix} L_x \\ L_y \\ L_z \end{pmatrix}, \tag{2.33}$$

In practice, the number of reciprocal space vectors included in the summation is limited by a judicious choice of κ, and by the use of an upper bound, k_{max}, i.e. $(k_x^2 + k_y^2 + k_z^2) \leq k_{max}^2$.

The Ewald convergence parameter κ depends on the complementary error function, and

the minimum image separation vector of two atoms $d_{i\alpha j\beta}$. It is understood from the $erfc(x)$ function behavior that x has to be greater than or equal to 2 for the complementary function to approach zero. Therefore we can say:

$$\kappa r_{cut} \geq 2. \tag{2.34}$$

Therefore the Ewald convergence parameter κ is chosen such that the screening is sufficiently large to ensure that only particles in the primary box need to be considered when calculating the real space sum.

2.9 Wolf method

The above mentioned Ewald method assumes that the considered system is periodically replicated. The Wolf method presented a new method for evaluating the Coulomb potential [19]. It provides an efficient method for the simulation which can cope with the problem of non-periodic systems and at the same time to increases the computational efficiency [20]. This method has been validated by simulations of crystals, liquids, and interfacial systems, such as free surfaces and grain boundaries [20–22].

The Wolf summation equation is given by:

$$\begin{aligned}\Phi^{Wolf} = \frac{1}{2}\sum_{i=1}^{N}\sum_{j\neq i, r_{ij}<R_c}\frac{q_i q_j}{d_{ij}}\left(erfc\left(\kappa d_{ij}\right)\right) - \lim_{r_{ij}\to R_c}\frac{q_i q_j}{r_{ij}}\left(erfc\left(\kappa d_{ij}\right)\right) \\ - \left(\frac{\left(erfc\left(\kappa d_{ij}\right)\right)}{2R_c} + \frac{\kappa}{\sqrt{\pi}}\right)\sum_{i=1}^{N} q_i^2.\end{aligned} \tag{2.35}$$

The last term in Eq. (2.35) is a self-energy associated with each ion i. Recently Zahn et al. [23] investigated a modified form of this summation to use in simulation involving water. Their method can be evaluated as a sum of two parts. The first part is the damped

interaction, the same as for the Ewald summation method:

$$\Phi_{Wolf}^{e,r} = \sum_{i=1}^{N}\sum_{\alpha=1}^{N_s}\sum_{j>i}^{N}\sum_{\beta=1}^{N_s}\frac{q_{i\alpha}q_{j\beta}}{d_{i\alpha j\beta}}erfc\left(\kappa d_{i\alpha j\beta}\right). \tag{2.36}$$

The second part consists of three terms:

$$\Phi_{Wolf}^{e,c} = \sum_{i=1}^{N}\sum_{\alpha=1}^{N_s}\sum_{j>i}^{N}\sum_{\beta=1}^{N_s}q_{i\alpha}q_{j\beta}\left[-\frac{erfc\left(\kappa r_c\right)}{r_c}+\left(\frac{erfc(\kappa r_c)}{r_c^2}+\frac{2\kappa}{\sqrt{\pi}}\frac{exp(-\kappa^2 r_c^2)}{r_c}\right)\left(d_{i\alpha j\beta}-r_c\right)\right], \tag{2.37}$$

where $d_{i\alpha j\beta} \leq r_c$.

The derivative of the above potential will lead to the following forces:

$$\begin{aligned}\mathbf{F}_{Wolf}^{e,c} = \sum_{i=1}^{N}\sum_{\alpha=1}^{N_s}\sum_{j>i}^{N}\sum_{\beta=1}^{N_s}q_{i\alpha}q_{j\beta}\Bigg[&\left(\frac{erfc\left(\kappa d_{i\alpha j\beta}\right)}{d_{i\alpha j\beta}^2}+\frac{2\kappa}{\sqrt{\pi}}\frac{exp(-\kappa^2 R_c^2)}{R_c}\right)\\ &-\left(\frac{erfc\left(\kappa R_c\right)}{R_c^2}+\frac{2\kappa}{\sqrt{\pi}}\frac{exp(-\kappa^2 R_c^2)}{R_c}\right)\Bigg],\end{aligned} \tag{2.38}$$

2.9.1 Pressure tensor and heat flux vector in the Wolf method

Since the electrostatic force is reduced to a relatively short-ranged pair force, there is no need for complicated corrections to the pressure tensor and heat flux vector. The usual expressions for the pressure tensor and heat flux vector in the atomic and molecular representations for potentials that obey the minimum image convention can then be used.

Chapter 3

Shear viscosity and thermal conductivity of liquid carbon disulphide

> The important thing in science is not so much to obtain new facts as to discover new ways of thinking about them.
>
> *Sir William Bragg (1862 - 1942)*

3.1 Introduction

Carbon disulphide is an example of a linear triatomic molecule, which is expected to have different dynamic behaviour from that of spherical molecules such as argon, methane and carbon tetrachloride, due to the effects of its orientational degrees of freedom.

Several molecular dynamics investigations of the transport properties of CS_2 have been published previously. In 1981, Tildesley and Madden [1] developed a model for CS_2 that they used for computations of the equilibrium properties. This model was used in 1983 [24] to study the centre of mass, angular velocity and transverse momentum current au-

tocorrelation functions (acfs). They found that there was evidence of significant coupling between the translational and rotational degrees of freedom in the transverse momentum current acf, and that at short times, the translational diffusion of a CS_2 molecule is anisotropic, but this anisotropy decays due to molecular reorientation and the diffusion is isotropic at long times.

Stassen and Steele [25] computed the stress acf for liquid CS_2 at several state points and found that at long times, the stress acf behaves similarly to that of liquid argon at a corresponding state. They also found that various correlation functions formed from components of the stress such as the kinetic and potential parts, and further splitting the potential component into attractive and repulsive parts, all behaved similarly to those for liquid argon, apart from small, short time effects due to molecular reorientation. Due to the restricted integration limits of their stress acfs, inaccurate values of the shear viscosity were obtained for their two lowest temperature state points. At room temperature the total decay of the acfs was captured within the upper time limit of their stress acfs (10 ps) and their viscosity value was within about 5% of the experimental value. At a higher temperature the agreement was worse.

A semiempirical correlation for the transport coefficients of fluids of small, nonspherical molecules based on the rough hard sphere model has been developed by Assael et al. [26]. This correlation accounts for the effect of translational-rotational coupling by including a roughness factor in the expressions for the transport coefficients. The roughness factor has a different value for each property, but these values are independent of the temperature and density. This correlation was first applied to a series of n-alkanes, but in a subsequent paper, it was successfully applied to experimental data for the self diffusion coefficient, viscosity and thermal conductivity of a variety of fluids including CS_2 [27]. Only two molecular parameters are required in this correlation, a characteristic volume, and a roughness factor. The success of this correlation in correlating diffusion, viscosity and thermal conductivity shows that it is not necessary to explicitly account for the effect

of attractive forces in this model, although they may be implicitly included by adjusting the volume parameter. This simplicity makes the model a very attractive tool for the prediction of transport coefficients.

In this work, we compute the viscosity and thermal conductivity of the Tidesley-Madden (TM) model of carbon disulphide to high precision in a low temperature (193 K) liquid state near the liquid-vapour coexistence curve and a high temperature (309 K) liquid state. We compare the results with the predictions of the correlation developed by Assael et al. [27]. This enables us to validate our simulation technique for a linear triatomic molecule, which uses a bond constraint algorithm unlike the rigid-body algorithm used by Tildesley and Madden. We compare the results of non-equilibrium simulations with those of equilibrium simulations, and also investigate the methods for obtaining the zero shear rate viscosity from the non-linear rheological data.

3.2 Molecular model

In the molecular fluid studied, the intermolecular interaction is given by the Lennard-Jones potential energy function. i.e.

$$\phi(r) = \begin{cases} 4\epsilon_{\alpha\beta}\left[\left(\frac{\sigma_{\alpha\beta}}{r}\right)^{12} - \left(\frac{\sigma_{\alpha\beta}}{r}\right)^{6}\right] & r \leq r_c \\ 0, & r > r_c \end{cases} \tag{3.1}$$

where r is the interatomic separation, $\epsilon_{\alpha\beta}$ is the potential well depth for interactions between species α and species β, and $\sigma_{\alpha\beta}$ is the value of r at which the unshifted potential is zero. Because we have two distinct types of interaction sites, $\alpha\beta$ could be CC, SS or CS for the carbon-carbon, sulphur-sulphur and carbon-sulphur interactions respectively.

We use Tildesley and Madden's liquid state pair potential for carbon disulphide (their model A) [1, 24], which accurately reproduces the structure and several time dependent

properties of liquid CS_2 along the orthobaric curve. The Lennard-Jones potential parameters of this model of CS_2 are shown in Table 3.1.

Table 3.1: Lennard-Jones energy and length parameters in Eq. (3.1) for CS_2 [1]

σ_{cc}	3.35 Å
σ_{cs}	3.44 Å
σ_{ss}	3.52 Å
ϵ_{cc}/k_B	51.20 K
ϵ_{cs}/k_B	96.80 K
ϵ_{ss}/k_B	183.0 K

The LJ potential is truncated at 8.8 Å and the bond length is rigidly constrained to a constant value of 1.57 Å [1]. The calculations of the potential energy and pressure include a tail correction which estimates the contributions from pairs of particles whose separation is greater than the cut-off. All other quantities are uncorrected.

3.3 Simulation methodology

3.3.1 Equations of motion and constraint algorithm

The model of carbon disulphide that we have used has rigidly constrained bond lengths and angles. As described in Chapter 2 we used a constraint method to maintain the rigid-body structure of the molecule in which the molecule is divided into primary (or basic) particles and secondary particles. The equations of motion are solved for the primary particles, using the forces on all of the atoms, and the positions of the secondary atoms are found by using the distance constraints and the positions of the primary particles.

The equations of motion for the basic particles can be written as

$$\dot{\mathbf{r}}_{i\alpha} = \frac{\mathbf{p}_{i\alpha}}{m_{i\alpha}} + \mathbf{r}_i \cdot \nabla \mathbf{v} \tag{3.2}$$

$$\dot{\mathbf{p}}_{i\alpha} = \mathbf{F}^{LJ}_{i\alpha} + \mathbf{F}^{C}_{i\alpha} - \frac{m_{i\alpha}}{m_i}\mathbf{p}_i \cdot \nabla\mathbf{v} - \zeta_M \frac{m_{i\alpha}}{m_i}\mathbf{p}_i \tag{3.3}$$

where $\mathbf{r}_{i\alpha}$ is the position of particle α of molecule i, $\mathbf{p}_{i\alpha}$ is the thermal momentum of particle α of molecule i, $\mathbf{r}_i$ and $\mathbf{p}_i$ are the position and thermal momentum of the centre of mass of molecule i and $m_{i\alpha}$ and m_i are the particle and molecular masses respectively. The total constraint force on particle α of molecule i consists of two terms. The first term is the sum of the direct constraint forces due to other basic particles and the second term is the sum of the constraint forces due to secondary particles:

$$\mathbf{F}^{C}_{i\alpha} = \sum_{\delta=1}^{n_c} M_{i\alpha\delta} \left(\lambda\mathbf{R}\right)_\delta - \sum_{\gamma=1}^{n_s} C_{\gamma\alpha}\boldsymbol{\mu}_\gamma. \tag{3.4}$$

The index δ has now been redefined to run over all constraints between the basic particles within molecule i, consistent with the notation of EEM. The second term on the right hand side of Eq. (3.4) accounts for the forces on basic particle α of molecule i due to the secondary particles in the same molecule.

It is not necessary to solve the equations of motion for the secondary particles, because their positions and momenta are obtained from Eq. (B.2). However, they are given here for completeness:

$$\dot{\mathbf{r}}'_{i\gamma} = \frac{\mathbf{p}'_{i\gamma}}{m_{i\gamma}} + \mathbf{r}_i \cdot \nabla\mathbf{v} \tag{3.5}$$

$$\dot{\mathbf{p}}'_{i\gamma} = \mathbf{F}'^{LJ}_{i\gamma} + \boldsymbol{\mu}_{i\gamma} - \frac{m_{i\gamma}}{M_i}\mathbf{p}_i \cdot \nabla\mathbf{v} - \zeta_M \frac{m_{i\gamma}}{M_i}\mathbf{p}_i \tag{3.6}$$

where $\gamma = 1, \cdots, n_s$.

The constraint multipliers λ are obtained by solving a set of linear equations for each molecule. This can be done very efficiently by using linear equation solvers optimised for sparse matrices, as described in the Appendix B.1. The expression for the constraint

forces on the secondary particles $\boldsymbol{\mu}$ is also given in the Appendix B.1. The thermostat multiplier [14] for the molecular centre of mass translational kinetic thermostat is described in Section: 2.7.2.

$$\zeta_M = \frac{\sum_{i=1}^{N_m} \left(\mathbf{F}_i \cdot \mathbf{p}_i - \mathbf{p}_i \cdot \nabla \mathbf{v} \cdot \mathbf{p}_i\right) / m_i}{\sum_{i=1}^{N_m} \mathbf{p}_i^2 / m_i}. \tag{3.7}$$

In the equilibrium simulations, $\nabla \mathbf{v} = 0$, and for the planar shear non-equilibrium simulations, it is given by:

$$\nabla \mathbf{v} = \begin{bmatrix} 0 & 0 & 0 \\ \dot{\gamma} & 0 & 0 \\ 0 & 0 & 0 \end{bmatrix} \tag{3.8}$$

3.4 Shear viscosity and molecular pressure tensor

In the equilibrium simulations, the shear viscosity was calculated from the Green-Kubo relation:

$$\eta = \frac{V}{10 k_B T} \int_0^\infty \left\langle \mathbf{P}^{0s}(\tau) : \mathbf{P}^{0s}(0) \right\rangle d\tau \tag{3.9}$$

where $\mathbf{P}^{0s}$ represents the traceless symmetric part of the pressure tensor and the ensemble average is performed in the equilibrium state. Note that the factor of 10 appears because we take advantage of the isotropy of the equilibrium state and average over all symmetry-equivalent correlation functions that can be generated from the five independent components of the symmetric traceless stress tensor [6, 7]. This is similar to the way that the heat flux vector is averaged over the three independent correlation functions in Eq. 3.13.

The molecular form of the pressure tensor was calculated using the expression:

$$\mathbf{P}V = \sum_{i=1}^{N_m} \frac{\mathbf{p}_i \mathbf{p}_i}{m_i} - \frac{1}{2} \sum_{i=1}^{N_m} \sum_{\alpha=1}^{N_s} \sum_{j \neq i}^{N_m} \sum_{\beta=1}^{N_s} \mathbf{r}_{ij} \mathbf{F}_{i\alpha j\beta}^{LJ}. \tag{3.10}$$

3.5 Non-Newtonian viscosity and first normal stress

In the non-equilibrium simulations, the shear rate was set to a non-zero value and the pressure tensor was calculated in the non-equilibrium shearing steady state. In the geometry used, P_{yx} and P_{xy} are related to the shear rate by:

$$\left\langle \frac{P_{yx} + P_{xy}}{2} \right\rangle = -\eta\dot{\gamma}. \tag{3.11}$$

The first normal stress coefficient is a result of the restoring forces that act against the anisotropy induced by the shear field. It is defined by:

$$\Psi_1 (\dot{\gamma}) = \frac{P_{yy} - P_{xx}}{\dot{\gamma}^2}. \tag{3.12}$$

Experimentally, the first normal stress coefficient,Ψ_1, is observed to approach a constant value as shear rate approaches zero.

3.6 Thermal conductivity and molecular heat flux vector

The thermal conductivity λ is usually evaluated from a Green-Kubo (GK) time-correlation relation by measuring the regression of equilibrium fluctuations of the heat flux. The expression for the thermal conductivity is given by:

$$\lambda = \frac{V}{3k_B T^2} \int_0^\infty dt \, \langle \mathbf{J}_q (t) \cdot \mathbf{J}_q (0) \rangle \tag{3.13}$$

where V is volume, T is absolute temperature, k_B is the Boltzmann constant, and $\mathbf{J}_q (t)$ is the heat flux vector.

From Eq. 3.13 it may be shown that the calculation of the thermal conductivity by GK

relations needs a microscopic definition of an instantaneous heat flux $\mathbf{J}_q(t)$ of the system. At equilibrium the molecular form of the heat flux vector in a system of N molecules in volume V is given by:

$$\mathbf{J}_q V = \sum_{i=1}^{N_m} e_i \frac{\mathbf{p}_i}{M_i} - \frac{1}{2} \sum_{i=1}^{N_m} \sum_{\alpha=1}^{N_s} \sum_{j \neq i}^{N_m} \sum_{\beta=1}^{N_s} \mathbf{r}_{ij} \mathbf{F}^{LJ}_{i\alpha j\beta} \cdot \frac{\mathbf{p}_{i\alpha}}{M_{i\alpha}}. \tag{3.14}$$

The indices i and j go over all N_m molecules of the system. In the diffusive part, $\mathbf{v}_i$ is the center-of-mass velocity of the molecule i, and its internal energy e_i consists of the kinetic energy of all its atoms, potential energy of deformation due to torsion, bending or bond stretching, and potential energy of interaction of its atoms with the rest of atoms in the liquid. In the interaction part, $\mathbf{r}_{ij} = \mathbf{r}_j - \mathbf{r}_i$ is the minimum image distance between the centers of mass of the molecule i and j, $\mathbf{F}^{LJ}_{i\alpha j\beta}$ is the force of interaction between the atom α belonging to the molecule i and the atom β of the molecule j, and $\mathbf{p}_{i\alpha}$ is the momentum of the atom α of the molecule i.

3.7 Simulation details

The molecular simulations were performed at two different temperatures and densities. Both systems consisted of 256 CS_2 molecules. One had a density of 1,420 kg/m^3 at a temperature of 193 K and the other had a density of 1,427 kg/m^3 at a temperature of 309 K. The Lennard-Jones potentials for the site-site interactions were truncated at 8.8 Å for the C-C, C-S and S-S interactions. All the computations were carried out in reduced units, using m_c, σ_{cc} and ϵ_{cc} as the reduction parameters. For example, the conversions from reduced to real units for time and viscosity are performed using the expressions: $t^* = \sigma_{cc}(m_c/\epsilon_{cc})$ and $\eta^* = \sigma^2_{cc}/(m_c\epsilon_{cc})^{1/2}$. Quantities in real units will have units specified and the asterisk will be omitted from reduced quantities in the remainder of this chapter.

The equilibrium simulations for 193 K system ran for a total averaging time of 72.08 ns.

The stress and heat flux acfs were computed with maximum lag times of 44 ps and 7 ps respectively. For the 309 K system total averaging time is 178 ns and stress and heat flux acfs were computed with maximum lag times of 57 ps and 7 ps respectively. All of the correlation functions decayed to zero within their respective maximum lag times.

The shear rates used in the non-equilibrium simulations were $\dot{\gamma} = 0.01$, 0.02, 0.03, 0.05, 0.06, 0.1, 0.2, 0.4, 0.5, 1.0 and 2.0 in reduced units. The total steady state averaging time for each shear rate was 4.3 ns.

3.8 Results and discussion

The potential energy per molecule, including long range corrections, was found to be -70.15 in (C-C) reduced units for the 193 K system, which is in excellent agreement with Tildesley and Madden's result (- 70.13) for the same model and state point. Similarly, the pressure including long range corrections was found to be 0.37 $\pm$ 0.14, which compares well with TM's value, 0.25.

Fig. 3.1 and Fig. 3.2 show the stress acf for liquid carbon disulphide at 193 K and 309 K respectively and Fig. 3.3 and Fig. 3.4 show the viscosity of CS_2 for liquid carbon disulphide at 193 K and 309 K as a function of time obtained from the normalized Green-Kubo integral given by Eq. (3.9).

For convenience, we have defined $N(\tau) = \left\langle \mathbf{P}^{0s}(\tau) : \mathbf{P}^{0s}(0) \right\rangle / 10$. Fig. 3.1 shows the acf up to the maximum delay time of 44 ps (25 reduced units) in the main figure and details of the short time decay in the inset. The Fig. 3.2 shows the acf up to the maximum delay time of 57 ps (32 reduced units) at 309 K and details of the short time decay in the inset. The stress acf displays a minimum, followed by a maximum and then a slow decay to zero. This distinctive shape is unlike the stress acfs for liquid Ar and CF_4 which show a monotonic decay [28], but it is similar to the stress acf for benzene [28]. The complicated

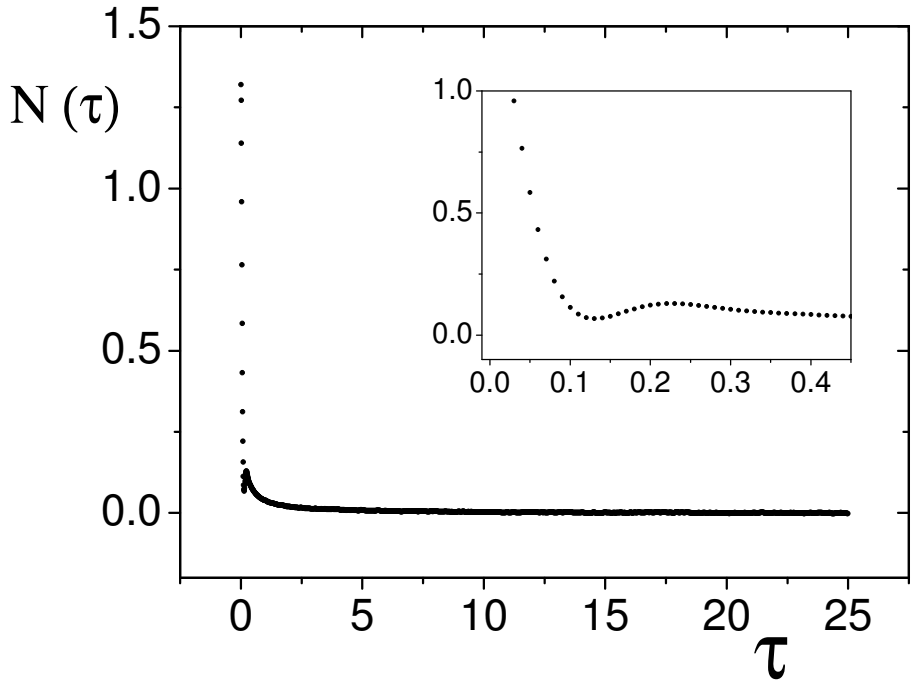

Figure 3.1: Stress auto correlation function for liquid carbon disulphide at 193 K. The inset shows the behaviour near zero delay time more clearly.

behaviour of the stress acf for molecular liquids can be understood by considering the effect of relaxation of the molecular orientation for highly anisotropic molecules. This effect seems to be absent in the case of liquid N_2 [28], which is considerably less anisotropic than benzene or CS_2. The behavior of the stress acf for liquids composed of flexible anisotropic molecules is again different from spherical and rigid-body anisotropic molecules [29]. In the case of butane [29], we see a minimum followed by a maximum and then a slow decay, but the maximum and minimum are much smoother and the long decay is much slower than for rigid body molecules, due to the existence of an internal degree of freedom responsible for its flexibility.

Fig. 3.3 illustrates that the viscosity has reached a constant value at long time, giving the zero shear rate viscosity. From the data the zero shear rate viscosity of equilibrated liquid

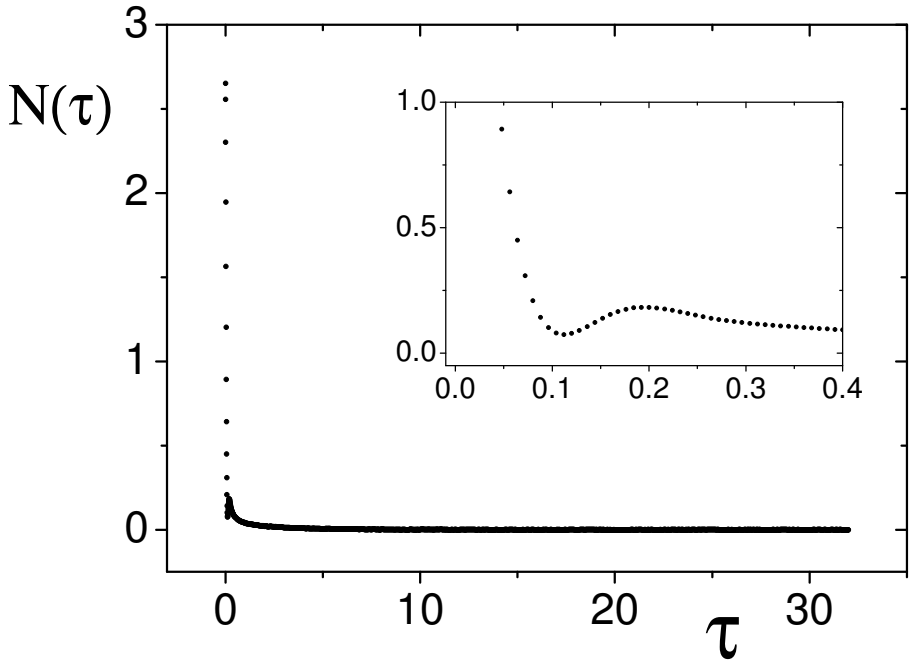

Figure 3.2: Stress auto correlation function for liquid carbon disulphide at 309 K. The inset shows the behaviour near zero delay time more clearly.

CS_2 at 193 K is 37.7 ± 0.1 in reduced units which is equal to 1261±3 μPa s. According to Fig. 3.4, the viscosity of CS_2 at 309 K converged to a constant value of 25.7 ± 0.2 in reduced units which is equal to 858±7 μPa s.

Fig. 3.5 shows the viscosity obtained from the non-equilibrium molecular dynamics simulations versus squared shear rate for low shear rates. Only the data that satisfy a linear relationship are shown in the Figure. To determine the zero shear rate viscosity we compute a linear fit using the built-in curve fitting capabilities of the Origin (version 8) graph plotting software. (This was also used for all subsequent data analysis.) According to the fit in Fig. 3.5 the zero shear rate viscosity is 37.8 ± 0.8 in reduced units or $1,260 \pm 30$ μPa s, which is in excellent agreement with the value obtained from equilibrium simulations using the Green-Kubo method.

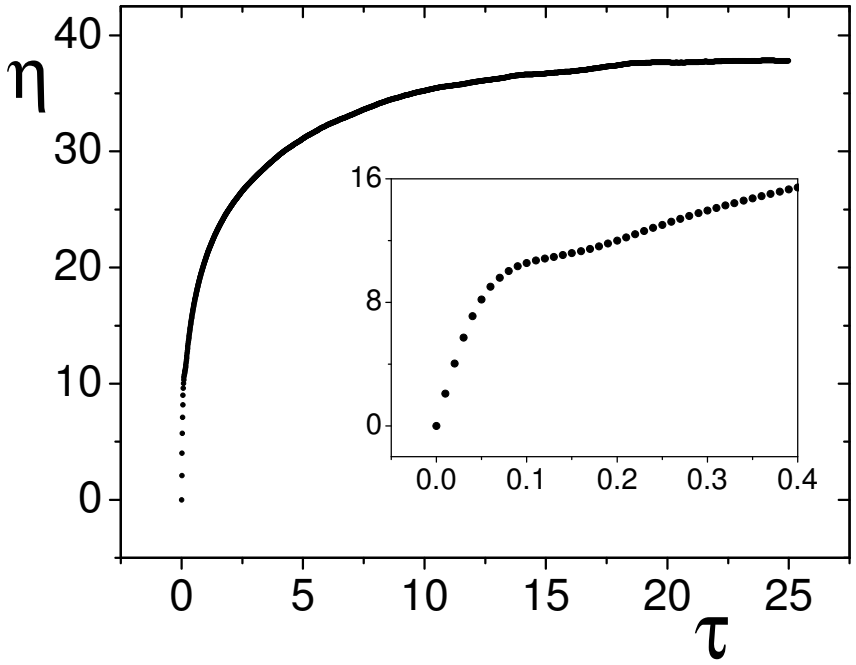

Figure 3.3: Running integral of the stress acf for liquid carbon disulphide at 193 K. The inset shows the behaviour of the acf near zero delay time.

Fig. 3.6 shows the log-log graph of viscosity versus strain rate for all of the values of shear rate studied. We can see a linear relationship in the log-log plot between strain rates of 0.01 and 1.0, indicating that the viscosity follows a power law at high strain rates. This is similar to the behavior of polymer melts [30] in which shear induced alignment and chain stretching are responsible for shear thinning. In CS_2, shear induced alignment is the only one of these two factors present, similar to the case of a liquid crystal in the isotropic phase.

The shear rate dependence of the viscosity can be described by a variety of empirical functions which are well-known in the field of polymer rheology. Two commonly used

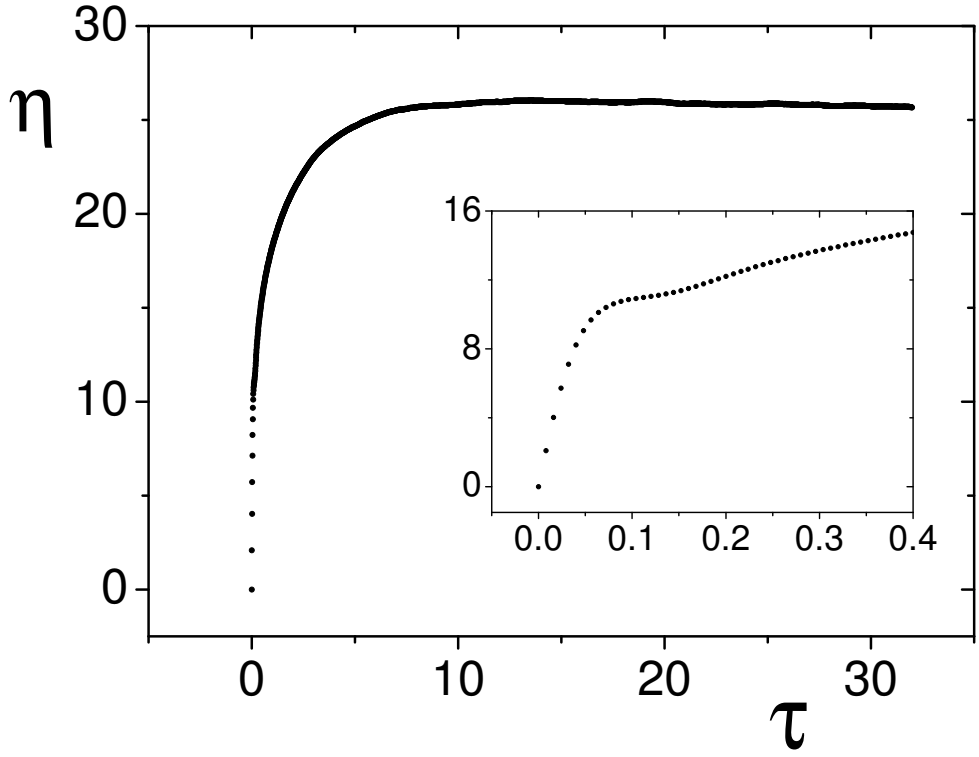

Figure 3.4: Running integral of the stress acf for liquid carbon disulphide at 309 K. The inset shows the behaviour of the acf near zero delay time.

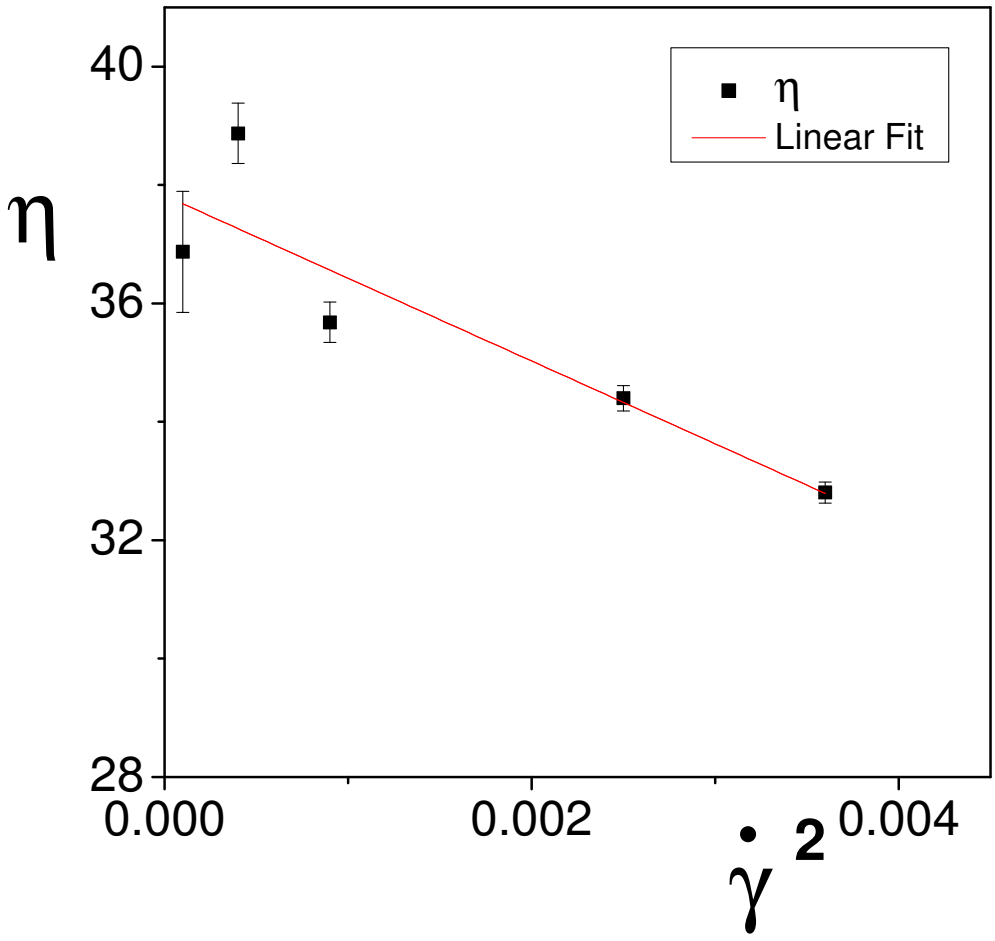

Figure 3.5: Viscosity versus squared shear rate for liquid carbon disulphide at 193 K for small shear rates. The linear fit shown uses the data for $\dot{\gamma} \leq 0.06$.

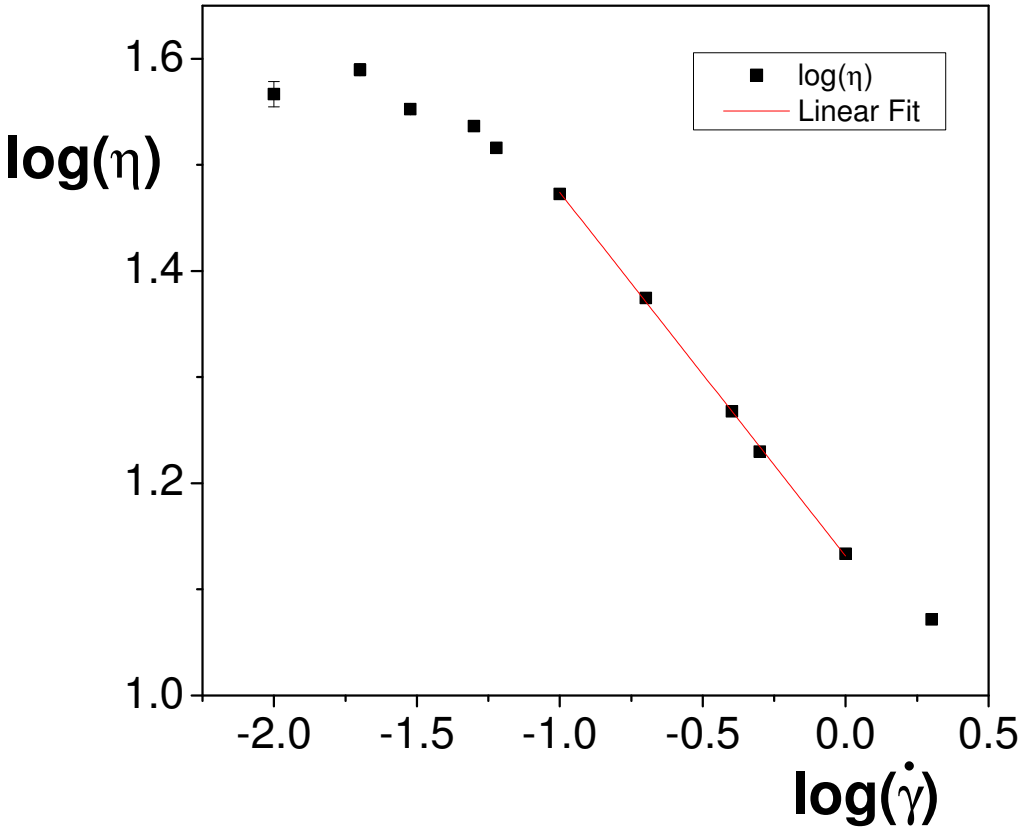

Figure 3.6: Log viscosity versus log shear rate for liquid carbon disulphide. The slope in the range $0.1 \leq \dot{\gamma} \leq 1.0$ is -0.34.

functions are the Carreau function, [31]

$$\eta = \eta_\infty + \frac{\eta_0 - \eta_\infty}{\left[1 + (\tau_1 \dot{\gamma})^2\right]^p} \tag{3.15}$$

and the Cross function [31]

$$\eta = \eta_\infty + \frac{\eta_0 - \eta_\infty}{1 + |\tau_2 \dot{\gamma}|^m} \tag{3.16}$$

where η_0 the zero shear rate viscosity and η_∞ is the infinite shear rate viscosity, and τ_1 and τ_2 are time constants. It is of interest to determine whether these functions also provide a good description of the shear rate dependence of the viscosity for a simple fluid such as

CS_2.

Fig. 3.7 shows the shear viscosity versus strain rate. A fit using the Carreau function gives $\eta_0 = 37.9 \pm 0.6$ for the zero shear rate viscosity, $\eta_\infty = 6.5 \pm 3.5$ for the infinite shear rate viscosity, $\tau_1 = 15 \pm 3$ for the time constant and $p = 0.27 \pm 0.08$ for the exponent. These values can be converted to $\eta_0 = 1,270 \pm 20$ μPa s, $\eta_\infty = 200 \pm 100$ μPa s and $\tau_1 = 27 \pm 5$ ps in real units. Fitting the Cross function to the data in Fig. 3.7 gives a zero shear rate viscosity of $\eta_0 = 38.8 \pm 0.9$, a time constant of $\tau_2 = 5.4 \pm 0.6$, an exponent m of 1.3 ± 0.2 and an infinite shear rate viscosity η_∞ of 11 ± 1. In real units, these correspond to $\eta_0 = 1,300 \pm 30$ μPa s, $\tau_2 = 10 \pm 1$ ps and η_∞ of 350 ± 40 μPa s. Both functions give zero shear rate viscosities in excellent agreement with the value obtained from the linear fit to the low shear rate data in Fig. 3.5, and with the equilibrium molecular dynamics value. Of the three different methods of extrapolating the shear rate dependent viscosity to zero shear rate, the linear fit to the viscosity versus squared shear rate gives the best agreement with the Green-Kubo result, closely followed by the fit to the Carreau function.

The Carreau function has the convenient feature of possessing a power series expansion at low shear rates, unlike the Cross function, which has a discontinuous first derivative at zero shear rate. In addition, the form used here (unlike the more general Carreau-Yasuda function in which the power of the shear rate factor need not be equal to 2 [31]) explicitly gives a viscosity that is an analytic, even function of the shear rate. This is consistent with the linearity of the plot of viscosity versus the squared shear rate observed in Fig. 3.5. Comparing the initial slope ($d\eta/d\dot{\gamma}^2$) of the the viscosity in Fig. 3.5 with that obtained by Taylor expanding the Carreau function, we find that the direct evaluation gives -1400 ± 400 whereas the same quantity evaluated from the Carreau function is $-(\eta_0 - \eta_\infty)\, p\tau_1^2 = -1900 \pm 1600$. The agreement between these two values is excellent, considering the propagation of uncertainties through the evaluation of the initial slope from the Carreau function. The η_∞ parameter is needed in both functions in order to accurately describe the shear rate dependence of the viscosity at high shear rates. It is

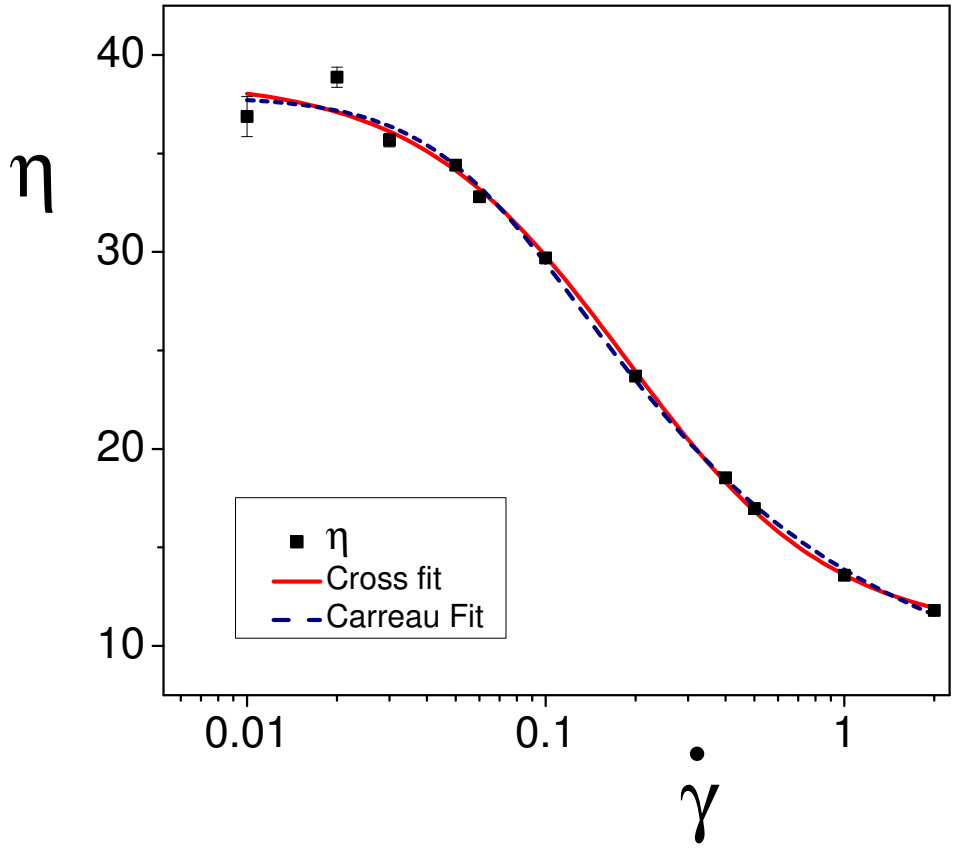

Figure 3.7: Shear viscosity versus strain rate for liquid carbon disulphide. The dashed line is the Carreau fit, Eq. (3.15) and the solid line is the Cross fit, Eq. (3.16).

well known that the viscosity goes through a minimum and then increases at very high shear rates when it is computed under constant volume conditions [7]. In contrast, the viscosity continues to decrease at high shear rates when it is evaluated under constant pressure conditions [7].

The results for the zero shear rate viscosity can be compared with previous simulation results and experimental results. Stassen and Steele calculated the shear viscosity of CS_2 at the same state point and obtained a value of 1,073 μPa s, which is considerably lower

than our value. However, they remark that their value is most likely an underestimate of the correct value, because their stress acf had not completely decayed to zero within the computed maximum delay time.

Experimental values of the viscosity can be obtained from the correlation developed by Assael et al. [26, 27]. This correlation expresses the logarithm of the reduced hard-sphere viscosity as a power series in the inverse reduced volume. Using the roughness factor (which can be obtained by fitting experimental data for a property at a single temperature and density) and a characteristic volume, which is temperature dependent but equal for different transport properties, the hard sphere value can be converted to an experimental value of a transport property for a given substance. With the data for CS_2 given by Assael et al. [27] we calculated a value of viscosity for the T=193 K state point as 964 μPa s, and for the T=309 K state point as 758 μPa s. When compared with our simulation values (the EMD viscosity result for 193 K is 1261 ± 3 μPa s and for 309 K it is 858 ± 7 μPa s) it is 23 % different from the value for 193 K and 12 % different from the value for 309 K.

The difference between the values may be because the Tildesley and Madden model is optimized at a temperature 193K to match the experimental pressure and their properties such as sigma and epsilon are defined at that temperature. The parameters we are using to the model may need to change according to the temperature.

Fig. 3.8 shows the first normal stress coefficient Ψ_1 versus squared strain rate $\dot{\gamma}^2$ for low shear rates. A linear fit to the data shows that the zero shear rate normal stress coefficient $\Psi_{1,0}$, is equal to 200 ± 20 and the slope of the line is $-18,000 \pm 6,000$. The zero shear rate first normal stress coefficient can be combined with the zero shear rate viscosity to give a viscoelastic relaxation time, $\tau_v = \Psi_{1,0}/2\eta_0 = 2.6$ [31]. This value does not agree very well with the relaxation times of the Carreau and Cross functions, and it implies a critical shear rate for shear thinning effects of $1/\tau_v = 0.38$, which is well above the shear

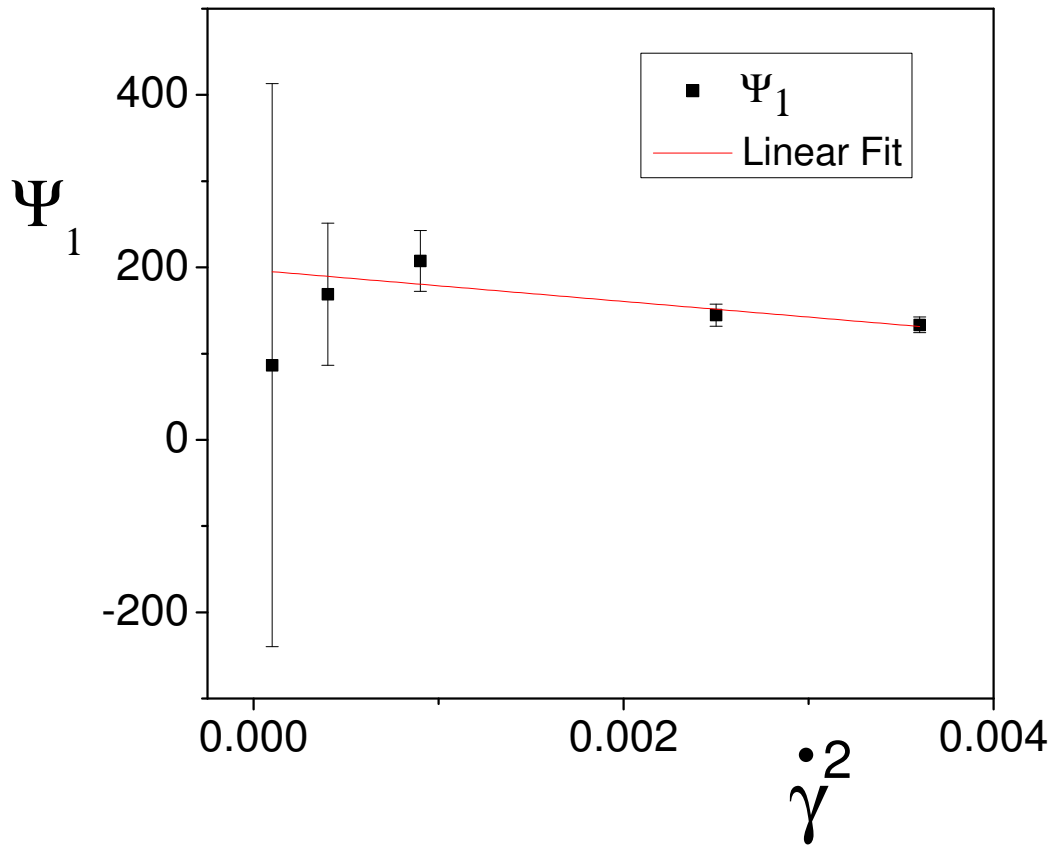

Figure 3.8: First normal stress coefficient versus squared strain rate for liquid carbon disulphide at 193 K. The solid line is a linear fit to the data.

rate at which shear thinning is observed to occur in Fig. 3.7. On the other hand, the Carreau and Cross functions give critical shear rates of 0.07 and 0.19 respectively. This discrepancy requires further investigation.

Fig. 3.9 shows the first normal stress coefficientΨ_1 versus strain rate $\dot{\gamma}$ over the entire range of shear rates studied. A Carreau function fits the whole curve very well, giving $\Psi_{1,0} = 176 \pm 6$ which agrees with the fit to the low shear rate data.

Fig. 3.10 shows the negative of the total internal energy $(-U)$ as a function of the strain

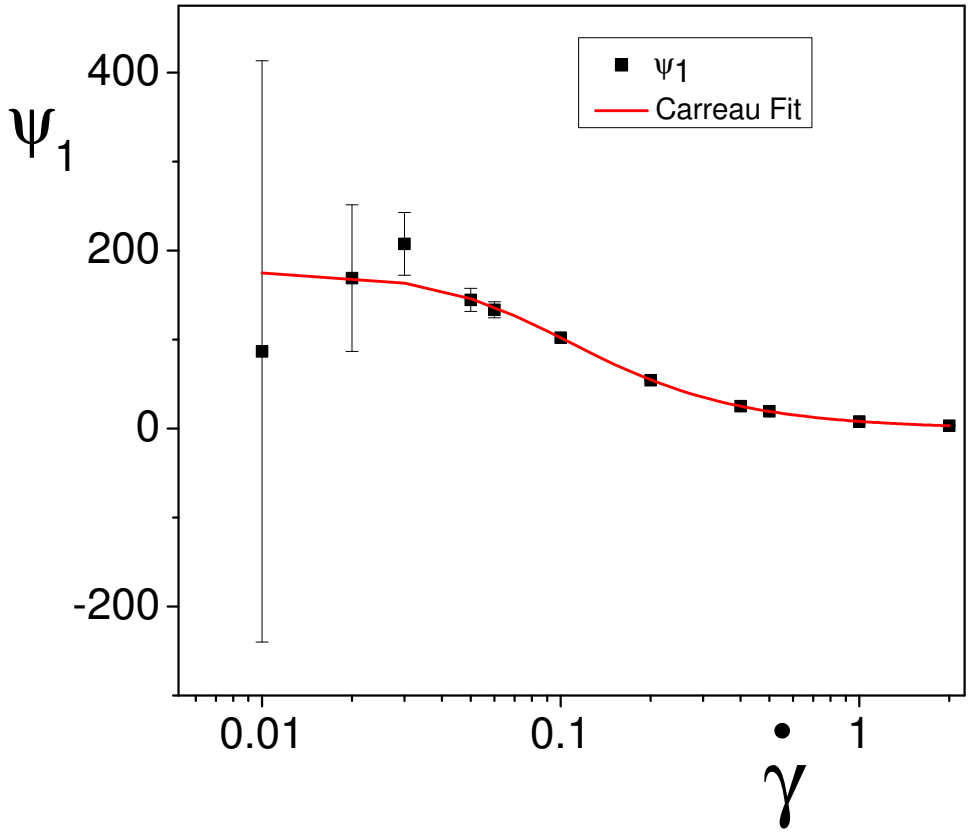

Figure 3.9: First normal stress coefficient versus squared strain rate for liquid carbon disulphide at 193 K. The nonlinear fit to the data is given a four-parameter Carreau function of the form Eq. (3.15).

rate. At strain rates less than 0.2 the internal energy is approximately constant. The variation of the internal energy can be fitted using the equation

$$U = U_1 + A_U e^{-(\dot{\gamma}/t_U)} \tag{3.17}$$

where $U_0 = U_1 + A_U$ is equal to the zero shear rate internal energy where U_1, A_U and t_U are constant.

Fig. 3.11 shows the total pressure as a function of strain rate. At strain rates less than

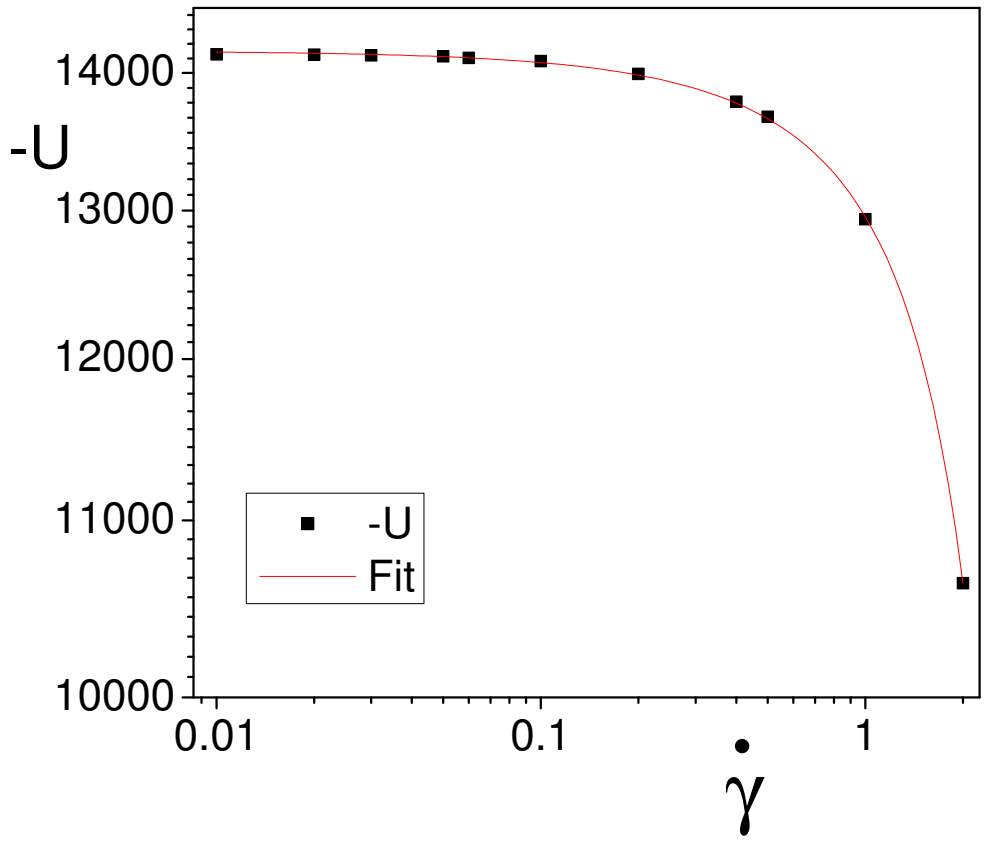

Figure 3.10: Internal energy plotted as $-U$ versus strain rate for liquid carbon disulphide at 193 K. The solid line is a fit to Eq. (3.17).

0.2 the pressure of the system is approximately constant. The variation of the pressure can be fitted by the equation:

$$P = P_1 + A_P e^{-(\dot{\gamma}/t_P)} \tag{3.18}$$

where $P_0 = P_1 + A_P$ is the zero shear rate pressure where P_1, A_P and t_P are constant.

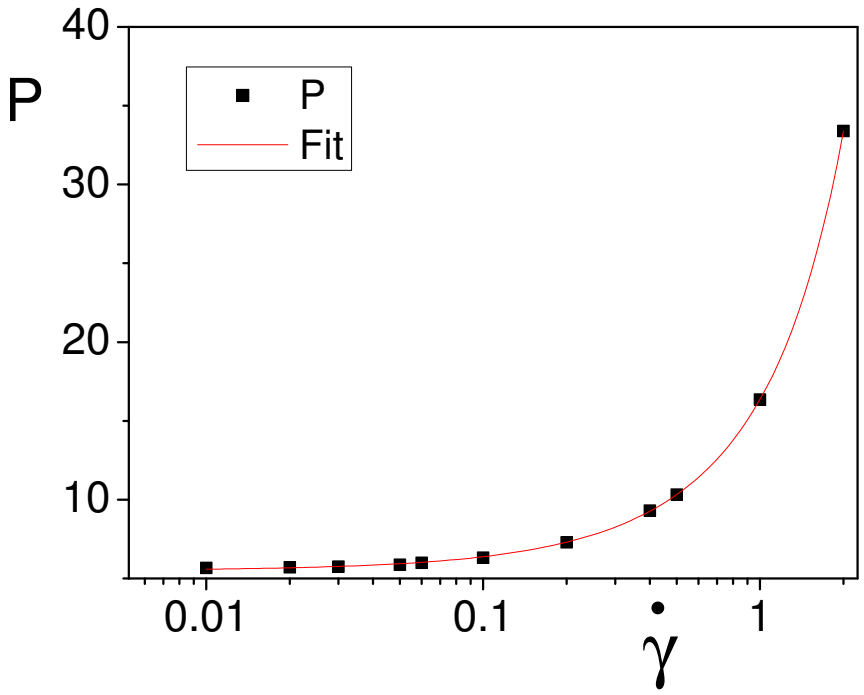

Figure 3.11: Total pressure versus strain rate for liquid carbon disulphide at 193 K. The solid line shows a fit to Eq. (3.18).

In both cases, we see that the shear rate dependence of the internal energy and the pressure are surprisingly well described by a simple three parameter function.

Fig. 3.12 and 3.13 show the heat flux auto-correlation function defined as:
$Q(\tau) = \langle \mathbf{J}_q(\tau) \cdot \mathbf{J}_q(0) \rangle / 3$ and Fig. 3.14 and 3.15 show the thermal conductivity of CS_2 obtained from Eq. 3.13 as a function of correlation time for two different temperatures.

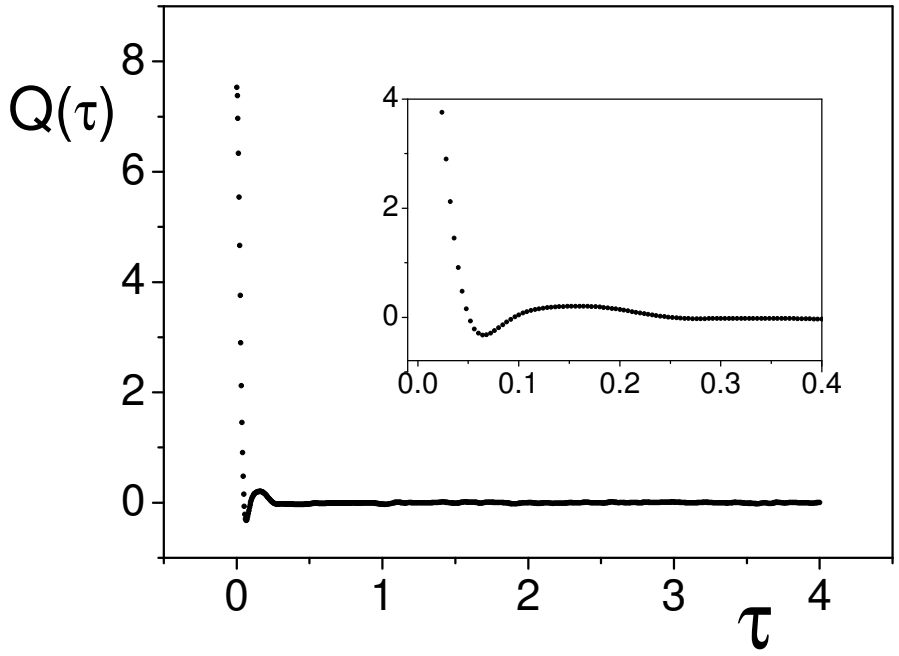

Figure 3.12: Heat flux auto correlation function for liquid carbon disulphide at 193 K. The inset shows the behaviour near zero delay time more clearly.

The integral has clearly converged after 3.5 ps (2 reduced time units) for both the T=193 K and T=309 K systems, the T=193 K system gives the thermal conductivity of 7.98 ± 0.08 in reduced units which is equal to 0.185 ± 0.002 W m^{-1}K^{-1} while the thermal conductivity of the T=309 K system gives 10.67 ± 0.09 in reduced units which is equal to 0.247 ± 0.003 W m^{-1}K^{-1}. The low temperature heat flux acf shows a negative minimum, followed by a maximum and then a rapid decay to zero. This contrasts with the heat flux acf of molecular fluids composed of spherical molecules. In 1994 Hoheisel et al. observed that the heat flux acf for an atomic liquid is positive and monotonic [28]. It is also different from the heat flux acf for liquid butane, which shows a monotonic decay [29]. This indicates that molecular reorientation is not as important for relaxation of the heat flux acf as it is for the stress acf. This is also evident in the shorter relaxation time of the heat flux acf compared to that of the stress acf. At the higher temperature the short time decay of the

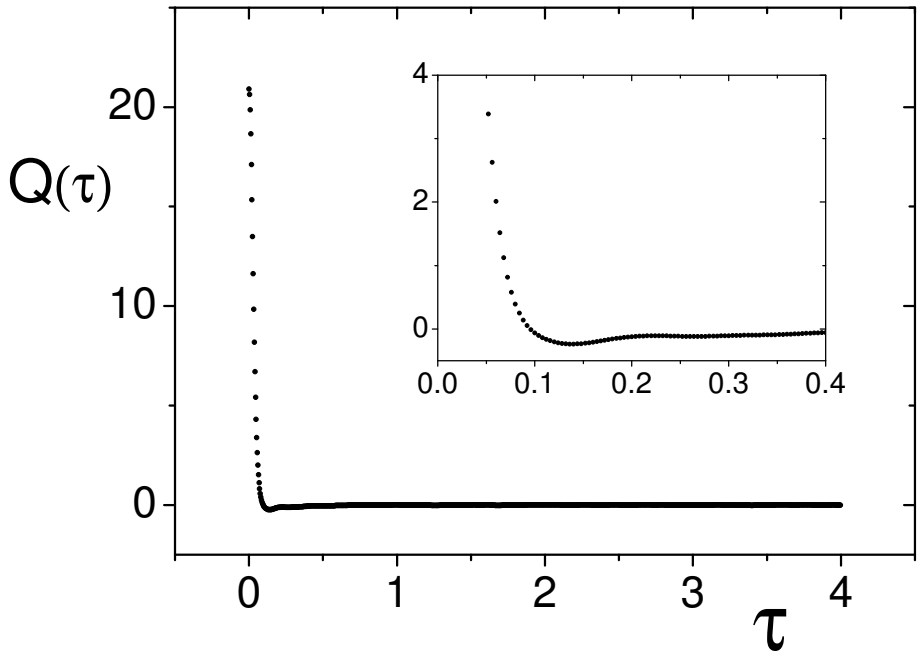

Figure 3.13: Heat flux auto correlation function for liquid carbon disulphide at 309 K. The inset shows the behaviour near zero delay time more clearly.

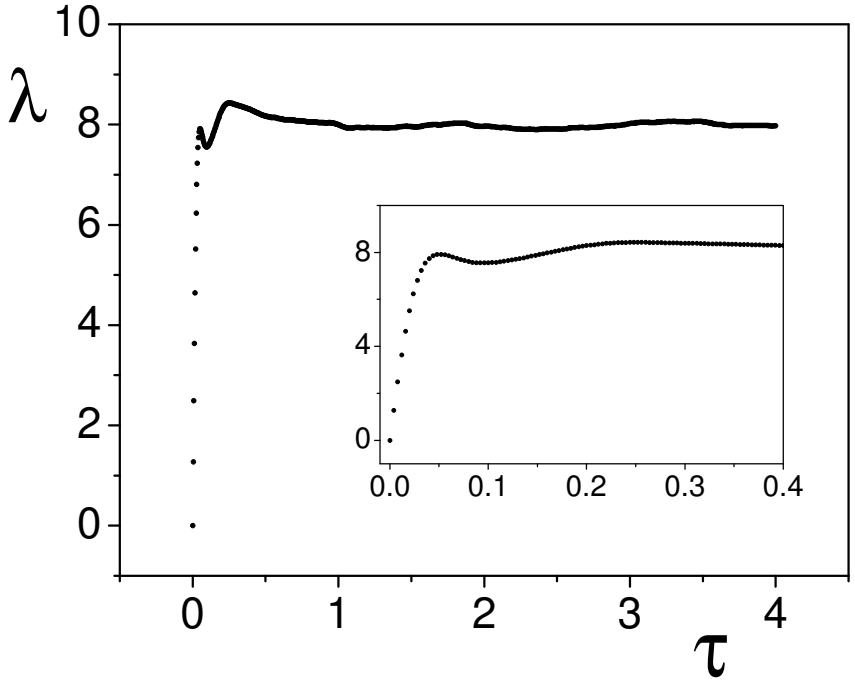

Figure 3.14: Running integral of the normalized heat flux acf for liquid carbon disulphide at 193 K. The inset shows the behaviour near zero delay time more clearly.

heat flux acf is much smoother.

There do not appear to be any previous computations of the thermal conductivity of liquid CS_2. However, we can use the correlation developed by Assael et al. [27] to calculate an experimental value. The calculation of experimental values using their method is briefly reviewed in the Appendix C. (Note that equation (8) of the paper by Assael et al. [27] contains a typographical error - the denominator should contain a factor of $R^{3/2}$ instead of $R^{1/2}$). Using their correlation, we find $\lambda = 0.184$ W m^{-1}K^{-1} for 193 K and $\lambda = 0.205$ W m^{-1}K^{-1} for 309 K, which is in excellent agreement with our result for 193 K (0.185 ± 0.002 W m^{-1}K^{-1}) but for 309 K it is 17% different from our value which is 0.247 ± 0.003 W m^{-1}K^{-1}.

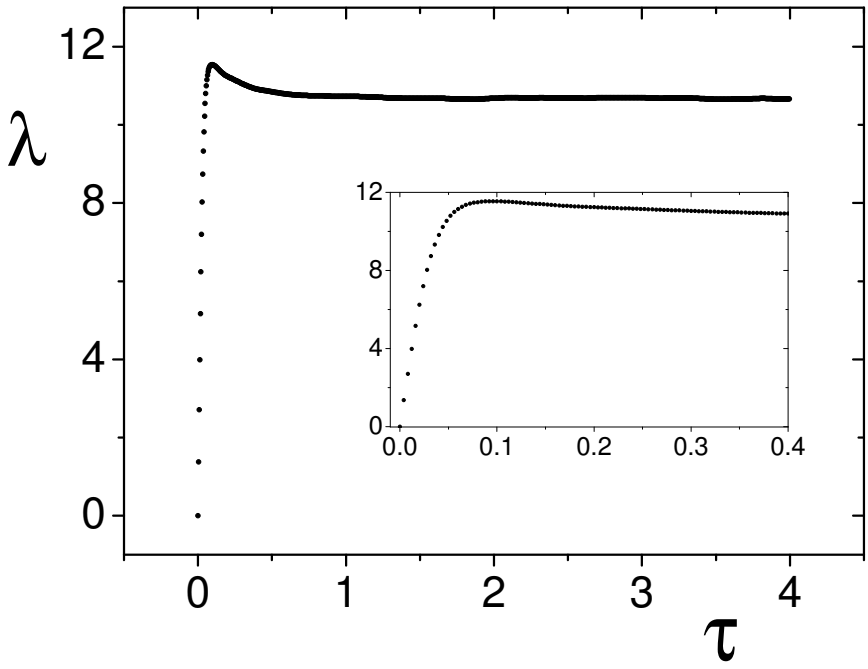

Figure 3.15: Running integral of the normalized heat flux acf for liquid carbon disulphide at 309 K. The inset shows the behaviour near zero delay time more clearly.

3.9 Conclusion

The viscosity and thermal conductivity of carbon disulphide have been calculated using equilibrium molecular dynamics simulations with the Green-Kubo method. The simulation technique was based on a constraint method proposed by Baranyai and Evans [11] that combines the Edberg, Evans and Morriss [12] method for solving the constraint equations with the Ciccotti, Ferrario and Ryckaert [9] method for formulating the constraint equations for molecules with primary and secondary constraints. In addition, the shear rheology has been computed by non-equilibrium molecular dynamics methods, giving excellent agreement between the viscosities calculated by both methods. Both the viscosity and thermal conductivity values were in good agreement with the predictions of a correlation based on the rough hard sphere model.

3.10 Acknowledgement

This work has been published before in Journal of Molecular Liquids (2010).

Chapter 4

Temperature dependence of shear viscosity of SPC/E water

Imagination is more important than knowledge.

Albert Einstein (1879 - 1955)

4.1 Introduction

In computational chemistry, classical water models are used for the simulation of liquid water, and aqueous solutions with explicit solvent in order to help discover the properties of them. Due to its pervasiveness on the earth and other planets water is the most investigated liquid in the literature. A recent review showed that more than 45 distinct models of water [32] have been considered within the past 30 years. These models differ according to whether they are rigid or flexible, and whether the model includes polarization effects. Many of the interaction potentials used to model water treat the molecules as rigid and non-polarizable, although several flexible and polarizable water models have been developed recently. A fairly representative rigid model of liquid water is the extended simple

point charge SPC/E model [2, 33].

According to Guillot's [32] survey regarding computer simulation on water, the SPC/E water model shows good agreement with experimental or target values of the liquid state properties [32]. As an example the SPC/E model reproduces the liquid density target value ($0.997 g/cm^3$) and also it predicts a critical point close to the critical point of real water. Alejandre et al. [34], reported that the SPC/E model of water gives a better account of the orthobaric densities and surface tensions than either the SPC or TIP4P models. Gonzalez et al. [35], have shown that the SPC/E water model is the only rigid and non-polarisable model which reproduces most of the dynamic properties of water.

Even though many papers were published relating to liquid water models and properties, not many were able to calculate the viscosity accurately. Balasubramanian et al. [33] were able to calculate the viscosity using the SPC/E model at 303.15K and they implied that their simulation result is 18% less than the experimental value. Wheeler et al. [17] calculated the shear viscosities of water and polar liquid mixtures via non-equilibrium molecular dynamics using the same water model. Their simulation value for shear viscosity is 15.3% less than the experimental value.

In this chapter we discuss the temperature dependence of the viscosity of the SPC/E water which was calculated by equilibrium molecular dynamics using Green-Kubo relations. Electrostatic forces are calculated from Ewald summation and we use a bond constraint algorithm to keep the rigid triatomic structure of the SPC/E model water in this simulation. The constraint algorithm method is explained in Chapter 2 and in the Appendix B.1.

Using existing experimental results for the viscosity of water we were able to form a simple and generalized equation to calculate the temperature dependence of the viscosity more accurately than previously proposed relations.

4.2 Molecular model

The water molecule consists of one oxygen atom and two hydrogen atoms (Fig. 4.1). The oxygen has six valence electrons and thus needs two more electrons from the two hydrogen atoms to complete its octet. This then leaves two lone electron pairs that are not bonded to any other atoms. These two lone electron pairs exert a little extra repulsion on the two bonding hydrogen atoms which determine the bond angle.

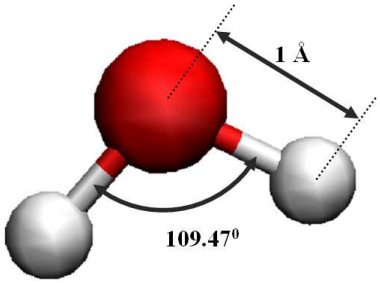

Figure 4.1: SPC/E water model

In molecular fluid studies the Lennard-Jones potential energy function is an extremely important one. For the SPC/E water model the LJ potential is truncated at 8.8 Å and the bond length is rigidly constrained to a constant value of 1.00 Å and bond angle is fixed to 109.47° [33]. The pair potential parameters of the model are shown in Table 4.1. The SPC/E model of water due to Berendsen et al. [2] was used.

Table 4.1: Lennard-Jones energy and length parameters in Eq. (3.1) for SPC/E [2]

σ_{OO}	3.17 Å
σ_{HH}	1.80 Å
σ_{OH}	2.48 Å
ϵ_{OO}/k_B	78.198 K
ϵ_{HH}/k_B	0.0000 K
ϵ_{OH}/k_B	0.1251 K

4.3 Simulation methodology

4.3.1 Constraint algorithm

The SPC/E model of water has rigidly constrained bond lengths and angles in which we can use the same Baranyai and Evans (BE) [11] method to solve constraint equations of motion as used in Chapter 2. Unlike the previously discussed CS_2 the SPC/E water molecule has no secondary particles. The model has three constraints per molecule and the constraint matrix for the model is given by:

$$\begin{bmatrix} -1 & 0 & -1 \\ 1 & -1 & 0 \\ 0 & 1 & 1 \end{bmatrix}. \tag{4.1}$$

4.3.2 Electrostatic forces - Ewald summation

The simulation of the full interaction can be carried out using long range corrections, large truncation distances, or the Ewald summations (ES) method. ES is one of the most accurate and standard methods used to calculate the long range interaction without including long range corrections. When performing simulations using the ES technique, each particle interacts with all periodic images of all particles. The simulated system is thus formally infinite. These conditions are sometimes referred to as truly periodic boundary conditions, and the ES method should be considered as one possible way to calculate the infinite lattice sums involved.

Mathematical expressions of the ES for energy, forces, and components of the pressure tensor are discussed in Chapter 2. In the Ewald formalism, the expression of a given property is conventionally divided into four different terms, viz (i) a real space term arising from the short-range interaction in the real space, (ii) a reciprocal space term arising from the long-range interaction in the reciprocal space, (iii) a self-term correcting an over-counting in the reciprocal space, and (iv) a surface term appearing in systems

with nonconducting surroundings.

There are three variables that control the accuracy of Ewald formalism: κ, the Ewald convergence parameter, r_{cut},the real space forces cutoff, and the k_{max},the largest k-vector considered in reciprocal space. These variables are not independent, and it is usual to regard one of them as pre-determined and adjust the other two accordingly. In this simulation we assume that r_{cut} is fixed and equal to $0.48 \times L$ where L is the box length. The recommended value for κ is $1.8\pi/L$ or greater [36], but if the κ value is very large then the reciprocal space sum converges very slowly. The largest k-vector, k_{max} is given by:

$$k_{max} = \frac{2\pi}{L} N_{max} \tag{4.2}$$

where, N_{max} is an integer represents number of wave vectors. For this work appropriate values are $N_{max} = 7$ and $k_{max} = 6$ in reduced units.The value of L equals to 7.8 in reduced units.

4.3.3 Shear viscosity and molecular pressure tensor

In the equilibrium simulations, the shear viscosity was calculated from the Green-Kubo relation:

$$\eta = \frac{V}{10 k_B T} \int_0^\infty \left\langle \mathbf{P}^{0s}(\tau) : \mathbf{P}^{0s}(0) \right\rangle d\tau. \tag{4.3}$$

The molecular form of the pressure tensor was calculated using the expression:

$$\mathbf{P}V = \sum_{i=1}^{N_m} \frac{\mathbf{p}_i \mathbf{p}_i}{m_i} - \frac{1}{2} \sum_{i=1}^{N_m} \sum_{\alpha=1}^{N_s} \sum_{j \neq i}^{N_m} \sum_{\beta=1}^{N_s} \mathbf{r}_{ij} \mathbf{F}^{short}_{i\alpha j\beta} + V \mathbf{P}^{(M)e,k} \tag{4.4}$$

where, $\mathbf{F}^{short}_{i\alpha j\beta}$ is defined in the Eq.(D.34) and $\mathbf{P}^{(M)e,k}$ in Eq.(D.45) of Appendix D.

4.4 Simulation details

The simulations were carried out using 500 water molecules at the temperatures of 298 K, 303.15 K and 313 K with the density of 996 kgm^{-3}. The system was simulated with periodic boundary conditions at constant NVT . The short range interactions and the real space part of the Ewald series were truncated at nearly half the box length, $r_c = 0.48 \times L$ (L=7.8 in reduced units for this system). The Coulomb interactions between the partial charges were evaluated using the Ewald summation method. The real-space truncation was at half the box length with convergence parameter $\kappa = 0.97$ in reduced units and the reciprocal space upper bound was $k_{max} = 6.0$ in reduced units. These values provides an accurate value for the electrostatics calculation. All the computations were carried out in reduced units using m_O, σ_O and ϵ_O as the reduction parameters. All the conversions from reduced to real units are given in the Table (A.1). Quantities in real units will have units specified and the asterisk will be omitted from reduced quantities in the remainder of this work.

The equilibrium simulations for the temperatures of 298 K, 303.15 K and 313 K, the stress acf were computed with maximum lag times of 25 ps. All the correlation functions decayed to zero within their respective maximum lag times. Systems ran for the total averaging time of 7.0 ns, 6.3 ns and 3.8 ns for the temperatures 298 K, 303.15 K and 313 K respectively.

4.5 Results and discussion

Fig. 4.2, 4.3, and 4.4 show the stress acfs for SPC/E water at 298 K, 303.15 K and 313 K respectively and Fig. 4.5, 4.6 and 4.7 show the viscosities of SPC/E water at 298 K, 303.15 K and 313 K respectively as a function of time obtained from the normalized Green-Kubo integral given by Eq. (4.3).

For convenience, we have defined $N(\tau) = \left\langle \mathbf{P}^{0s}(\tau) : \mathbf{P}^{0s}(0) \right\rangle / 10$. Fig. 4.2, 4.3 and 4.4

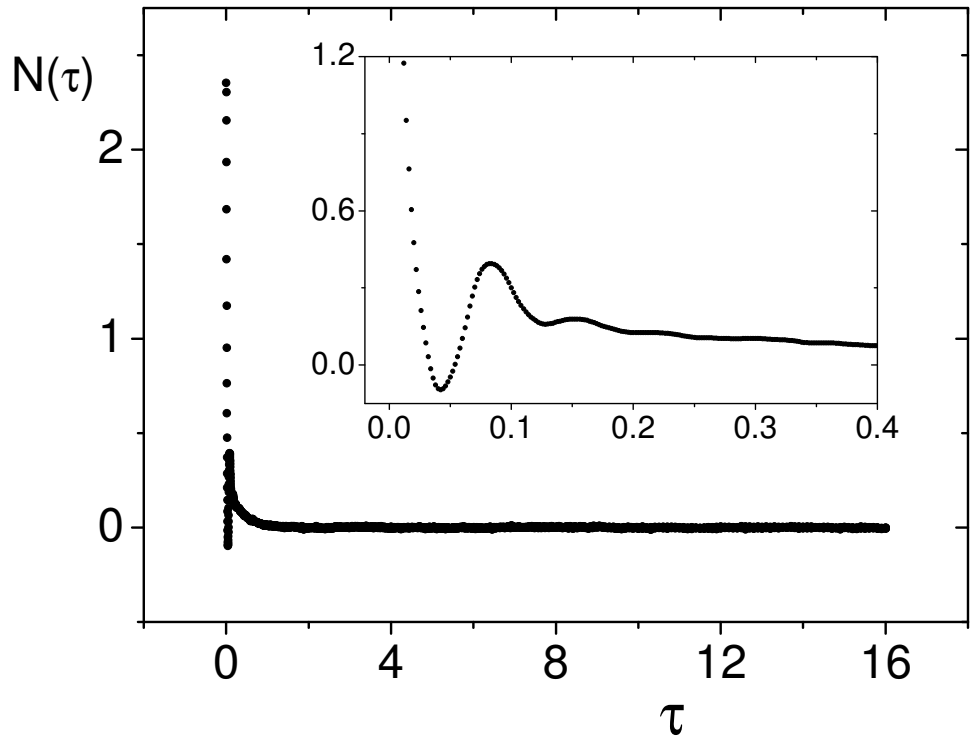

Figure 4.2: Stress auto correlation function for SPC/E water model at 298 K. The inset shows the behaviour near zero delay time more clearly.

show the acf up to the maximum delay time of 25 ps (16 reduced units) in the main figure and details of the short time decay in the inset.

In the case of SPC/E, the stress acf displays a minimum followed by a maximum and then a slow decay to zero. The maximum and minimum are much sharper and the long decay is much faster than for CS_2 (Chapter 3). The stress relaxation depends on the mass of the particle. Comparing to CS_2 molecule SPC/E has less rotational inertia and therefore it shows a sharper maximum and minimum than that of CS_2.

Table 4.2 shows the minimum and maximum values of stress auto correlation (sacf) functions of three systems. All the values are in reduced units. From the table we can see

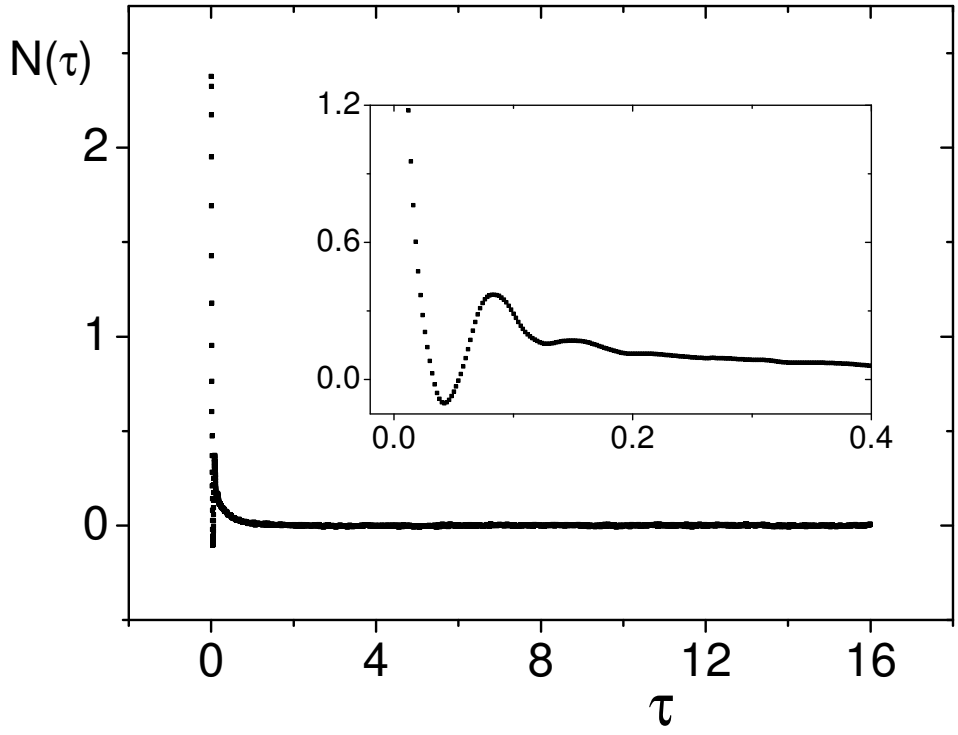

Figure 4.3: Stress auto correlation function for SPC/E water model at 303.15 K. The inset shows the behaviour near zero delay time more clearly.

that the minimum and maximum occurs at the same time. At the temperature 298 K the difference between maximum and minimum is equal to 0.49 in reduced units. The difference between maximum and minimum is about 0.475 for the temperature 303.15 K and the difference is about 0.462 at the temperature 313 K. There we can see that when the temperature increases the difference between maximum and minimum of stress auto correlation functions decreases. This is because the liquid viscosity decreases when the temperature increases.

Fig. 4.5, 4.6 and 4.7 illustrate that the viscosities have reached a constant value at long time, giving the zero shear rate viscosities of temperatures 298 K, 303.15 K and 313 K. From the data the zero shear rate viscosity of equilibrated liquid SPC/E water at 298 K

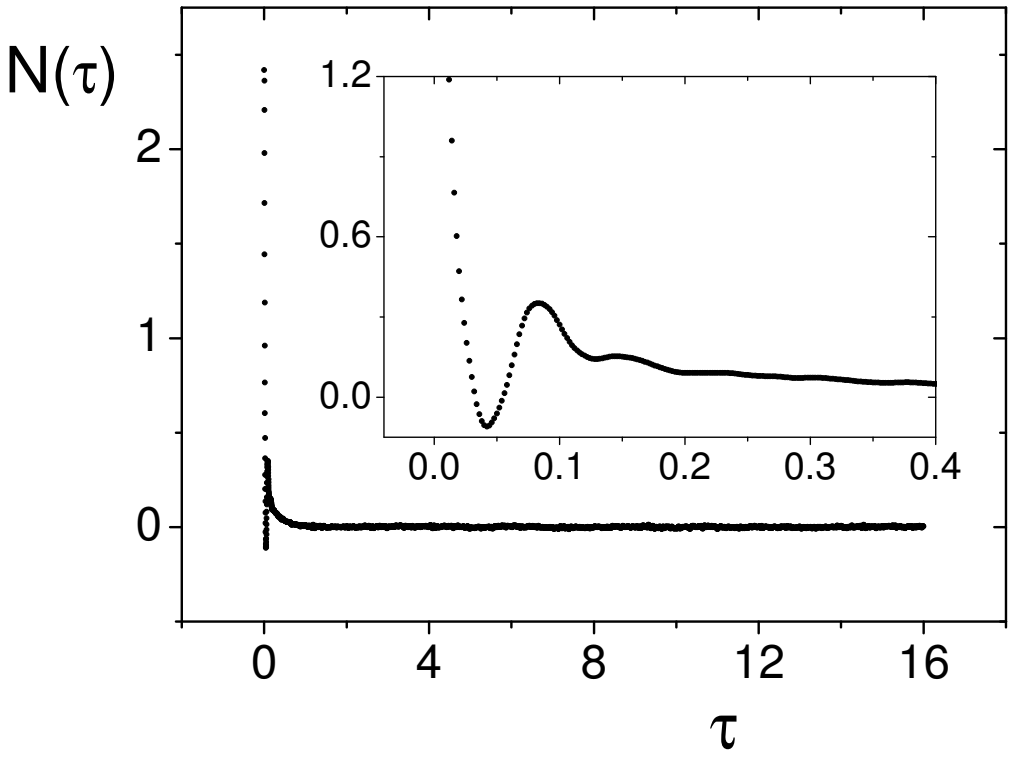

Figure 4.4: Stress auto correlation function for SPC/E water model at 313 K. The inset shows the behaviour near zero delay time more clearly.

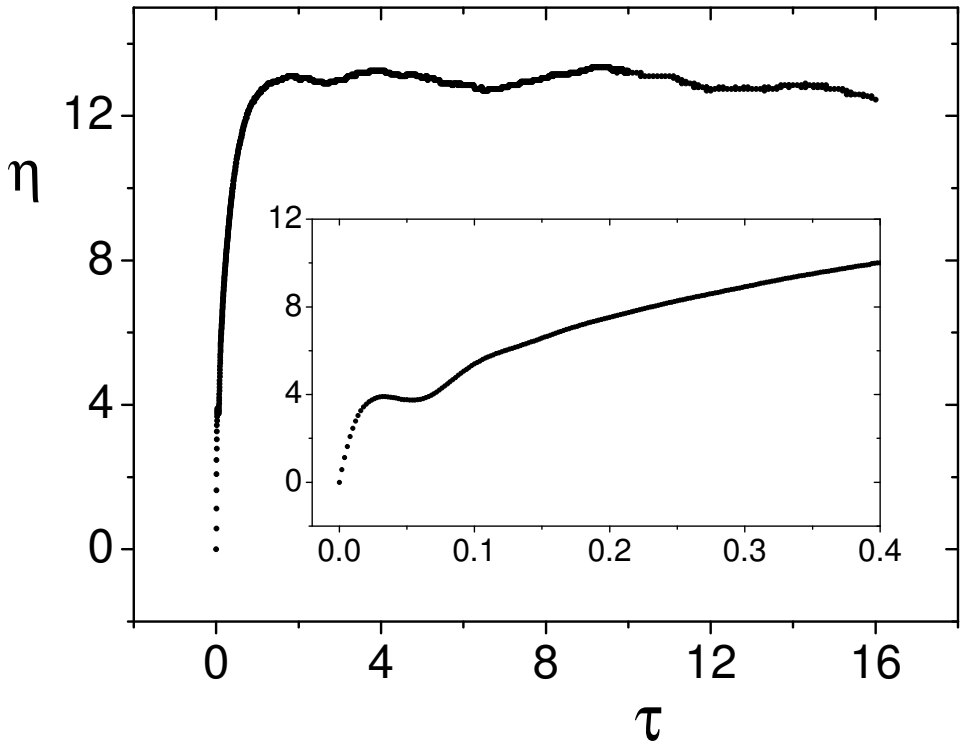

Figure 4.5: Running integral of the stress acf for SPC/E water model at 298 K. The inset shows the behaviour of the acf near zero delay time.

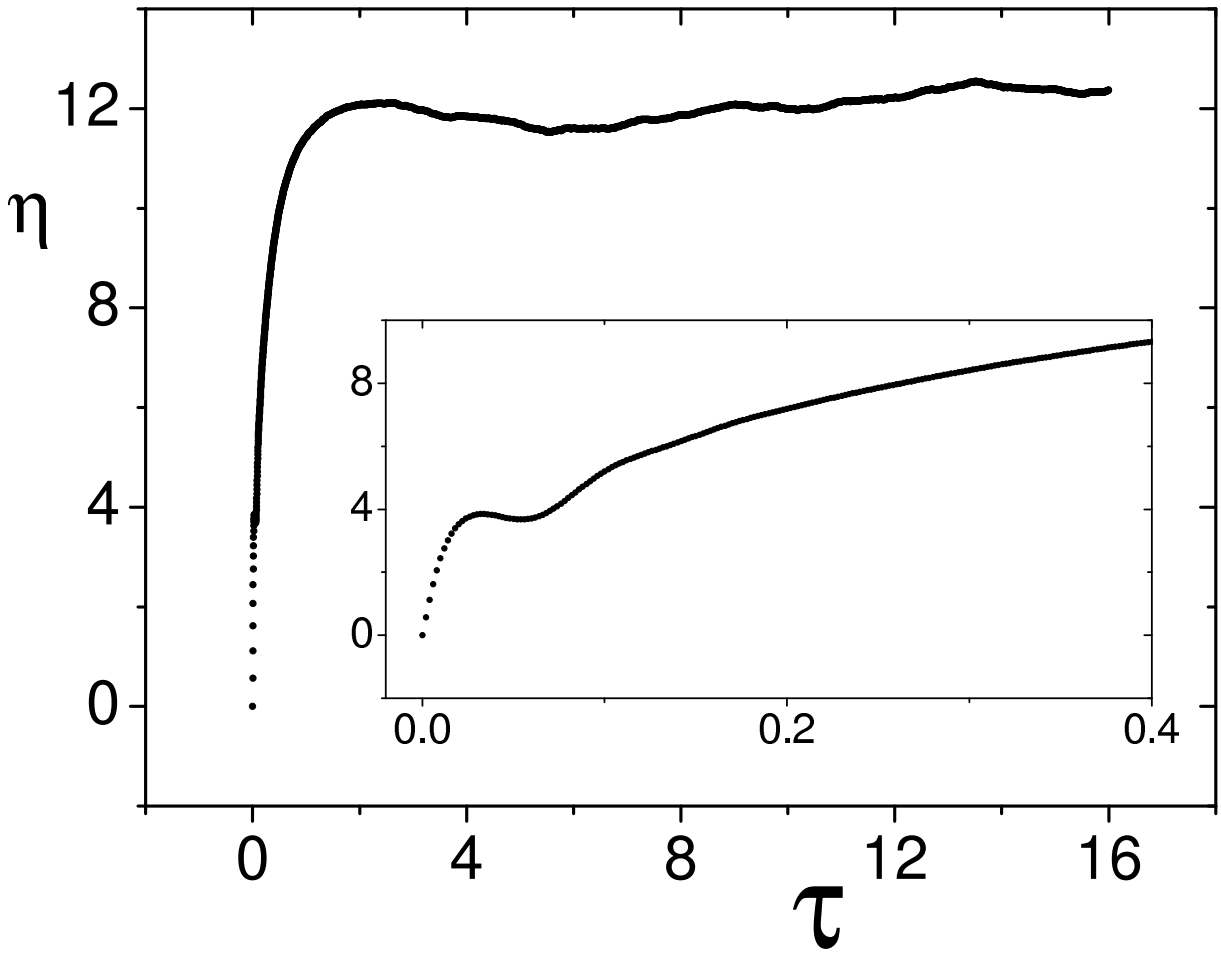

Figure 4.6: Running integral of the stress acf for SPC/E water model at 303.15 K. The inset shows the behaviour of the acf near zero delay time.

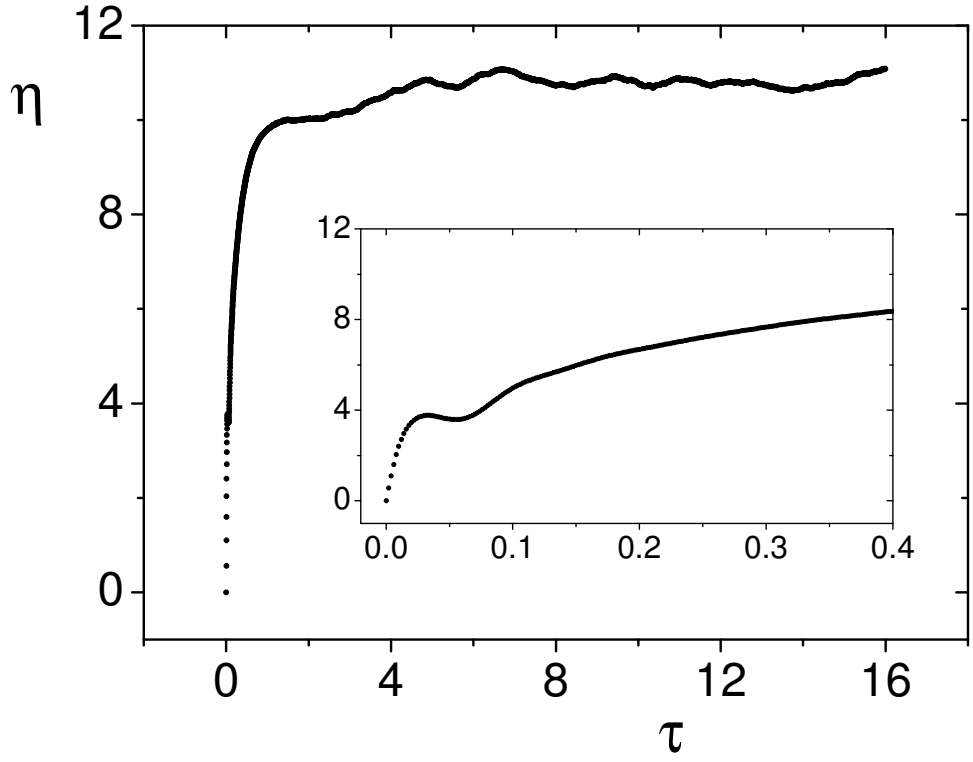

Figure 4.7: Running integral of the stress acf for SPC/E water model at 313 K. The inset shows the behaviour of the acf near zero delay time.

Table 4.2: Minimum and maximum values of sacf

temp	*min/max*	*time*	*sacf*	*error*	$(max - min)$
298	*min*	0.042	-0.096	±0.002	
	max	0.082	0.394	±0.005	0.49
303.15	*min*	0.042	-0.103	±0.004	
	max	0.082	0.372	±0.003	0.475
313	*min*	0.042	-0.11	±0.004	
	max	0.082	0.352	±0.004	0.462

is 13.9 $\pm$ 0.1 in reduced units which is equal to 7.4 $\pm$ 0.6 $\times$ 10^{-4} Pa s. The viscosity at 303.15 K converged to a constant value of 12.4 $\pm$ 0.8 in reduced units which is equal to 6.6 $\pm$ 0.4 $\times$ 10^{-4} Pa s and the viscosity at 313 K converged to a constant value of 11.2 $\pm$ 0.8 in reduced units which is equal to 6.0 $\pm$ 0.4 $\times 10^{-4}$ Pa s.

Table 4.3 lists the simulated and experimental viscosities of water at various temperatures. The simulation result for the temperature 298 K agrees well with Gonzalez and Wheelers' [17, 35] values and it is 17 % less than the experimental value of Harris [37]. Our simulation value for the temperature 303.15 K agrees with the simulation result of Balasubramanian [33].

Fig. 4.8 shows the temperature dependent viscosities of water for both simulation and experimental data. In this graph also we can see our simulation results agree with existing simulation results. Eq. (4.5) and Eq. (4.6) represent the experimentally proven equation to calculate temperature dependent viscosity of bulk water by Aleksandrov [38] and Kestin [39] respectively.

$$ln\eta = \sum_{i=0}^{5} a_i \left(\frac{100}{T}\right)^i. \tag{4.5}$$

with the following coefficient values:

$a_0 = -1.1469663\times10^1$, $a_1 = 1.43659564\times10^2$, $a_2 = -9.97411315\times10^2$, $a_3 = 3.74665106\times$

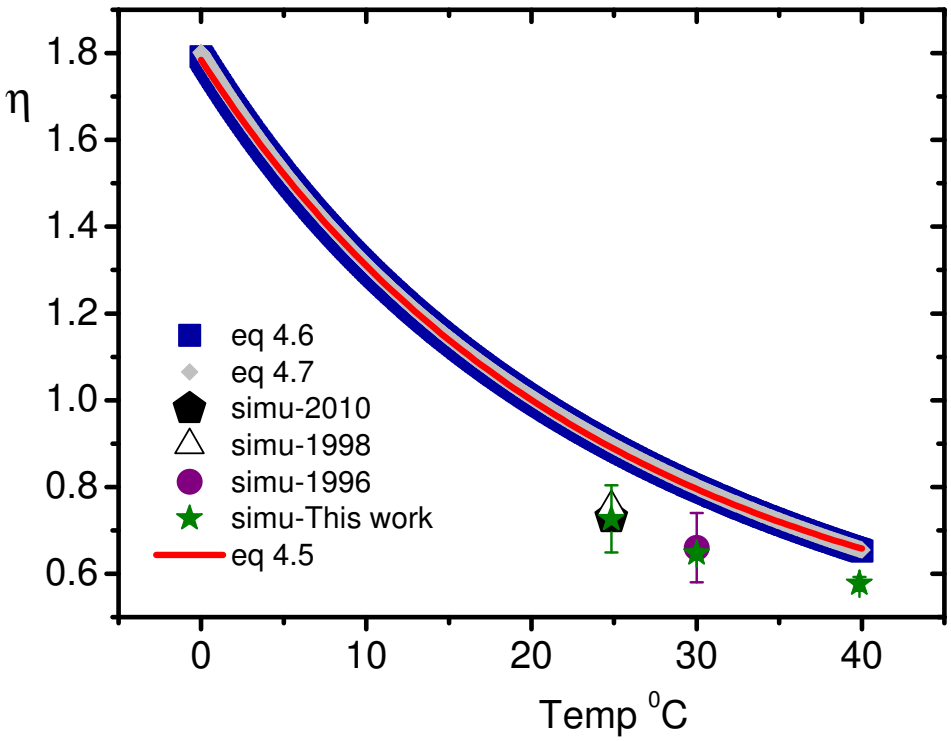

Figure 4.8: Comparison of temperature dependent viscosity of water using simulation and experimental data

10^3, $a_4 = -7.02407628 \times 10^3$ and $a_5 = 5.39493001 \times 10^3$

$$log\left\{\frac{\eta(t)}{\eta(20^0C)}\right\} = \frac{20-t}{t+96}\{1.2364 - 1.37 \times 10^{-3}(20-t) + 5.7 \times 10^{-6}(20-t)^2\}. \quad (4.6)$$

where, t is in Celsius and T is in Kelvin.

Using the existing experimental data for temperature dependent viscosity [38, 39] we define a new empirical formula to calculate the viscosity and it is given by:

$$\eta = exp(a + bt + ct^2). \quad (4.7)$$

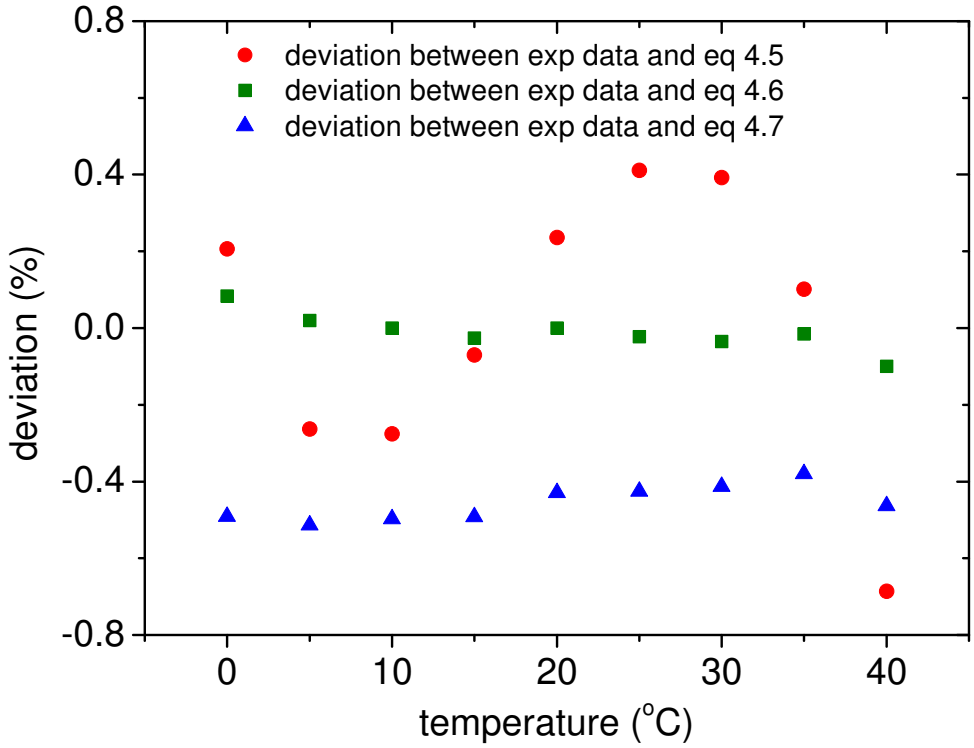

Figure 4.9: Compare the deviation of temperature dependent viscosity of proposed equations with experimental data.

Our newly formed equation gives accurate viscosities for relevant temperature and the formula we used is very simple when compared to previous ones [17, 33, 35, 37, 39]. The coefficients for the fit are given in the Table 4.4. The comparison of the deviation between experimental data and Aleksandrov, Kestin and our group is shown in the Figure 4.9.

4.6 Conclusion

The temperature dependent viscosity of the SPC/E water has been calculated by using equilibrium molecular dynamics simulations with Green-Kubo relations. Ewald summa-

tion was used to calculate electrostatic forces and the simulation technique was based on constraint method described in previous chapters to keep the rigid triatomic structure of the SPC/E model water. Not only were we able to get an excellent agreement with existing data for the viscosity of bulk water, we were able to form a simple and generalized equation to calculate the temperature dependence of viscosity more accurately using existing experimental results. Also we were able to see the characteristic behavior of the stress auto correlation function at short times.

Table 4.3: Comparison of SPC/E simulation results with existing data

First Author	Year	Method	Temperature(K)	Viscosity (mPa s)	Uncertainty
M A Gonzalez	2010	SPC/E	298.00	0.7290	
D R Wheeler	1998	SPC/E	298.15	0.7540	
S Balasubramanian	1996	SPC/E	303.15	0.6600	±0.08
This work	2011	SPC/E	298.00	0.74	±0.06
This work	2011	SPC/E	303.15	0.66	±0.04
This work	2011	SPC/E	313.00	0.60	±0.04
K R Harris	2004	Exp	298.15	0.8916	
M J Assael	1998	Exp	303.75	0.7862	
J Kestin	1978	Exp	303.00	0.7960	

Table 4.4: Coefficients of best fit for Eq. (4.7)

Coefficient	unit	value
a	mPa s	0.5818
b	mPa s $\cdot$ K^{-1}	-0.03315
c	mPa s $\cdot$ K^{-2}	2.02072×10^{-4}

Chapter 5

Concentration dependence of shear viscosity of salt solutions

> Chlorine is a deadly poison gas employed on European battlefields in World War I. Sodium is a corrosive metal which burns upon contact with water. Together they make a placid and unpoisonous material, table salt. Why each of these substances has the properties it does is a subject called chemistry.
>
> *Carl Sagan (1934 -1996)*

5.1 Introduction

Physical properties of aqueous solutions have countless practical applications. There is however no easily available source of critically evaluated data. One of the most important thermophysical properties is the viscosity as a function of temperature, pressure, and salt concentration. The viscosity of binary aqueous solutions plays an important role in a variety of fields, including chemistry and chemical engineering, separation processes (crystallization, evaporation, desalination), waste water treatment,and so on.

It has been long recognized that the hydration of ions should have an important effect

on the structure and dynamical properties of aqueous solutions. In particular, it affects the liquid structure and the transport properties of the solutions. Many measurements have been reported on the viscosity of aqueous single electrolyte solutions [40, 41]. In 1996 Zhang et. al. [40] worked on viscosity and density of water + sodium chloride + potassium chloride solutions and designed to extend the Jones-Dole [42] type equations to saturation for single electrolyte solutions.

One of the best ways to gain a better understanding of the interaction of water and salt solutions is molecular dynamics(MD). In fact, MD simulations provide a realistic description at molecular resolving power of structural and dynamical characteristics in an aqueous solution. Over the past several years great progress in computer simulations of aqueous electrolyte solutions using various water models has been achieved. The SPC/E model has been used in computer simulation studies of the thermodynamic and transport properties of ions and uncharged solutes during the past few years [43–48].

In this chapter we discuss the concentration dependent viscosity of salt solutions at the temperature 298 K. Salt solutions are made by changing the number of Na^+ and Cl^- ions in the system. To the best of our knowledge, molecular dynamics simulations of the concentration dependence of viscosities of SPC/E with NaCl have not been reported previously. Inhere, we also present simplest empirical equation to estimate the concentration dependent viscosity of aqueous solutions using experimental data in literature.

5.2 Molecular model

We have used a standard type model in which the intermolecular interactions are expressed as a sum of electrostatic potentials (Chapter 2). The previously described rigid SPC/E (extended simple point charge) model was adopted for the water molecules. The ions are modeled as charged LJ particles. As we have four distinct types of interaction sites for an NaCl solution, it is necessary to consider ten different interactions. The po-

tential parameters for unlike pairs are expressed via the Lorentz-Berthelot (Chapter 2) mixing rules.

The potential parameters used are given in Table 5.1. We used the potential parameters given by Berendsen et al. [2] for SPC/E water model and the potential parameters given by Smith and Dang [44] for sodium and chloride ions.

Table 5.1: Length and energy parameters for NaCl solutions

σ_{OO}	3.17 Å	ϵ_{OO}/k_B	7.82×10^1 K
σ_{HH}	1.80 Å	ϵ_{HH}/k_B	2.00×10^{-4} K
σ_{OH}	2.48 Å	ϵ_{OH}/k_B	1.25×10^{-1} K
σ_{NaNa}	2.73 Å	ϵ_{NaNa}/k_B	4.30×10^1 K
σ_{NaO}	2.88 Å	ϵ_{NaO}/k_B	7.16×10^1 K
σ_{NaH}	2.27 Å	ϵ_{NaH}/k_B	9.27×10^{-2} K
σ_{ClCl}	4.86 Å	ϵ_{ClCl}/k_B	2.02×10^1 K
σ_{ClO}	3.25 Å	ϵ_{ClO}/k_B	6.27×10^1 K
σ_{ClH}	3.33 Å	ϵ_{ClH}/k_B	6.35×10^{-2} K
σ_{NaCl}	3.87 Å	ϵ_{NaCl}/k_B	2.05×10^1 K

The intermolecular potential energy between atom/ions were calculated by Ewald summation Eq.(2.24, 2.22, 2.23 and 2.27), where q_α is the charge of the αth atom or ion here (see Chapter 2 and Appendix D for more details on Ewald summation).

5.3 Simulation details

The simulations were carried out using 1000 molecules at a temperatures of 298 K with salt solutions of different concentrations obtained by changing the number of Na^+ and Cl^- ions in the system. Four different concentrations used in the simulations are given in the Table 5.2. System 2 corresponding to the NaCl salinity of seawater (average salinity of seawater is 35 g/kg) [49].

Systems were simulated with periodic constant NVT boundary conditions. The short

Table 5.2: Concentration of salt solutions

system	$Na^+ ions$	$Cl^- ions$	*Molality*(mol/kg)	*Salinity*(g/kg)
1	6	6	0.33	19.72
2	11	11	0.60	36.52
3	30	30	1.61	103.63
4	72	72	3.67	273.13

range interactions and the real part of the Ewald series were truncated at nearly half the box length, $r_c = 0.48 \times L$. The Coulomb interactions between the partial charges were evaluated using the Ewald interaction. The convergence parameter was $\kappa = 0.97$ and the reciprocal space truncation radius was $k_{max} = 6.0$ in reduced units. All the computations were carried out in reduced units using m_O, σ_O and ϵ_O as the reduction parameters. All the conversions from reduced to real units are given in the Table (see Appendix A).

Equilibrium simulations for systems 1, 2 and 3 for the temperatures of 298 K were performed and the stress acfs were computed with maximum lag times of 25 ps (16 reduced units). For system 4, which has higher concentration, the stress acfs were computed with maximum delay times of 50 ps (32 reduced units) at the same temperature. All the correlation functions decayed to zero within their respective maximum lag times. Systems ran for the total averaging time of 3.6 ns, 6.3 ns, 5.7 ns and 12.6 ns for the systems 1, 2, 3 and 4 respectively.

5.4 Results and discussions

Fig. 5.1, 5.2, 5.3 and 5.4 show the stress acf for systems 1, 2, 3 and 4 respectively at the temperature 298 K.

Fig. 5.5, 5.6, 5.7 and 5.8 show the viscosities of NaCl salt solutions at systems 1, 2, 3 and 4 respectively at the temperature 298 K as a function of time obtained from the normalized Green-Kubo integral given by Eq. (2.4).

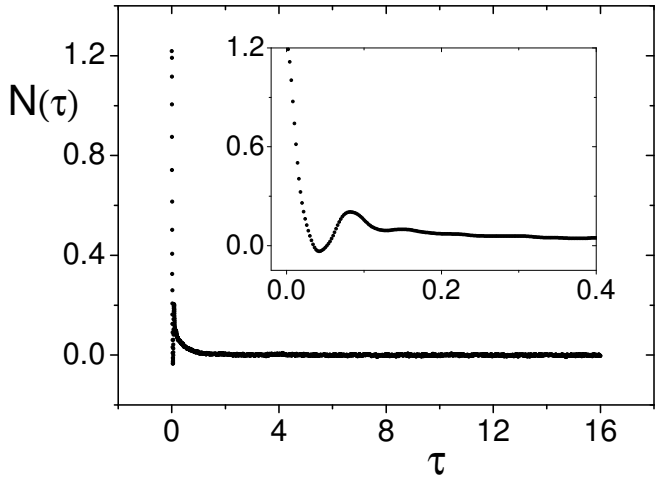

Figure 5.1: Stress auto correlation function for SPC/E + NaCl salt solution at the salinity 19.72 (g/kg). The inset shows the behaviour near zero delay time more clearly.

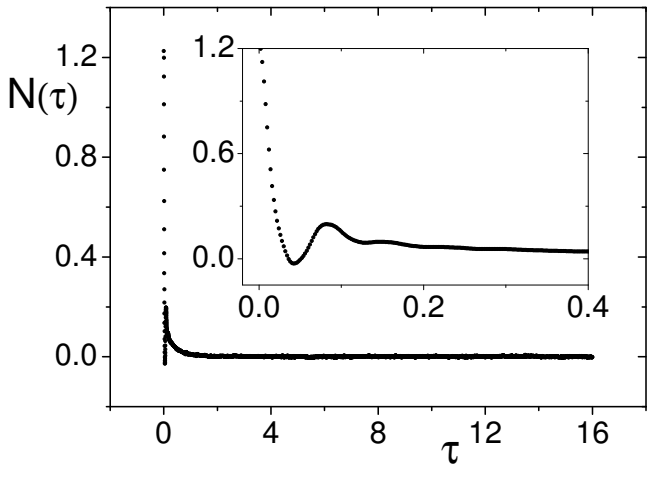

Figure 5.2: Stress auto correlation function for SPC/E + NaCl salt solution at the salinity 36.52 (g/kg). The inset shows the behaviour near zero delay time more clearly.

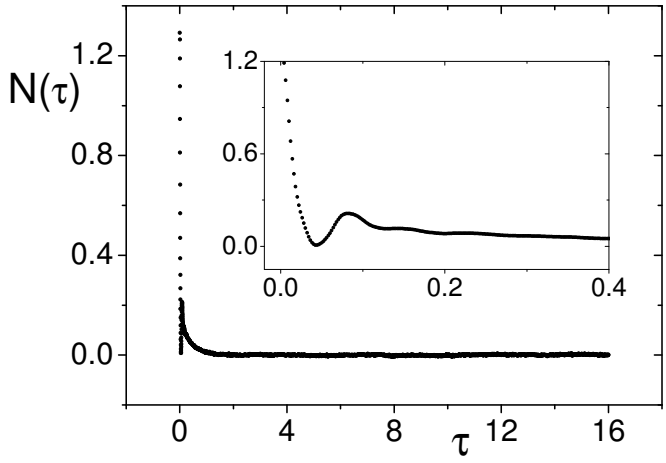

Figure 5.3: Stress auto correlation function for SPC/E + NaCl salt solution at the salinity 103.63 (g/kg). The inset shows the behaviour near zero delay time more clearly.

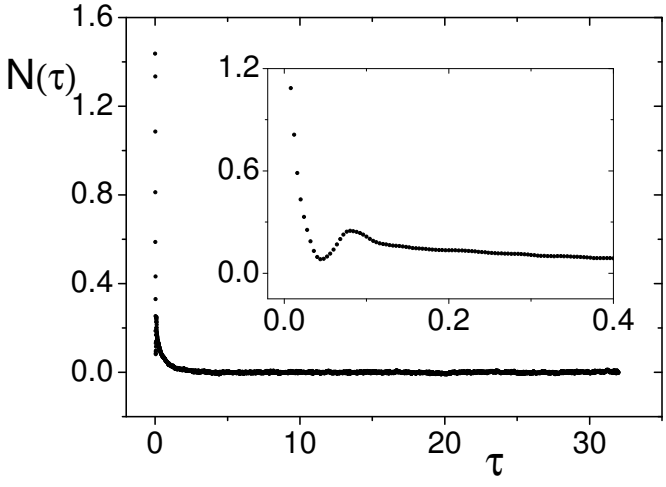

Figure 5.4: Stress auto correlation function for SPC/E + NaCl salt solution at the salinity 273.13 (g/kg). The inset shows the behaviour near zero delay time more clearly.

For convenience, we have defined $N(\tau) = \left\langle \mathbf{P}^{0s}(\tau) : \mathbf{P}^{0s}(0) \right\rangle /10$. Fig. 5.1, 5.2 and 5.3 show the acf up to the maximum delay time of 25 ps (16 reduced units) and Fig. 5.4 shows the acf up to the maximum delay time of 50 ps (32 reduced units) in the main figure and details of the short time decay in the inset. We doubled the maximum delay time for most condensed system to test for long-time slow decay of the acf.

The stress acf displays a minimum, followed by a maximum and then a slow decay to zero. The maximum and minimum are much sharper and the long decay is much faster than for CS_2 (Chapter 3) but the maximum and minimum are not much sharper than the previously simulated pure SPC/E water systems. The long decay is similar to that obtained for pure water, simulated with the SPC/E model.

The stress relaxation depends on the interactions, mass and rotational inertia of the molecules. Compared to the CS_2 molecule, the water molecule has stronger interaction and less mass and also lower rotational inertia. Therefore the stress acf of pure SPC/E model water shows a sharper maximum and minimum than that of CS_2 . Similarly, when comparing NaCl solution with bulk water, the salt solution has heavy Na^+ and Cl^- ions with negligible rotational relaxation. Therefore it gives less sharp minimum and maximum than pure SPCE/E water.

Table 5.3 shows the minimum and maximum values of stress auto correlation (sacf) functions of four systems. All the values are in reduced units. From the table we can see that the minimum and maximum occurs at the same time and it is the same as for the bulk water simulation done in the previous chapter (see chapter 4 table 4.2). For system 1 the difference between maximum and minimum is equal to 0.239 in reduced units. The difference between maximum and minimum is about 0.224 for the system 2, about 0.205 for system 3, and 0.154 for system 4. The results show that as the NaCl concentration increases the difference between the maximum and minimum stress auto correlation func-

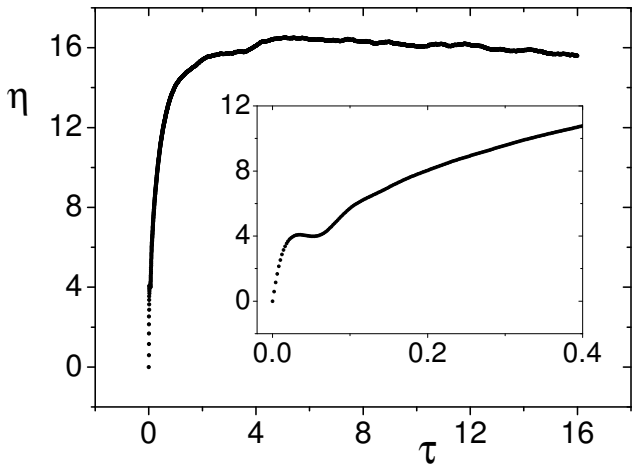

Figure 5.5: Running integral of the stress acf for SPC/E + NaCl salt solution at the salinity 19.72 (g/kg)-system 1. The inset shows the behaviour of the acf near zero delay time.

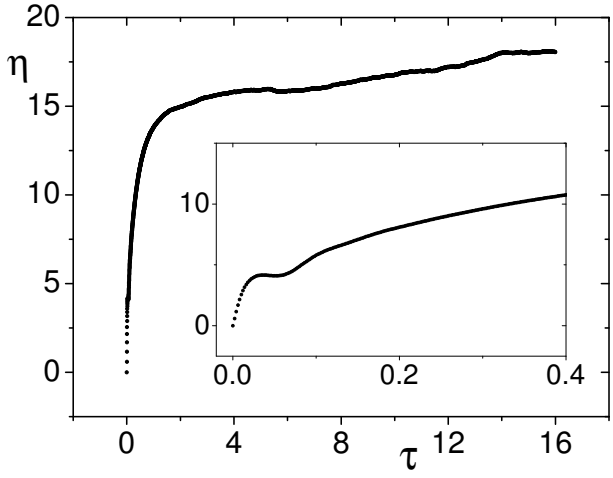

Figure 5.6: Running integral of the stress acf for SPC/E + NaCl salt solution at the salinity 36.52 (g/kg)-system 2. The inset shows the behaviour of the acf near zero delay time.

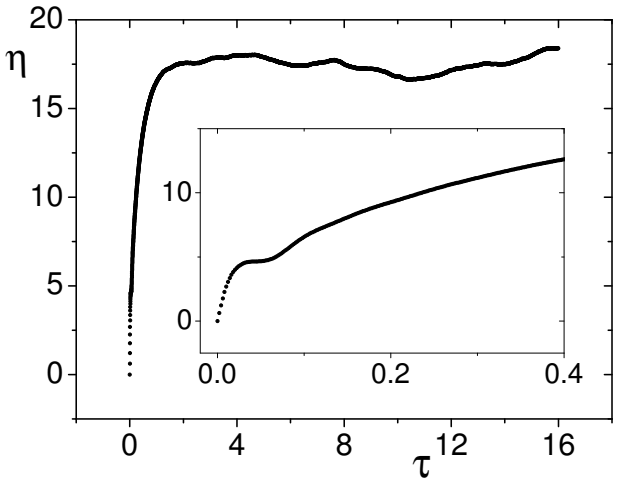

Figure 5.7: Running integral of the stress acf for SPC/E + NaCl salt solution at the salinity 103.63 (g/kg)-system 3. The inset shows the behaviour of the acf near zero delay time.

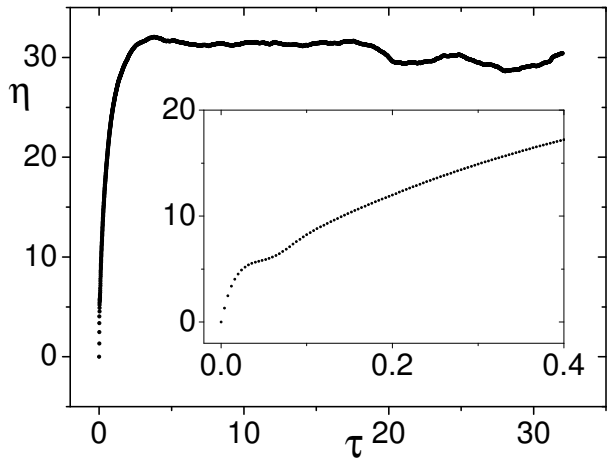

Figure 5.8: Running integral of the stress acf for SPC/E + NaCl salt solution at the salinity 273.13 (g/kg)-system 4. The inset shows the behaviour of the acf near zero delay time.

tions decreases. The local structure of the system may be the reason for this phenomenon.

Table 5.3: Minimum and maximum values of sacf

system	*min/max*	*time*	*sacf*	*error*	$(max - min)$
1	*min*	0.042	-0.035	±0.002	
	max	0.082	0.204	±0.003	0.239
2	*min*	0.042	-0.027	±0.002	
	max	0.082	0.197	±0.002	0.224
3	*min*	0.042	-0.008	±0.003	
	max	0.082	0.213	±0.002	0.205
4	*min*	0.042	-0.095	±0.004	
	max	0.082	0.249	±0.004	0.154

Fig. 5.5, 5.6, 5.7 and 5.8 illustrate that the viscosities have reached a constant value at long time, giving the zero shear rate viscosities of temperature 298 K at the four different concentrations denoted by systems 1 to 4 respectively. From the data the zero shear rate viscosity of the equilibrated NaCl solution system 1 is 15.1 ± 1.8 in reduced units which is equal to $8.1 \pm 0.9 \times 10^{-4}$ Pa s. The viscosity of system 2 converged to a constant value of 17.9 ± 1.4 in reduced units which is equal to $9.6 \pm 0.7 \times 10^{-4}$ Pa s and the viscosity of system 3 converged to a constant value of 18.4 ± 1.48 in reduced units which is equal to $9.8 \pm 0.8 \times 10^{-4}$ Pa s and the viscosity of system 4, which is highly concentrated, converged to a constant value of 31.3 ± 3.8 in reduced units which is equal to $16.7 \pm 2.0 \times 10^{-4}$ Pa s. Figure 5.9 shows the simulation data compared with equation 5.3

As no simulation results exist in the literature, we compare our simulation results with experimental data. In 1996 Zhang et. al. [40] developed an equation (5.1) to calculate the concentration dependence of viscosity of aqueous salt solutions. The coefficients of their equation are given in the Table 5.4.

$$\eta/\eta_0 = 1 + Ac^{0.5} + Bc + Dc^2 + Ec^{3.5} \tag{5.1}$$

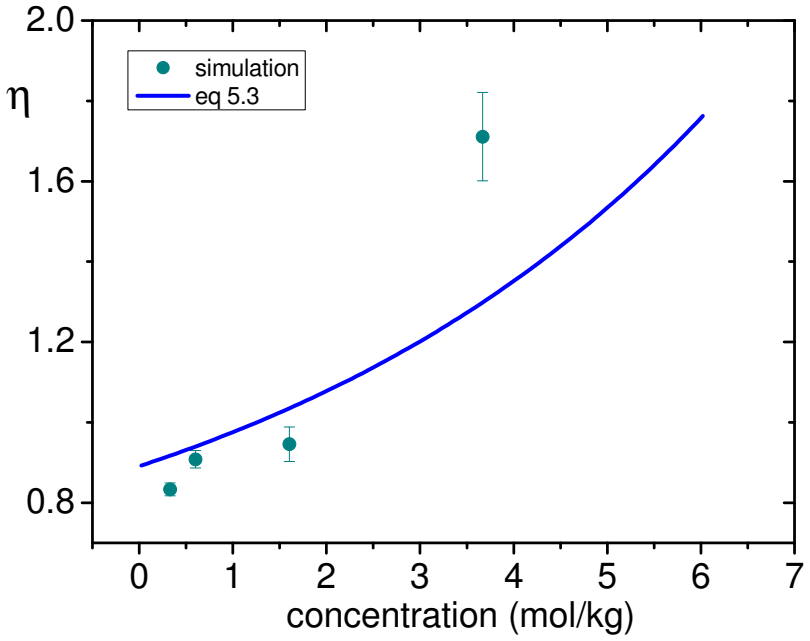

Figure 5.9: Compare the simulation result with the eq 5.3

Table 5.4: Coefficients of best fit for Eq. (5.1)

Coefficient	Zhang	unit
A	0.0061	$(\text{mol/kg})^{-0.5}$
B	0.0794	$(\text{mol/kg})^{-1}$
D	0.01142	$(\text{mol/kg})^{-2}$
E	0.000619	$(\text{mol/kg})^{-3.5}$

In 2010 Yang et. al [50] modified that equation and described the concentration dependence of viscosity more accurately using a more complex formula (Eqn. 5.2). Coefficients to this equation are given in the Table 5.5.

$$\eta = A + Bc^{0.5} + Dc + Ec^{1.5} + Fc^2 + Gc^{2.5} \tag{5.2}$$

Table 5.5: Coefficients of best fit for Eq. (5.2)

Coefficient	Yang	unit
A	0.886628	mPa s
B	0.027908	mPa s $\cdot$ (mol/kg)$^{-0.5}$
D	0.023812	mPa s $\cdot$ (mol/kg)$^{-1}$
E	0.049328	mPa s $\cdot$ (mol/kg)$^{-1.5}$
F	-0.018517	mPa s $\cdot$ (mol/kg)$^{-2.0}$
G	0.006804	mPa s $\cdot$ (mol/kg)$^{-2.5}$

Using the existing data for the concentration dependence of the viscosity we found a simpler and more accurate way of predicting the concentration dependence of the viscosity of NaCl solutions, Eq. 5.3. This new equation has only three coefficients and most importantly the formula we defined for salt solutions is very similar to the equation for temperature dependence of the viscosity of water (Chapter 5). Coefficients of this equation are given in the Table 5.6. The comparison of the deviation between experimental data and Zhang, Yang and our group is shown in the Figure 5.10.

$$\eta = exp(A + Bc + Dc^2) \tag{5.3}$$

Table 5.6: Coefficients of best fit for Eq. (5.3)

Coefficient	Our group	unit
A	-0.11542	$mPas$
B	0.08611	$mPas \cdot (mol/kg)^{-1}$
D	0.00451	$mPas \cdot (mol/kg)^{-2}$

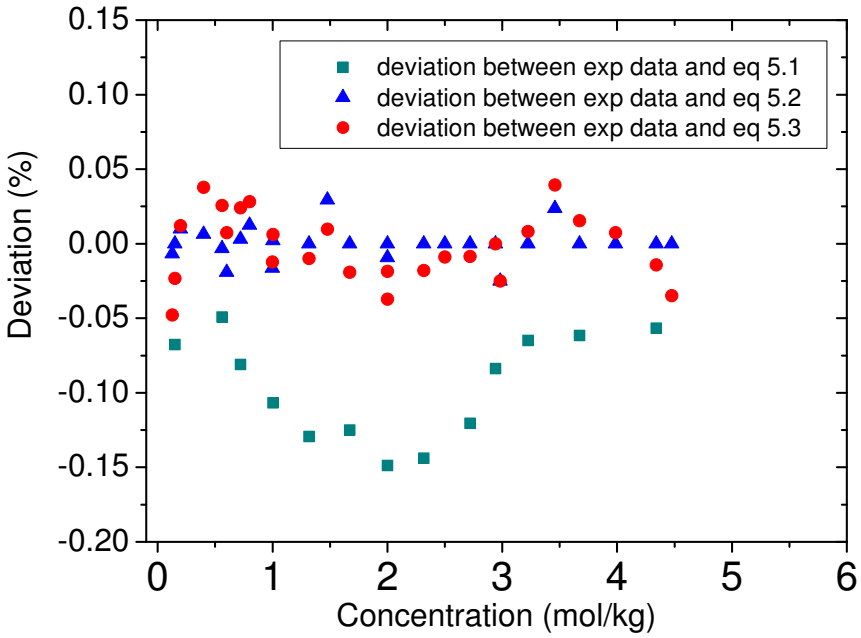

Figure 5.10: Compare the deviation of concentration dependent viscosity of proposed equations with experimental data.

5.5 Conclusion

The concentration dependent viscosity of salt solutions has been calculated by using equilibrium molecular dynamics simulations with Green-Kubo relations. The Ewald summation was used to calculate electrostatic forces and the simulation technique was based on the constraint method described in previous chapters to keep the rigid triatomic structure of the SPC/E model water. The number of Na^+ and Cl^- ions simulated are varied to get the desired salt concentrations of the systems. We have considered four different concentrations one correspondent to the NaCl concentration of sea water [49]. Not only were we able to get good agreement with existing experimental data for the viscosity of salt solutions, we were able to form a simple and generalized equation to fit the experimental data for the concentration dependence of the viscosity.

Chapter 6

Water and salt solutions in silica pores

> A man may imagine things that are false, but he can only understand things that are true, for if the things be false, the apprehension of them is not understanding.
>
> *Isaac Newton (1643 - 1727)*

6.1 Introduction

In recent times a new field of materials science has opened up based on the special properties of amorphous materials. These are substances like glasses, ceramics and even metals which have no long-range order in their structure. These materials possess special properties which make them suitable for technological applications. They are often inexpensive to prepare and their properties can be engineered to suit particular applications. Amorphous silica is one of the most useful materials which has attracted great interest for a wide range of industrial and technological applications.

Amorphous silica is a naturally occurring or synthetically produced oxide of silicon char-

acterized by the absence of pronounced crystalline structure. In particular, due to its unique mechanical and dielectric properties, amorphous silica has become a key material in microelectronics [51]. Many applications of silica materials depend on their surface properties [4, 52], which are largely determined by the functional groups on surfaces through various modification methods. Hydrophilic and hydrophobic functional group concentrations on the silica surfaces are the most significant factor for structural and dynamic properties of liquids at the silica interface [5, 52].

From a fundamental point of view, intracellular water very close to any membrane (vicinal water) shows puzzling behavior as its properties significantly differ from its bulk counterpart. This behavior occurs because vicinal water is organized very differently from bulk water. As a result, much research effort has been devoted to understanding the effect of confinement and surface forces on the thermodynamics and dynamics of water using molecular simulations and experiments. Among the large amount of work published on this topic, several authors have reported studies of water confined in nanoporous silicas with pores of a simple geometry such as slit pores [53, 54] or cylindrical pores [23, 53, 55].

It has recently been suggested that it might be possible to design much more efficient membranes by studying diatoms, which act as natural filters and separators [56–58]. There are many different species of diatoms which give several silica nano-structures. Matthias et al. [57] demonstrated that the one-dimensional pores of a macroporous silicon membrane, etched to exhibit a periodic asymmetric variation in pore diameter, can act as massively parallel and multiply stacked brownian ratchets that are potentially suitable for large-scale particle separations.

Understanding the structure and behavior of liquids near membrane surfaces can clarify a number of phenomena and processes, typically classified as hydrophobic and hydrophilic effects. In 2008, Argyris et. al. [52] investigated the structure and dynamics of water molecules and the hydrogen bonding network that develops when water molecules inter-

act with a solid crystalline substrate. Their results confirmed that for SiO_2 with a low density of hydroxyl groups, the interfacial water shows increased density compared to the bulk. They also suggested that not only the solid surface, but also preferential interaction between interfacial water molecules may result in macroscopic phenomena typically used to discriminate between hydrophobic and hydrophilic surfaces. Realistically, natural membranes do not have a fixed shape and therefore the shape of the pore may affect the structural and dynamical properties of the interfacial water molecules, as well as their rate of exchange with bulk water.

Using our simulation program we have previously carried out molecular dynamics simulations of simple homogeneous systems. Chapter 3 described our calculations of the properties of realistic molecules. There we used a simple linear CS_2 molecule to test and develop our methods. Then we further improved our simulation program to calculate the dynamic and thermodynamic properties of complex systems such as bulk water and salt solutions (Chapter 4 and 5). Finally, in this chapter we are going to describe the properties of inhomogeneous systems using molecular dynamics simulations. In this chapter, we will discuss salt solutions inside amorphous silica pores of varying cross-section.

To understand the effect of a non-cylindrical pore shape, we design an hourglass shaped silica pore for the membrane structure. We used our well established simulation program to investigate the static properties of the fluid inside the pore.

6.2 Models and techniques

6.2.1 Preparation of amorphous silica structure using β-cristobalite basic structure

First, the structure of bulk crystalline silica was generated by repeating the well-known β-cristobalite structure 10 times in the x-direction and 7 times in the y and z directions. The

crystal structure consists of 3920 silicon atoms and 7840 oxygen atoms in a rectangular box (71.66 Å× 50.162 Å× 50.162 Å). Then we applied the melt-quench procedure and created amorphous silica of density 2200 kg/m^3. The structure was melted to form a liquid state at 8000 K; then amorphous silica was obtained by quenching the liquid to 3000 K and the atomic positions were tethered and the system was quenched again to 303 K (Fig. 6.1) to get a realistic amorphous silica structure. Using this bulk amorphous

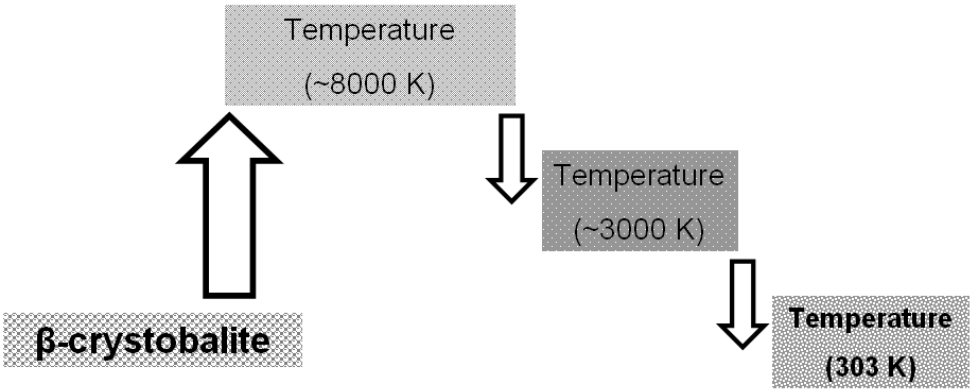

Figure 6.1: Create amorphous silica using β-cristobalite silica

silica block at first, we carved out an hourglass shaped pore using a MATLAB program (The MATLAB program for creating the silica pore is available upon request on CD).

We used the following form to describe the radius of the pore in Å and rotate around the x-axis to get the desired shape of the silica pore,

$$r(x) = e \times exp(-5 \times (x - x_0)^2/1000) + f \tag{6.1}$$

here, x_0 is middle point of the x-direction and e and f are defined constants to get the correct shape. The pore diameter at the ends is equal to 15 Å and the diameter at the centre is equal to 30 Å by selecting e=7.5 and f=7.5.

Secondly, we calculated the silanol number for each of four systems (Table 6.1) according

to the desired silanol surface concentration (Fig. 6.2). Systems 2 & 3 corresponding to the average concentration of the surface hydroxy groups (the silanol number) [3]. We have selected two concentrations of salt solutions to monitor if there is any behavioral changes in salt solutions when the surface silanol number is changing. Both concentrations and densities are close to that of bulk sea water at ambient temperature [49]. Then we identified the correct number of silanol ions for the system by taking the nearest O-atoms to the surface. Finally, we removed unnecessary Si and O atoms on the surface to ensure the simulation box is electro-neutral (Fig. 6.3). The hourglass shape of the pore and x-y side view of the system is shown in the Figure (6.4). The silica has been cut away in the top half of the image to reveal the salt solution.

Table 6.1: Concentration of salt solutions

system	1	2	3	4
OH/nm^2	6.0	4.6	4.6	0
Si	6513	6578	6578	6754
O	3325	3341	3341	3377
OH^-	274	208	208	0
H_2O	600	600	491	491
Na^+	7	7	6	6
Cl^-	7	7	6	6
$mol.kg^{-1}$	0.62	0.62	0.65	0.65
$g.kg^{-1}$	37.9	37.9	39.7	39.7
$mol.l^{-1}$	0.47	0.47	0.41	0.41

Unlike crystalline silica, amorphous silica has no defined constant bond length and bond angle for the Si and O atoms. In 2009, Zhang et. al. [23] carried out molecular dynamics simulations of water confined in a cylindrical nanopore of amorphous silica. In their work they used amorphous silica but assumed that the structure of amorphous silica was characterized by the same Si-O-Si bond length and bond angle as the crystal to classify bridging and non-bridging oxygens. Probably because of this approximation, the number of non-bridging oxygen atoms was found to increase as the pore diameter decreases (refer Table 3 on their paper). However, when the pore diameter decreases the cavity surface

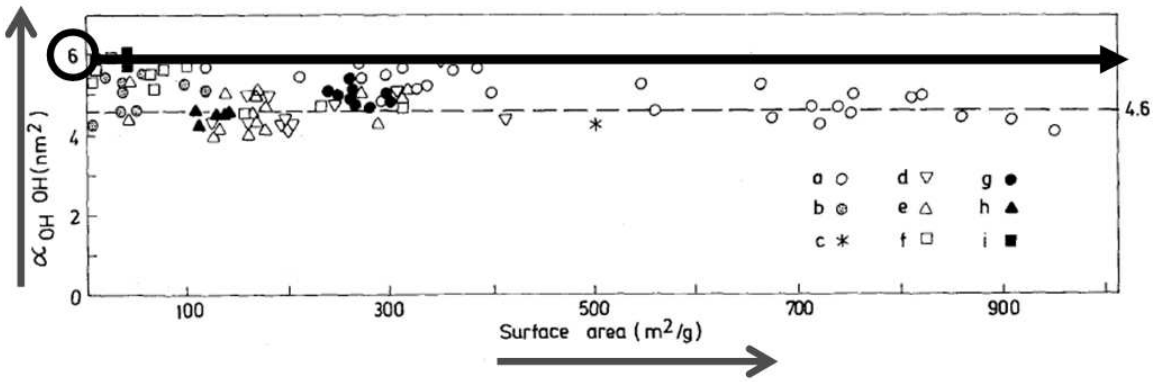

Fig. 2. Concentration of the surface hydroxy groups (the silanol number) α_{OH}, for silicas having different specific surface areas, S, when the surface has been hydroxylated to a maximum degree: a-i - different types of amorphous silica [2]: shaded area - range of experimental data (100 samples of SiO_2 with different S: from 9.5 to 950 m^2/g); dashed lines - average value of the silanol number (231 independent determinations), $\alpha_{OH,av}$=4.6 OH groups/nm^2 (least-squares method)

Figure 6.2: The surface area dependence of silanol number concentration taken from ref. [3] reproduced by permission of the publisher.

area also decreases and therefore the number of non-bridging oxygens should decrease accordingly. It seems that after carving out the pore they have added OH not only to the surface but throughout the whole material to get an electro-neutral system which is not a realistic model for amorphous silica.

To correct the above problems, we have modified their approach. First we select the appropriate silanol number for the cavity surface. We have considered three surface concentrations of silanol groups by changing the number of hydroxyl groups on the wall (Fig. 6.2):
(1) the maximum concentration (6 OH/nm^2)
(2) the average concentration (4.6 OH/nm^2) and
(3) the least concentration (no silanol bonds exist on the wall) of hydroxyl groups found in the silica surfaces [3].

Secondly, we select the volume near the surface by defining a region of slightly larger

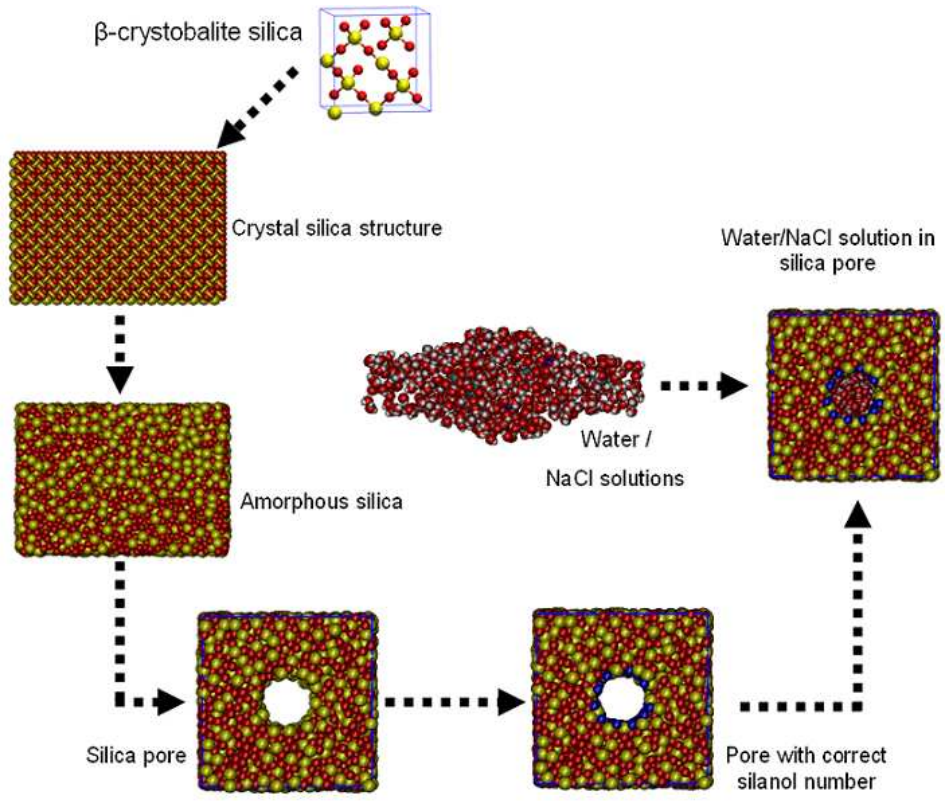

Figure 6.3: Method of creating amorphous silica pore starting with β cristobalite

radius than the pore and mark the oxygen in that region as non-bridging oxygen and other oxygens in the material as bridging oxygen. Then we identify the desired number of hydroxyl groups and number of Si atoms to be removed to get an electro-neutral system. Si atoms are removed from the area we selected before and some of the oxygens near the wall converted to the desired number of hydroxyl groups. Using this process we can create a more realistic amorphous silica pore with less Si atoms near the surface.

The process of creating our electro neutral silica pore is given in a flowchart (Fig. 6.5), which explains how to identify surface silanol ions using the target hydroxyl concentration.

In 2003 Puibasset et al. [59] proposed an algorithm to reproduce vycor like sample using

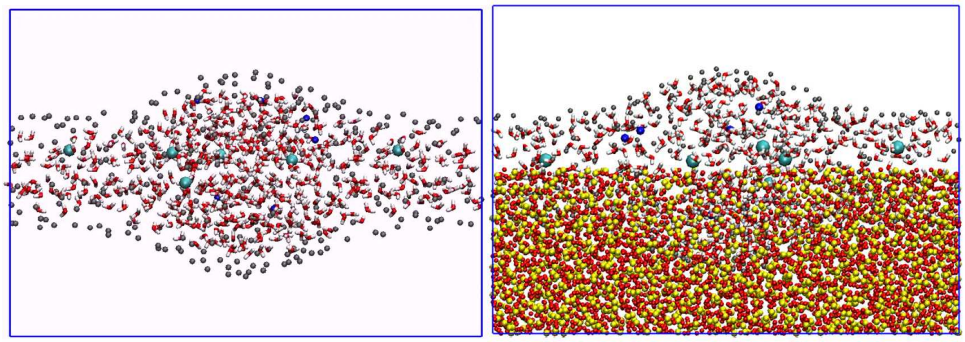

(a) hourglass shape **(b)** x-y side view

Figure 6.4: Introducing pore shape

crystobalite silica. There they have changed the molecular structure on the surface to get correct silanol number, but for the bulk solid they assumed that all silica molecules have the cristobalite structure. Assuming the crystobalite structure for an amorphous material could affect to the liquid behaviour inside the pore. Our algorithm gives a more realistic structure for an amorphous material. Our method also replicates the surface structure of amorphous silica well. Therefore we believe that our method is better for heterogeneous systems than Puibasset et al.'s.

6.3 Simulation details

As shown in the above section we generate four systems of different silanol concentration on the pore surface and two different salt solution concentrations in the pore (see Table 6.1). Systems were simulated as NVT systems with periodic boundary conditions. As these systems consist of many particles, the Coulomb interactions between the partial charges were evaluated using the Wolf method (see Section 2.9) to reduce the computational time. The pair potential parameters of the model are shown in Table (6.2) [53]. bO represents all the bridging oxygens in amorphous silica and we take the electrostatic charge of the bO to be negative and half the value of the Si atom. Unsaturated non-bridging oxygens on the surface need an H^+ ion to be neutralized. Therefore we made a united

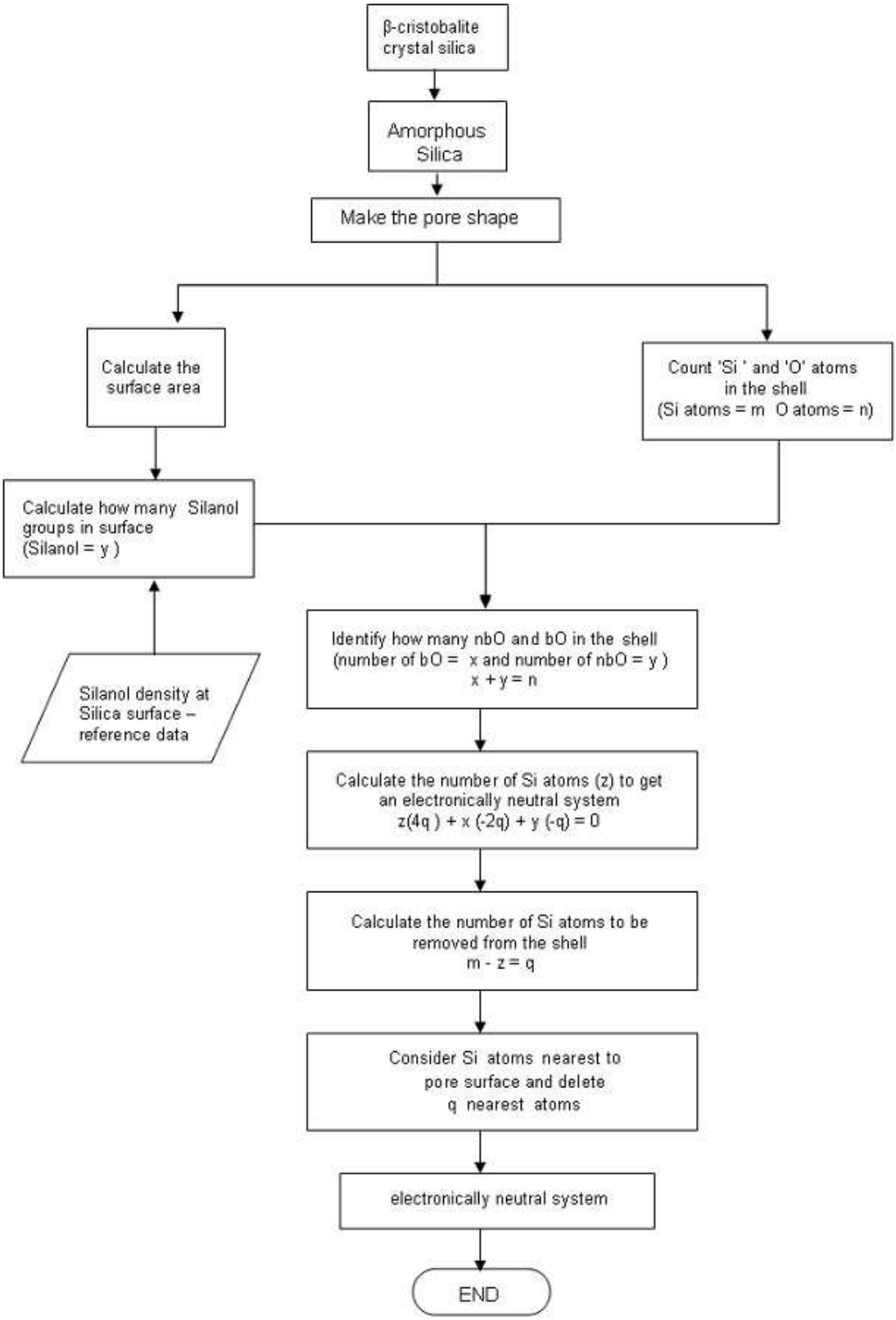

Figure 6.5: The implemented method

atom called nbOH which represents the hydroxyl (OH^-) on the surface. After calculating the number of silanol groups to be placed on the surface we define non-bridging oxygen near to the surface and assign them as united OH ions (hydroxyl group)

The convergence parameter κ is selected as 0.6 in reduced units (1.9 nm^{-1}) to provide an accurate value for the electrostatics calculation (section 2.9) [21]. A higher value of κ takes less computational time but leads to less accurate results [20]. All the computations were carried out in reduced units using m_O, σ_O and ϵ_O as the reduction parameters. All the conversions from reduced to real units are given in Table (A.1)(see Appendix A).

Equilibrium simulations were carried out for all four systems at the temperature of 298 K. We calculated the radial distribution function for a salt solution in the pore and also calculated 3 dimensional histograms of density, temperature, momentum flux in the equilibrated system.

6.4 Results and discussion

The simulation results were analyzed using various methods to understand the salt solution behavior inside the silica pore when the surface silanol density is changing. We used the VMD software [60] to get a clear picture inside the silica pore in the initial and equilibrium states. Tables 6.3 and 6.5 show the initial structure of the pore and salt solutions inside the silica pore. Tables 6.4 and 6.6 show some cross-sectional views of systems 1, 2, 3 and 4 at the equilibrium state. From the figures we can see that the water molecules are more organized and more dense near the wall and therefore a cavity develops in the middle of the pore.

The middle cross-sectional views of concentration profiles in the equilibrium states are shown in the Tables 6.7 and 6.8 using MATLAB. From the figures we can see that the cavity inside the silica pore is bigger when the density of the salt solution inside is lower.

Table 6.2: Length and energy parameters for silica + NaCl solutions

		length Å		energy K
amorphous silica	σ_{Si-Si}	3.80	ϵ_{Si-Si}/k_B	6.42×10^1
	σ_{Si-bO}	3.25	ϵ_{Si-bO}/k_B	1.22×10^2
	σ_{bO-bO}	2.70	ϵ_{bO-bO}/k_B	2.30×10^2
silica-water-wall	$\sigma_{Si-nbOH}$	3.10	$\epsilon_{Si-nbOH}/k_B$	3.71×10^2
	σ_{Si-H}	2.80	ϵ_{Si-H}/k_B	1.13×10^{-1}
	σ_{Si-O}	3.48	ϵ_{Si-O}/k_B	7.09×10^1
	$\sigma_{bO-nbOH}$	2.55	$\epsilon_{bO-nbOH}/k_B$	7.03
	σ_{bO-H}	2.25	ϵ_{bO-H}/k_B	2.14×10^{-1}
	σ_{bO-O}	2.93	ϵ_{bO-O}/k_B	1.34×10^2
	$\sigma_{nbO-nbOH}$	3.00	$\epsilon_{nbO-nbOH}/k_B$	2.30×10^2
	σ_{nbOH-H}	2.10	ϵ_{nbOH-H}/k_B	6.55×10^{-3}
	σ_{nbOH-O}	2.78	ϵ_{nbOH-O}/k_B	4.10
Silica-Na^+Cl^-	σ_{Si-Na}	3.26	ϵ_{Si-Na}/k_B	5.25×10^1
	σ_{Si-Cl}	4.33	ϵ_{Si-Cl}/k_B	3.60×10^1
	σ_{bO-Na}	2.72	ϵ_{bO-Na}/k_B	9.95×10^1
	σ_{bO-Cl}	3.78	ϵ_{bO-Cl}/k_B	6.81×10^1
	$\sigma_{nbOH-Na}$	2.57	$\epsilon_{nbOH-Na}/k_B$	3.04
	$\sigma_{nbOH-Cl}$	3.63	$\epsilon_{nbOH-Cl}/k_B$	2.08
water inside pore	σ_{OO}	3.17	ϵ_{OO}/k_B	7.82×10^1
	σ_{HH}	1.80	ϵ_{HH}/k_B	2.00×10^{-4}
	σ_{OH}	2.48	ϵ_{OH}/k_B	1.25×10^{-1}
Na^+ water	σ_{NaNa}	2.73	ϵ_{NaNa}/k_B	4.30×10^1
	σ_{NaO}	2.95	ϵ_{NaO}/k_B	5.80×10^1
	σ_{NaH}	2.27	ϵ_{NaH}/k_B	9.27×10^{-2}
Cl^- water	σ_{ClCl}	4.86	ϵ_{ClCl}/k_B	2.02×10^1
	σ_{ClO}	4.01	ϵ_{ClO}/k_B	3.97×10^1
	σ_{ClH}	3.33	ϵ_{ClH}/k_B	6.35×10^{-2}
Na^+Cl^-	σ_{NaCl}	3.80	ϵ_{NaCl}/k_B	2.95×10^1

Table 6.3: The structure of systems 1 & 2 - initial state

	6.0 − nbOH	4.6 − nbOH
Inside the pore.	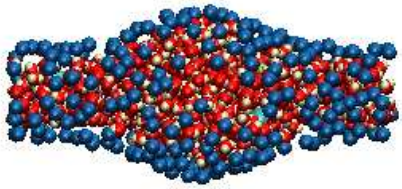	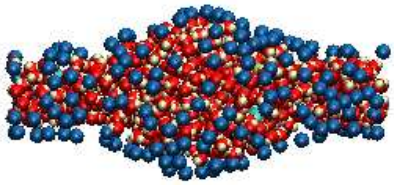
y-z view (30<x<40).	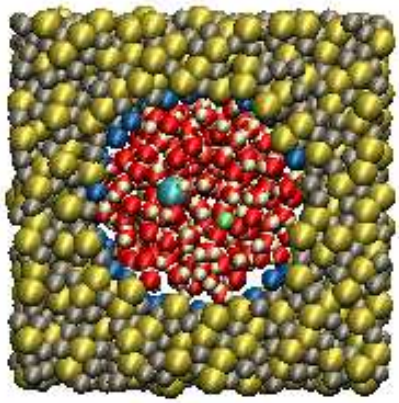	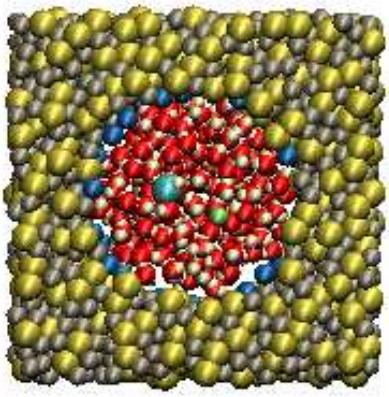
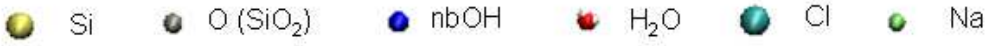		

And also we can see that there is a high molecular concentration near the bottle neck area at the left hand side of the pore and mostly, water molecules cluster near the wall. This shows that the water inside the pore is arranged according to the electrostatic forces of the vessel and as a result of that there are some high density areas and some low density areas in the pore. And also not like in VMD snap shots taken at equilibrium state the concentration data represent the concentration of water calculation throughout the simulation. Therefore, when compare VMD results at equilibrium with MATLAB results, it proves that the water molecules were more ordered like liquid bulk at the initial state (see MATLAB data) and accumulating at the pore surface when it reaches to an equilibrium state (see VMD data).

Table 6.4: The structure of systems 1 & 2 - the equilibrium state

	6.0 − nbOH	4.6 − nbOH
Inside the pore	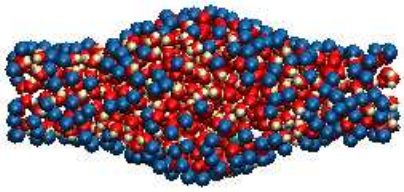	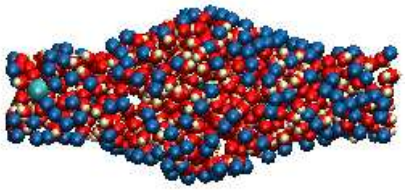
y-z view (0<x<10)	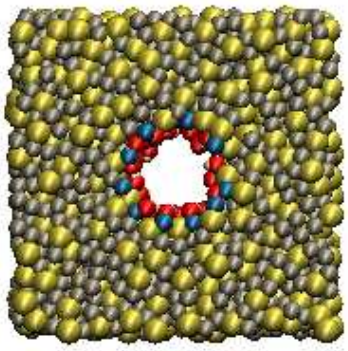	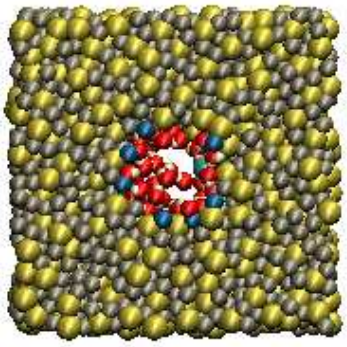
y-z view (10<x<20)	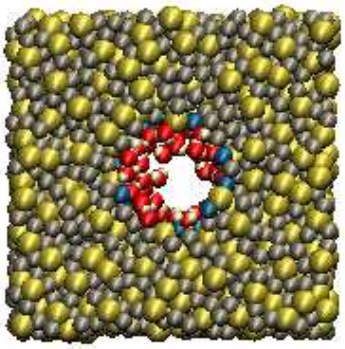	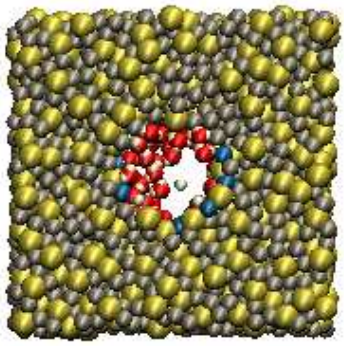

Continued on next page

Table 6.4 – *The structure of systems* 1 & 2 - *the equilibrium state cont.*

	6.0 – nbOH	4.6 – nbOH
y-z view (20<x<30)	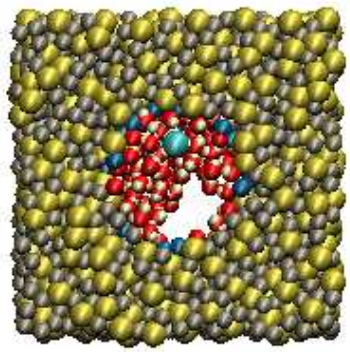	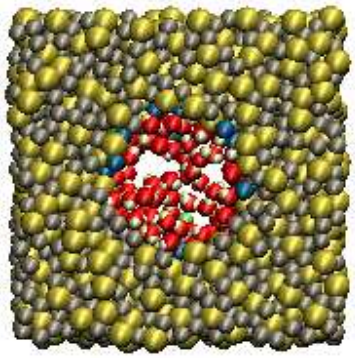
y-z view (30<x<40)	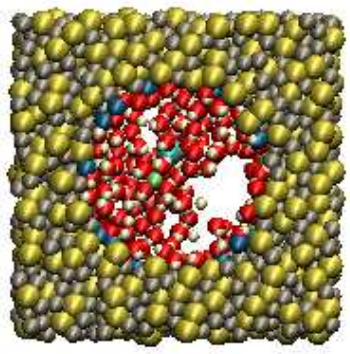	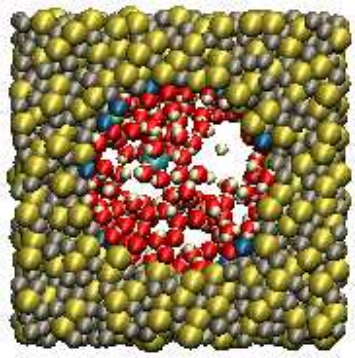
y-z view (40<x<50)	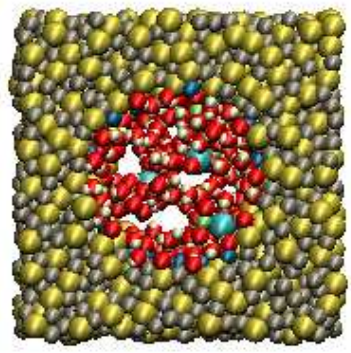	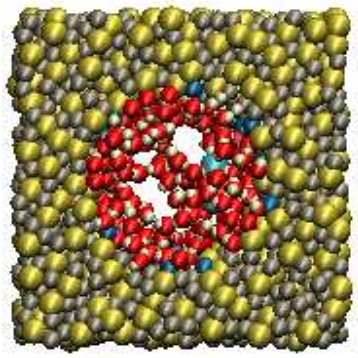

Continued on next page

Table 6.4 – *The structure of systems* 1 & 2 - *the equilibrium state cont.*

	6.0 – nbOH	4.6 – nbOH
y-z view (50<x<60)	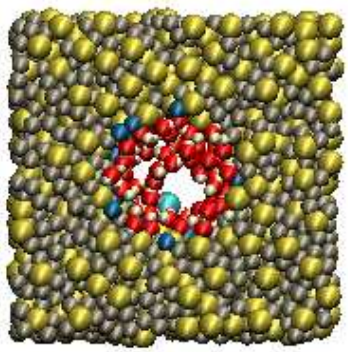	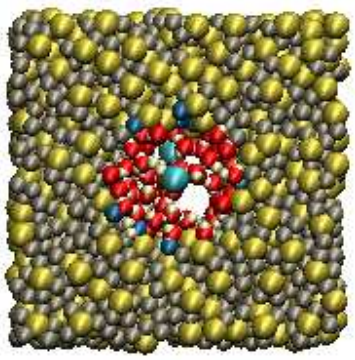
y-z view (60<x<71)	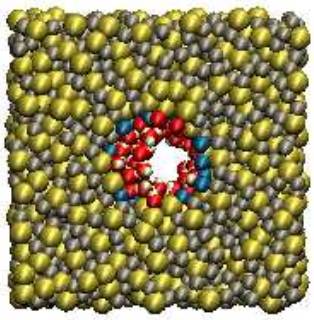	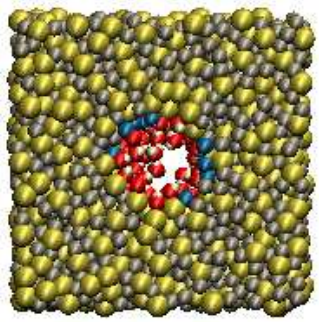

Table 6.5: The structure of systems 3 & 4 - initial state

	4.6 − nbOH	0 − nbOH
Inside the pore.	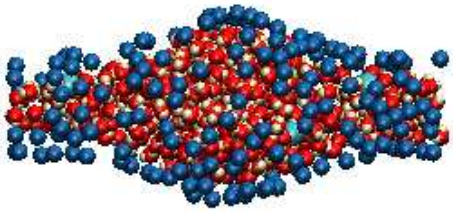	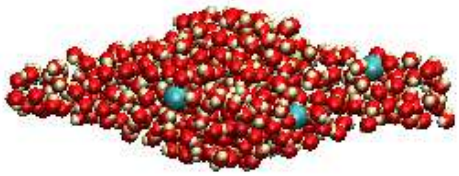
y-z view (30<x<40).	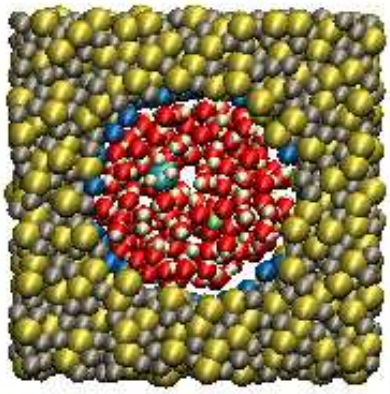	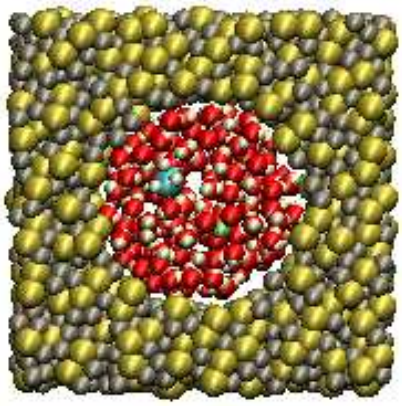
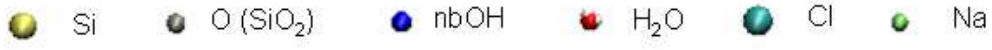		

Table 6.6: The structure of systems 3 & 4 - the equilibrium state

	4.6 − nbOH	0 − nbOH
Inside the pore.	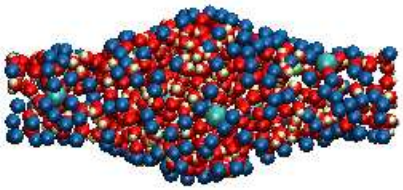	
y-z view (0<x<10)	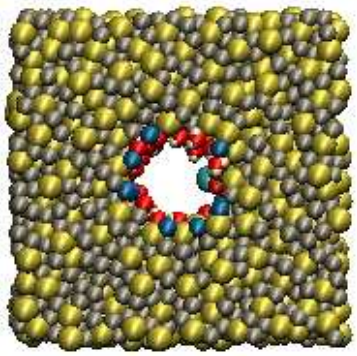	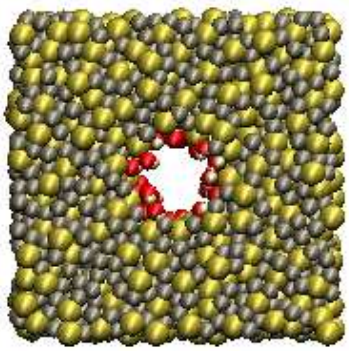
y-z view (10<x<20)	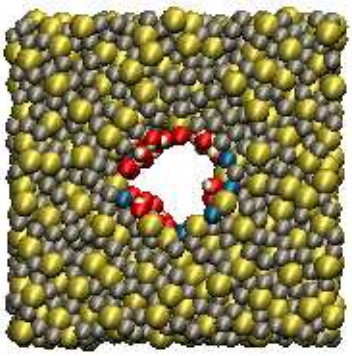	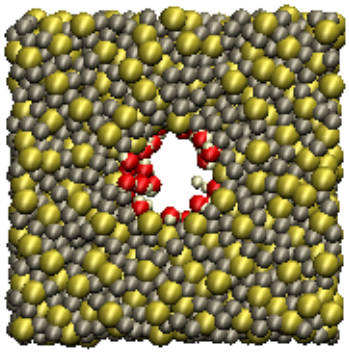

Continued on next page

Table 6.6 – *The structure of systems* 3 & 4 - *the equilibrium state cont.*

	4.6 – nbOH	0-nbOH
y-z view (20<x<30)	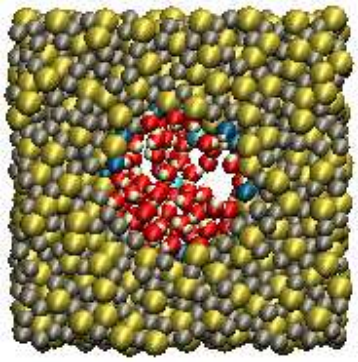	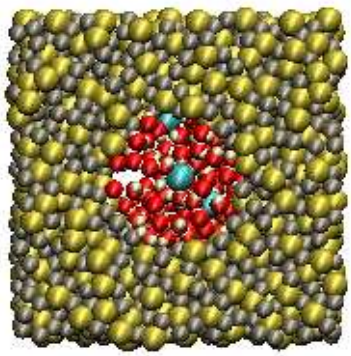
y-z view (30<x<40)	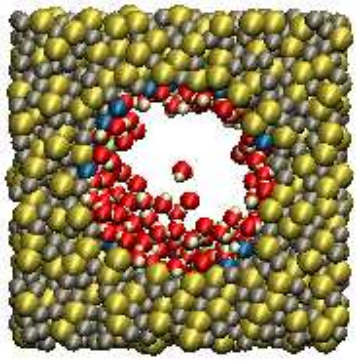	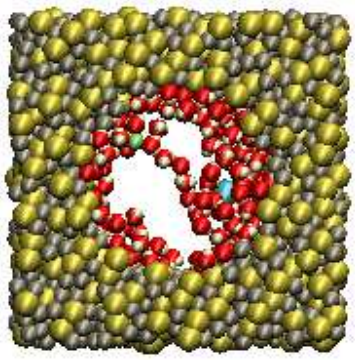
y-z view (40<x<50)	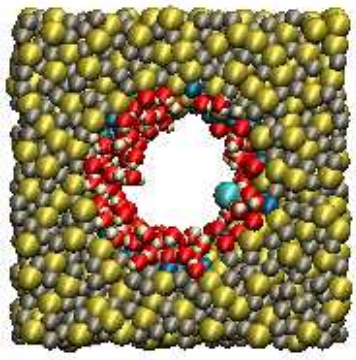	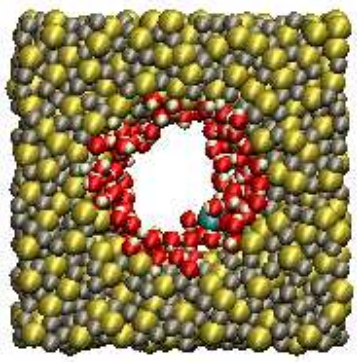

Continued on next page

Table 6.6 – *The structure of systems* 3 & 4 - *the equilibrium state cont.*

	4.6 – nbOH	0-nbOH
y-z view (50<x<60)	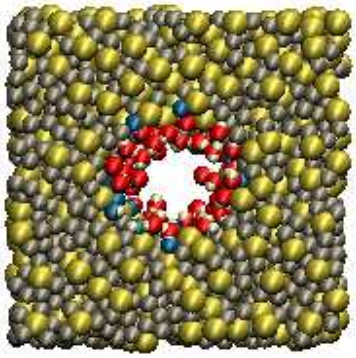	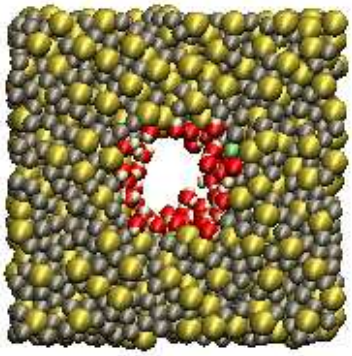
y-z view (60<x<71)	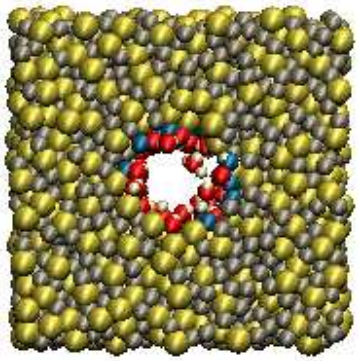	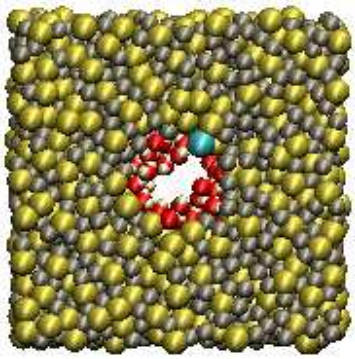

Table 6.7: Concentration of water inside the pore of systems 1 & 2 at equilibrium state in reduced units

	$6.0-$ nbOH	$4.6-$ nbOH
x-y view (z=25).		
y-z view (x=35).		

Table 6.8: Concentration of water inside the pore of systems 3 & 4 at equilibrium state in reduced units

	$4.6-$ nbOH	$0-$ nbOH
x-y view (z=25).	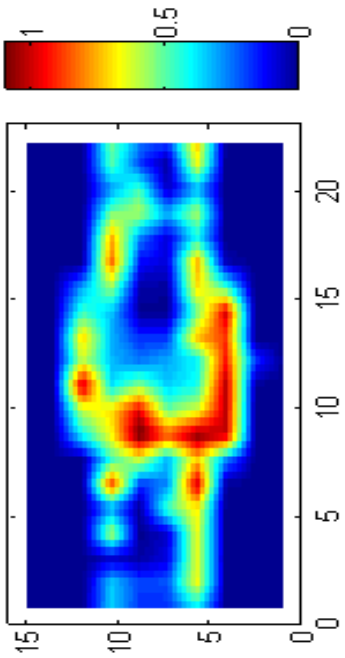	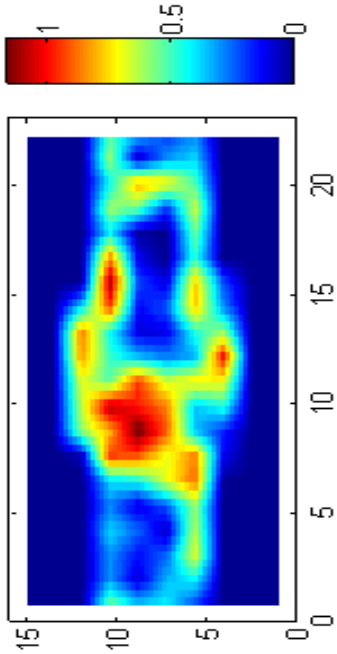
y-z view (x=35).	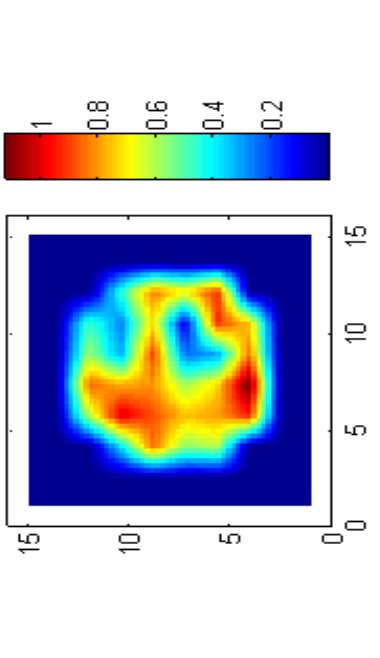	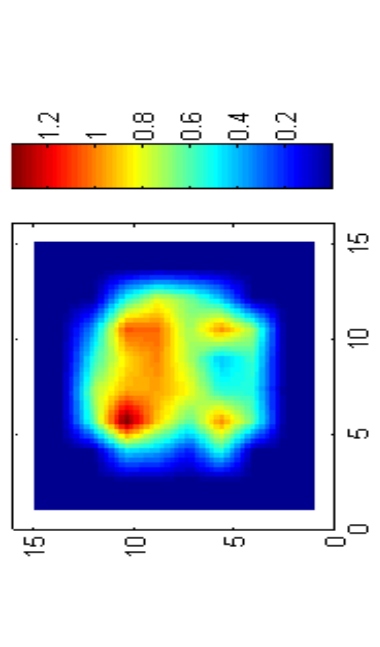

The radial distribution functions, g(r), of the systems are shown in Tables 6.9 and 6.10. The RDFs were calculated using a configuration file at the equilibrium state. Table 6.9 represents the g(r) of the salt solution inside the pore and it is compared with the g(r) of a bulk salt solution which was calculated in previous chapter. The results show that the $g_{OH}(r), g_{HH}(r)$ and $g_{OO}(r)$ of the salt solution inside the pore have higher peak values than the bulk solutions. From those values we can say that the salt solution inside the silica pore is more ordered than the bulk liquid.

The first row of Table 6.10 shows that all four systems are similarly affected by the confinement in the amorphous silica pore. The second row represents hydrogen bonds between surface silanol groups (here OH represents hydroxyl groups formed from the non bridging oxygens at the silica surface) and water H for systems 1, 2, and 3. The $g_{OH\text{-}H}(r)$ depends more strongly on the water concentration in the pore than on the surface silanol number.

Argyris et. al. [52] remarked that the behavior of the water becomes more complex in the case of SiO_2 surfaces. From their result they noticed that even for low density SiO_2 the peaks in the RDFs change shape as well as intensity because the RDFs are representative of the hydrogen-bonding network.

In our systems the salt solution is surrounded by silica. The RDFs for water inside the pore are similar to the results of Argyris et al. but for the RDFs we get higher peaks. That is most probably because the surface affect of the silica is considerably higher than that of Argyris et al and therefore the water molecules are more strongly ordered.

Even though Zhang et al. [23] did their simulations using an unrealistic silica structure the RDFs of water inside the pore were not affected much. The Table 6.11 compares our simulation results for the RDFs of water inside the pore with the results of Zhang et al.

Table 6.9: Salt solution g(r) data of systems

	g(r)
$g_{O\text{-}H}(r)$	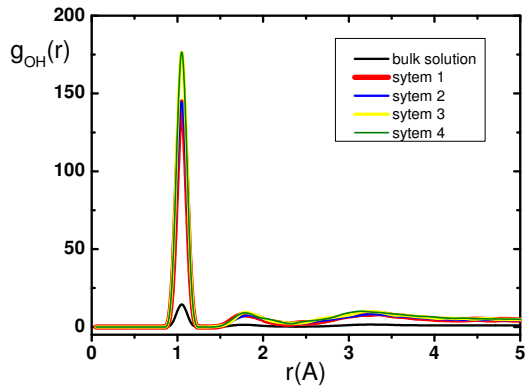
$g_{H\text{-}H}(r)$	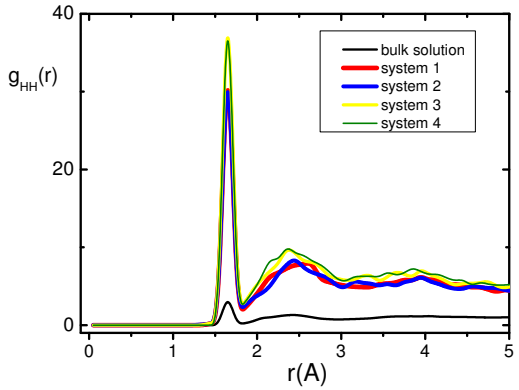
$g_{O\text{-}O}(r)$	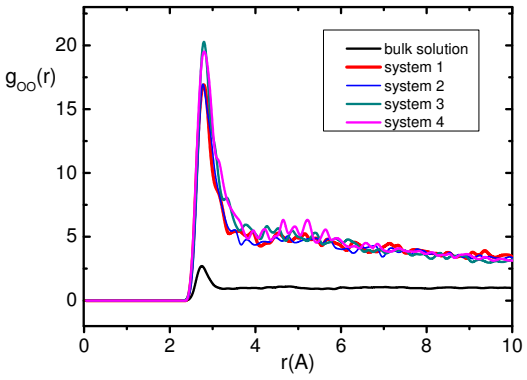

Table 6.10: Amorphous silica and surface g(r) data of systems

	g(r)
$g_{Si\text{-}O}(r)$ (silica pore)	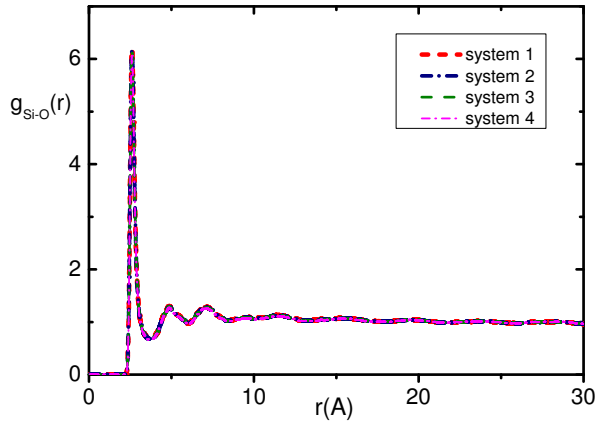
$g_{OH\text{-}H}(r)$ (silica surface)	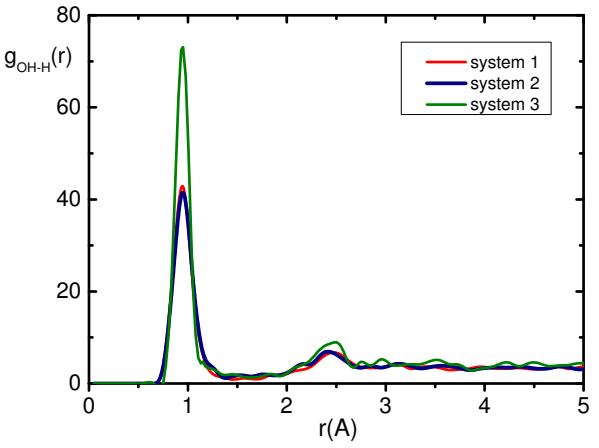

Table 6.11: Comparing the peak position of RDFs of water inside the pore

g(r)	*Peak(simu)*	*Zhang et al.*
O-H	1.05	1.75
H-H	1.65	2.5
O-O	2.75	3.0
Si-O(amo-silica)	4.88	
OH-H (surface)	1.05	

Babu et. al. carried out the molecular dynamics simulations to study the pressure driven fluid flow of water through single walled carbon nanotubes [61] which gave similar results to our. Their work investigated the effect of surface curvature of the nanotubes on viscosity by varying the diameter of nanotubes. They found that the definition of viscosity fails for very small diameter nanotubes since they have only single file transport of water molecules through them. Their computations were performed with nanotube diameters ranging from 8.136 Å to 54.2 Å. They maintained the translational symmetry of the nanotubes by selecting ten translational unit cells as the length of the nanotubes. Their results (see Fig. 4 on their paper) clearly show that only single file transport of water molecules is possible inside the smallest nanotube (see Fig. 4(a) on their paper), but as the diameter is increased they first obtain a concentric tube of water molecules in the medium nanotube (see Fig. 4(b) on their paper), and then a concentric tube of water molecules with a single file inside that in the largest nanotube (see Fig. 4(c) on their paper).

This is similar to what we obtain from our simulations shown in Fig. 6.3, 6.4, 6.5, and 6.6. Fig. 6.3 and 6.5 show that the water is distributed all over the pore at initial stage. Fig. 6.4 and 6.6 show the cross-sections of the pore at different x-positions. The cross-sections at the distance $0 < x < 20$ and also $50 < x < 71$ show that when the diameter is equal to 15 Å water is gathered near the wall and it is similar to the result of Babu et al. (see Fig 4(b) on their paper). Cross-sections at $20 < x < 50$ show that when the pore diameter is larger, water gathered near the walls and also in the centre. This is a similar to the diameter of carbon nanotubes required to give a value for the viscosity consistent with that of the homogeneous, unconfined solution, as found by Babu et al. [61].

Cavities in the salt solutions are irregular comparing to Babu's result. That may be because the structure of amorphous silica is not as requlars as CNTs and it has patchy surfaces. Therefore the intermolecular forces may change with positions. And also $Na^+$and

Cl^- ions are located randomly and the electrostatic field in the pore is effected by that too. That result in an uneven electrostatic field in the nano pore and as a result of it there are some cavity when the salt solution is at equilibrium state and those cavities form leaving 'bridges' (Fig. 6.4, 6.6, 6.4 and 6.6).

From the above arguments we can say realistically that all three possibilities (consider to Fig 4 of Babu et al.) may happen in one pore and therefore we can't treat the fluid inside the silica pore as a bulk fluid.

6.5 Conclusion

We analyzed the adsorption of salt solutions in silica pores using molecular dynamics simulations. We generated four different systems by varying the silanol concentration on the pore surface and the concentration of the salt solution inside the pore. The Coulomb interactions between the partial charges were evaluated using the Wolf method (see Section 2.9). We were able to develop a reliable method to simulate water + NaCl in a silica pore with varying cross-sectional diameter.

From the results we verify that the solution inside the pore behaves differently than it does in the bulk. The solution is not distributed uniformly throughout the pore. From the simulation results for the RDFs of water inside the pore we were able to predict that the water behaves in a state between solid and liquid.

From our simulation results we can predict that a bigger pore with a minimum diameter of approximately 13 molecular diameters ($\approx$ 40 Å) would reduce the effect of the surface on the water inside and that would be a good to examine. This is a similar to the diameter of carbon nanotubes required to give consistence value for the viscosity as found by Babu et al. [61]. It is hoped that in future work it will be possible to examine what will happen when a sodium chloride solution flows through the non-cylindrical pore.

Chapter 7

Conclusion

Science may set limits to knowledge, but should not set limits to imagination.

Bertrand Russell (1872 - 1970)

7.1 Conclusion

The behaviour of fluids in nanopores is complicated and poorly understood. This behaviour results from a complex interplay of surface forces, intermolecular forces and packing effects. For sufficiently small pores, normal continuum fluid behaviour is completely absent. Applications of nanofluidics, such as lab-on-a-chip technology and separation science, require a detailed understanding of these complex issues.

The aim of this project was to study the behaviour of complex fluids in bulk and also to conduct molecular dynamics simulations on systems consisting of sodium chloride solutions inside an amorphous silica nanopore.

Chapter 3 described our calculations of the properties of realistic molecules. There we used a simple linear CS_2 molecule to test and develop our methods.Then we further improved our simulation program to calculate the dynamic and thermodynamic properties

of complex systems such as bulk water and salt solutions (Chapter 4 and 5). In chapter 6 we described the properties of inhomogeneous systems using molecular dynamics simulations. Here we discussed salt solutions inside amorphous silica nanopores which have a cylindrical cross section of varying diameter, forming a continuous bulb-shaped pore.

The viscosity and thermal conductivity of carbon disulphide have been calculated using equilibrium molecular dynamics simulations with the Green-Kubo method. The simulation technique was based on a constraint method which is previously published by Baranyai and Evans. We have made some minor corrections to the constraint equations for molecules with primary and secondary constraints that appeared in the original publication. In addition, the shear rheology has been computed by non-equilibrium molecular dynamics methods, giving excellent agreement between the viscosities calculated by both methods. Both the viscosity and thermal conductivity values were in good agreement with the predictions of an enginaring correlation correlation based on the rough hard sphere model. We managed to calculate the viscosity of carbon disulphide in a wide temperature range, and proposed an empirical equation for the viscosity as a function of temperature.

After ensuring our computational programs were adequate to simulate a rigid non-spherical fluid, we we employed the code to simulate bulk water. The temperature dependent viscosity of SPC/E water has been calculated by using equilibrium molecular dynamics simulations with Green-Kubo relations. Ewald summation was used to calculate electrostatic forces and the simulation technique was based on direct solution of the constraint equations. Here in addition, we were able to form a simple and generalized equation to calculate the temperature dependence of viscosity more accurately using existing experimental results. Also we were able to see the characteristic behaviour of the stress auto correlation function at short times.

Using the same simulation technique we calculated the concentration dependent viscosity of NaCl solutions. The simulation are conducted for water at ambient conditions at

increasing NaCl concentration. The number of Na^+ and Cl^- ions simulated are varied to get the desired salt concentrations of the systems. We have considered four different concentrations, one corresponding to the NaCl concentration of sea water (average salinity of seawater is 35 g/kg) [49]. Here also we were able to form a simple and generalized equation to fit the experimental data for the concentration dependence of the viscosity.

Finally, we analyzed the behaviour of salt solutions in silica pores using molecular dynamics simulations. We generated four different systems by varying the silanol concentration on the pore surface and the concentration of the salt solution inside the pore. The Coulomb interactions between the partial charges were evaluated using the Wolf method (see Section 2.9). We were able to develop a reliable method to simulate water and NaCl in a silica pore with varying cross-sectional diameter.Our results show that the sodium chloride solutions form a complicated network of cavities inside the nanopore. These cavities result from the hydrogen bonding network of the water, combined with the coordination of water around the sodium and chloride ions and the constraints imposed by the confinement. The structural features of these systems are similar to those of water confined in more uniform pores such as carbon nanotubes, but the varying cross-section of the silica pores and the presence of sodium and chloride ions disrupts the tendency of the water molecules to order in a regular network. And also we verify that the solution inside the pore behaves differently than it does in the bulk. From the simulation results for the radial distribution functions of water inside the pore we were able to predict that the water behaves in a state between solid and liquid.

7.2 Suggestions for future work

In Chapter 6 we examined the molecular behaviour of salt solution in silica pore and proved that the liquid inside does not show bulk characteristics when the pore diameter is less than 10-15 molecular diameter of the water molecule. Therefore future work in this project should focus on simulating salt solutions in much bigger silica pores. And also

it is interesting to argue this phenomena using other water models such as TIP4P and TIP5P. It is hoped that in future work it will be possible to examine what will happen when a sodium chloride solution flows through the non-cylindrical pore.

Appendix A

A.1 Reduced units

In order to maintain accuracy in calculations made on computers, operations should involve numbers of similar size. At the atomic level however, there are large differences in the exponents of numbers such as the atomic mass, the potential well depth and the interatomic radius. A new set of units, called reduced units, can be defined by using atomic units for the fundamental quantities of mass (m), energy (ε) and distance (σ). Therefore all the masses are now expressed in units of atomic mass, the energies are in units of the well depth and all distances are in the units of the atomic diameter. Values written in reduced units are typically denoted by an asterisk. The following Table shows how to derive the reduced values of some commonly used properties A.1. where ρ is the

Table A.1: Reduced physical quantities

Physical quantity		value
Length	L^*	L/σ
Energy	U^*	U/ϵ
Density	ρ^*	$\rho\sigma^3$
Temperature	T^*	k_BT/ϵ
Pressure	$\mathbf{P}^*$	$\mathbf{P}\sigma^3/\epsilon$
Time	t^*	$(\epsilon/m\sigma^2)^{1/2}\,t$
Force	F^*	$\sigma F/\epsilon$
Viscosity	η^*	$\sigma^2\eta/\sqrt{(\epsilon m)}$
Shear rate	$\dot{\gamma}^*$	$(m\sigma^2/\epsilon)^{1/2}\,\dot{\gamma}$

number density, k_B is Boltzmann's constant, U is the energy, and t is the time.

Appendix B

B.1 Equations of motion

An exact prescription for deriving equations of motion involving holonomic constraints is given by Gauss' principle of least constraint [12, 14]. This method was extended to the case of molecules with basic and secondary particles by Baranyai and Evans [11]. In this Appendix, we will review their method to define the quantities that appear in the equations of motion. The number of basic particles in each molecule is defined as n_b and the number of secondary particles is defined as n_s. Primed variables refer to secondary particles, Roman letters are used for molecule indices and Greek letters are used for atom (or particle) indices. Holonomic bond length constraints between pairs of basic particles are defined by one constraint equation for each constraint in the molecule, of the form

$$\left(\mathbf{r}_\alpha - \mathbf{r}_\beta\right)^2 = d_{\alpha\beta}^2 \tag{B.1}$$

where, $\alpha > \beta = 1, ..., n_b$ and $\mathbf{r}_\alpha$ and $\mathbf{r}_\beta$ are the positions of basic particles and $d_{\alpha\beta}$ is the constrained distance. The positions of the secondary particles (denoted by primed position vectors, $\mathbf{r'}_\gamma$) can be defined in terms of the position vectors of the basic particles as

$$\sum_{\alpha=1}^{n_b} C_{\gamma\alpha}\mathbf{r}_\alpha - \mathbf{r}'_\gamma = 0 \tag{B.2}$$

where, $\gamma = 1, ..., n_s$ and for each value of γ, the sum of the $C_{\gamma\alpha}$ factors over all values of the basic particle index can be written as

$$\sum_{\alpha=1}^{n_b} C_{\gamma\alpha} = 1 \tag{B.3}$$

The equations of motion for the basic particles at equilibrium can be written as

$$\dot{\mathbf{r}}_{i\alpha} = \frac{\mathbf{p}_{i\alpha}}{m_{i\alpha}} \tag{B.4}$$

$$\dot{\mathbf{p}}_{i\alpha} = \mathbf{F}_{i\alpha}^{LJ} + \mathbf{F}_{i\alpha}^{c} \tag{B.5}$$

where $\mathbf{r}_{i\alpha}$ is the position of particle α of molecule i, $\mathbf{p}_{i\alpha}$ is the thermal momentum of particle α of molecule i, $m_{i\alpha}$ is the particle mass. The total constraint force on particle α of molecule i consists of two terms. The first term is the sum of the direct constraint forces due to other basic particles and the second term is the sum of the constraint forces due to secondary particles

$$\mathbf{F}_{i\alpha}^{c} = \sum_{\delta=1}^{n_c} M_{i\alpha\delta}(\lambda\mathbf{R})_{\delta} - \sum_{\gamma=1}^{n_s} C_{\gamma i\alpha}\boldsymbol{\mu}_{\gamma} \tag{B.6}$$

The index δ has now been redefined to run over all constraints between the basic particles within molecule i, consistent with the notation of Edberg, Evans and Morriss (EEM) [12]. The second term on the right hand side of Eq. (B.6) accounts for the forces on basic particle α of molecule i due to the secondary particles in the same molecule.

From the Eq. (B.4, B.5 and B.6) we get,

$$m_\alpha \ddot{\mathbf{r}}_\alpha = \mathbf{F}_\alpha^{LJ} + \sum_{\delta=1}^{n_c} M_{\alpha\delta}(\lambda\mathbf{R})_\delta - \sum_{\gamma=1}^{n_s} C_{\gamma\alpha}\boldsymbol{\mu}_\gamma \tag{B.7}$$

and the equations of motion for the momenta of the secondary particles can be written as

$$m_\gamma \ddot{\mathbf{r}}'_\gamma = \mathbf{F}'^{LJ}_\gamma + \boldsymbol{\mu}_\gamma \qquad \gamma = 1, \cdots, n_s \tag{B.8}$$

Using Eqs (B.2)and (B.8), we can obtain an equation for the constraint force on a secondary particle

$$\boldsymbol{\mu}_\gamma = m_\gamma \sum_{\alpha=1}^{n_b} C_{\gamma\alpha}\ddot{\mathbf{r}}_\alpha - \mathbf{F}'^{LJ}_\gamma \tag{B.9}$$

Substituting the equation of motion for the primary particle,

$$\boldsymbol{\mu}_\gamma = m_\gamma \sum_{\alpha=1}^{n_b} \frac{C_{\gamma\alpha}}{m_\alpha}\left[\mathbf{F}_\alpha^{LJ} + \sum_{\delta=1}^{n_c} M_{\alpha\delta}(\lambda\mathbf{R})_\delta - \sum_{\gamma=1}^{n_s} C_{\gamma\alpha}\boldsymbol{\mu}_\gamma\right] - \mathbf{F}'^{LJ}_\gamma. \tag{B.10}$$

$$\frac{\boldsymbol{\mu}_\gamma}{m_\gamma} = \sum_{\alpha=1}^{n_b} \frac{C_{\gamma\alpha}}{m_\alpha}\left[\mathbf{F}_\alpha^{LJ} + \sum_{\delta=1}^{n_c} M_{\alpha\delta}(\lambda\mathbf{R})_\delta - \sum_{\gamma=1}^{n_s} C_{\gamma\alpha}\boldsymbol{\mu}_\gamma\right] - \frac{\mathbf{F}'^{LJ}_\gamma}{m_\gamma}$$

$$\frac{\boldsymbol{\mu}_\gamma}{m_\gamma} = -\frac{\mathbf{F}'^{LJ}_\gamma}{m_\gamma} + \sum_{\alpha=1}^{n_b} \frac{C_{\gamma\alpha}}{m_\alpha}\mathbf{F}_\alpha^{LJ} + \sum_{\alpha=1}^{n_b} \frac{C_{\gamma\alpha}}{m_\alpha}\sum_{\delta=1}^{n_c} M_{\alpha\delta}(\lambda\mathbf{R})_\delta - \sum_{\alpha=1}^{n_b} \frac{C_{\gamma\alpha}}{m_\alpha}\sum_{\gamma=1}^{n_s} C_{\gamma\alpha}\boldsymbol{\mu}_\gamma$$

$$\frac{\boldsymbol{\mu}_\gamma}{m_\gamma} + \sum_{\alpha=1}^{n_b} \frac{C_{\gamma\alpha}}{m_\alpha}\sum_{\gamma=1}^{n_s} C_{\gamma\alpha}\boldsymbol{\mu}_\gamma = -\frac{\mathbf{F}'^{LJ}_\gamma}{m_\gamma} + \sum_{\alpha=1}^{n_b} \frac{C_{\gamma\alpha}}{m_\alpha}\mathbf{F}_\alpha^{LJ} + \sum_{\alpha=1}^{n_b} \frac{C_{\gamma\alpha}}{m_\alpha}\sum_{\delta=1}^{n_c} M_{\alpha\delta}(\lambda\mathbf{R})_\delta$$

$$\frac{\boldsymbol{\mu}_\gamma}{m_\gamma} + \sum_{\alpha=1}^{n_b}\sum_{\gamma=1}^{n_s} \frac{C_{\gamma\alpha}}{m_\alpha} C_{\gamma\alpha}\boldsymbol{\mu}_\gamma = T_\epsilon + \sum_{\alpha=1}^{n_b} \frac{C_{\gamma\alpha}}{m_\alpha}\sum_{\delta=1}^{n_c} M_{\alpha\delta}(\lambda\mathbf{R})_\delta$$

where

$$\mathbf{T}_\epsilon = -\frac{\mathbf{F}'^{LJ}_\epsilon}{m_\epsilon} + \sum_{\alpha=1}^{n_b} \frac{C_{\epsilon\alpha}}{m_\alpha}\mathbf{F}_\alpha^{LJ} \tag{B.11}$$

$$\boldsymbol{\mu}_\gamma = \sum_{\epsilon=1}^{n_s} \delta_{\gamma\epsilon}\boldsymbol{\mu}_\epsilon \begin{cases} \boldsymbol{\mu}_\gamma = \delta_{\gamma_1}\boldsymbol{\mu}_1 + \delta_{\gamma_2}\boldsymbol{\mu}_2 + \delta_{\gamma_3}\boldsymbol{\mu}_3 + \ldots\ldots + \delta_{\gamma n_s}\boldsymbol{\mu}_{n_s} \\ \text{if } \gamma = \epsilon \text{ then } \delta_{\gamma\epsilon} = 1 \text{ else } \delta_{\gamma\epsilon} = 0 \therefore \text{ one of them won't be zero i.e. } \delta_{\gamma\gamma}\boldsymbol{\mu}_\gamma = \boldsymbol{\mu}_\gamma \end{cases}$$

$$\frac{\sum_{\epsilon=1}^{n_s}\delta_{\gamma\epsilon}\boldsymbol{\mu}_\epsilon}{m_\gamma} + \sum_{\alpha=1}^{n_b}\sum_{\epsilon=1}^{n_s}\frac{C_{\epsilon\alpha}}{m_\alpha}C_{\epsilon\alpha}\boldsymbol{\mu}_\epsilon = \mathbf{T}_\epsilon + \sum_{\alpha=1}^{n_b}\frac{C_{\epsilon\alpha}}{m_\alpha}\sum_{\delta=1}^{n_c}M_{\alpha\delta}(\lambda\mathbf{R})_\delta$$

$$\sum_{\epsilon=1}^{n_s}\boldsymbol{\mu}_\epsilon\left[\frac{\delta_{\gamma\epsilon}}{m_\gamma} + \sum_{\alpha=1}^{n_b}\frac{C_{\epsilon\alpha}}{m_\alpha}C_{\epsilon\alpha}\right] = \mathbf{T}_\epsilon + \sum_{\alpha=1}^{n_b}\frac{C_{\epsilon\alpha}}{m_\alpha}\sum_{\delta=1}^{n_c}M_{\alpha\delta}(\lambda\mathbf{R})_\delta$$

as,

$$A_{\gamma\epsilon} = \frac{\delta_{\gamma\epsilon}}{m_\gamma} + \sum_{\alpha=1}^{n_b}\frac{C_{\epsilon\alpha}}{m_\alpha}C_{\epsilon\alpha} = A_{\epsilon\gamma} \tag{B.12}$$

$$\sum_{\epsilon=1}^{n_s}\boldsymbol{\mu}_\epsilon\left[A_{\gamma\epsilon}\right] = \mathbf{T}_\epsilon + \sum_{\alpha=1}^{n_b}\frac{C_{\epsilon\alpha}}{m_\alpha}\sum_{\delta=1}^{n_c}M_{\alpha\delta}(\lambda\mathbf{R})_\delta$$

Take,

$$\sum_{\epsilon=1}^{n_s}\boldsymbol{\mu}_\epsilon\left[A_{\gamma\epsilon}\right] = b_\gamma$$

therefore,

$$\sum_{\epsilon=1}^{n_s}\left[A_{\gamma\epsilon}\right]\boldsymbol{\mu}_\epsilon = b_\gamma$$

$$\sum_{\gamma=1}^{n_s}\left[A_{\delta\gamma}^{-1}\right]\sum_{\epsilon=1}^{n_s}\left[A_{\gamma\epsilon}\right]\boldsymbol{\mu}_\epsilon = \sum_{\gamma=1}^{n_s}\left[A_{\delta\gamma}^{-1}\right]b_\gamma$$

$$\sum_{\gamma=1}^{n_s}\sum_{\epsilon=1}^{n_s}\left[A_{\delta\gamma}^{-1}\right]\left[A_{\gamma\epsilon}\right]\boldsymbol{\mu}_\epsilon = \sum_{\gamma=1}^{n_s}\left[A_{\delta\gamma}^{-1}\right]b_\gamma$$

$$\sum_{\gamma=1}^{n_s}\left[A_{\delta\gamma}^{-1}\right]\left[A_{\gamma\epsilon}\right] = \delta_{\gamma\epsilon}$$

$$\sum_{\epsilon=1}^{n_s}\delta_{\gamma\epsilon}\boldsymbol{\mu}_\epsilon = \boldsymbol{\mu}_\delta = \sum_{\gamma=1}^{n_s}\left[A_{\delta\gamma}^{-1}\right]b_\gamma$$

$$\boldsymbol{\mu}_\gamma = \sum_{\epsilon=1}^{n_s}\left[A_{\epsilon\gamma}^{-1}\right]b_\epsilon$$

$$\boldsymbol{\mu}_\epsilon = \sum_{\gamma=1}^{n_s} \left[A^{-1}_{\epsilon\gamma}\right] b_\gamma$$

$$\boldsymbol{\mu}_\gamma = \sum_{\epsilon=1}^{n_s} \left[A^{-1}_{\epsilon\gamma}\right] \left[\mathbf{T}_\epsilon + \sum_{\alpha=1}^{n_b} \frac{C_{\epsilon\alpha}}{m_\alpha} \sum_{\delta=1}^{n_c} M_{\alpha\delta}(\lambda\mathbf{R})_\delta\right]$$

$$\boldsymbol{\mu}_\epsilon = \sum_{\gamma=1}^{n_s} \left[A^{-1}_{\epsilon\gamma}\right] \left[\mathbf{T}_\epsilon + \sum_{\alpha=1}^{n_b} \frac{C_{\epsilon\alpha}}{m_\alpha} \sum_{\delta=1}^{n_c} M_{\alpha\delta}(\lambda\mathbf{R})_\delta\right]$$

$$\boldsymbol{\mu}_\gamma = \sum_{\epsilon=1}^{n_s} \left(A^{-1}\right)_{\gamma\epsilon} \left[\mathbf{T}_\epsilon + \sum_{\alpha=1}^{n_b} \frac{C_{\epsilon\alpha}}{m_\alpha} \sum_{\gamma=1}^{n_c} M_{\alpha\gamma}(\lambda\mathbf{R})_\gamma\right] \tag{B.13}$$

Note that this expression differs from the one appearing in the paper by Baranyai and Evans, due to an erroneous summation in Eq. (6) of the BE paper [11].

$$m_\alpha \ddot{\mathbf{r}}_\alpha = \mathbf{F}^{LJ}_\alpha + \sum_{\delta=1}^{n_c} M_{\alpha\delta}(\lambda\mathbf{R})_\delta - \sum_{\gamma=1}^{n_s} C_{\gamma\alpha} \left[\sum_{\gamma=1}^{n_s} \left[A^{-1}_{\epsilon\gamma}\right] \left[\mathbf{T}_\epsilon + \sum_{\alpha=1}^{n_b} \frac{C_{\epsilon\alpha}}{m_\alpha} \sum_{\delta=1}^{n_c} M_{\alpha\delta}(\lambda\mathbf{R})_\delta\right]\right] \tag{B.14}$$

$$m_\alpha \ddot{\mathbf{r}}_\alpha = \mathbf{F}^{LJ}_\alpha - \sum_{\gamma=1}^{n_s}\sum_{\gamma=1}^{n_s} C_{\gamma\alpha} \left[A^{-1}_{\epsilon\gamma}\right] \mathbf{T}_\epsilon + \sum_{\delta=1}^{n_c} M_{\alpha\delta}(\lambda\mathbf{R})_\delta - \sum_{\gamma=1}^{n_s}\sum_{\gamma=1}^{n_s} C_{\gamma\alpha} \left[A^{-1}_{\epsilon\gamma}\right] \left[\sum_{\alpha=1}^{n_b} \frac{C_{\epsilon\alpha}}{m_\alpha} \sum_{\delta=1}^{n_c} M_{\alpha\delta}(\lambda\mathbf{R})_\delta\right] \tag{B.15}$$

$$\mathcal{F}_\alpha = \frac{\left[\mathbf{F}^{LJ}_\alpha - \sum_{\gamma=1}^{n_s}\sum_{\gamma=1}^{n_s} C_{\gamma\alpha} \left[A^{-1}_{\epsilon\gamma}\right] \mathbf{T}_\epsilon\right]}{m_\alpha} \tag{B.16}$$

$$N_{\alpha\delta} = \frac{\left[M_{\alpha\delta} - \sum_{\gamma=1}^{n_s}\sum_{\gamma=1}^{n_s} C_{\gamma\alpha} \left[A^{-1}_{\epsilon\gamma}\right] \left[\frac{C_{\epsilon\alpha}}{m_\alpha} \sum_{\delta=1}^{n_c} M_{\alpha\delta}\right]\right]}{m_\alpha} \tag{B.17}$$

$$\ddot{\mathbf{r}}_\alpha = \mathcal{F}_\alpha + \sum_{\delta=1}^{n_c} N_{\alpha\delta}(\lambda\mathbf{R})_\delta \tag{B.18}$$

$$\ddot{\mathbf{r}}_\alpha \cdot \mathbf{r}_\alpha = \mathcal{F}_\alpha \cdot \mathbf{r}_\alpha + \sum_{\delta=1}^{n_c} N_{\alpha\delta}(\lambda\mathbf{R})_\delta \cdot \mathbf{r}_\alpha \tag{B.19}$$

To cast the constraint in a form required for treatment using Gauss' Principle, we take the second derivative of Eq.(B.1) and the constraint multipliers, λ are found by solving a set of linear equations that are formulated in a similar way to the original EEM treatment

[11, 12, 14],

$$-\left(\mathcal{F}_\zeta \cdot \mathbf{r}_\zeta + \dot{\mathbf{r}}_\zeta^2\right) = \sum_{\delta=1}^{n_c} \left(\mathbf{r}_\zeta \cdot N_{\zeta\delta}\mathbf{r}_\delta\right) \lambda_\delta \tag{B.20}$$

Note that the equation involves the first derivative and this is shown in the BE paper [11] as a second derivative equation(Eq.15). There is a typographical error in Eq.(14) of the BE paper which has to be corrected as follows.

$$\mathbf{r}_\zeta \cdot \ddot{\mathbf{r}} + \dot{\mathbf{r}}_\zeta^2 = 0 \tag{B.21}$$

where $\mathcal{F}_\zeta = \mathcal{F}_\beta - \mathcal{F}_\alpha$ is the difference in $\mathcal{F}$ between two primary particles in a constraint and

$$\mathcal{F}_\zeta = \frac{\mathbf{F}_\zeta^{LJ} - \sum_{\delta=1}^{n_s} \sum_{\epsilon=1}^{n_s} C_{\epsilon\zeta} \left(A^{-1}\right)_{\delta\epsilon} \mathbf{T}_\delta}{m_\zeta} \tag{B.22}$$

$N_{\zeta\delta}$ is a generalization of the matrix formed from the difference between rows of the constraint matrix that appears in the original EEM formulation, and it is given by

$$N_{\zeta\delta} = \frac{M_{\zeta\delta} - \sum_{\gamma=1}^{n_s} \sum_{\epsilon=1}^{n_s} C_{\epsilon\zeta} \left(A^{-1}\right)_{\gamma\epsilon} \sum_{\alpha=1}^{n_b} \frac{C_{\gamma\zeta}}{m_\zeta} M_{\zeta\delta}}{m_\zeta}. \tag{B.23}$$

For small molecules, any direct method can be used to solve the set of linear equations Eq. (B.20) quite efficiently. For larger molecules, a specialized method for solving linear equations with sparse matrices (e.g. tridiagonal constraint matrices resulting from linear chain molecules) will result in a significant speed-up over general direct methods. As with other constrained equations of motion using the Gaussian constraint method, the inevitable small numerical drift in the constraints was easily controlled by adding very small proportional feedback terms to the position and momentum equations of motion [11].

Appendix C

C.1 Prediction of thermal conductivity of CS_2 by M.J. Assael et al.

The basis of this method is that transport coefficients for real dense fluids are assumed to be directly proportional to values given by exact hard-sphere theory.

This method introduces just two molecular parameters; a characteristic volume v_0 and roughness factor R, which take into account departures from spherical shape and molecular roughness. v_0 is temperature dependent but having the same value for different properties at same temperature. The R factor varies for different properties but is independent of the temperature and density [26].

The relationship between reduced experimental thermal conductivity $\left(\lambda^*_{exp}\right)$ and reduced volume (v_r) is given by:

$$log_{10}\left[\frac{\lambda^*_{exp}}{R_\lambda}\right] = \sum_{i=0}^{4} a_{\lambda i}\left(\frac{1}{v_r}\right)^i \tag{C.1}$$

where, v denotes the molar volume.

The characteristic volume (close-packed volume) of the system is given by the equation:

$$10^6 v_0 = a_0 + a_1 T + a_2 T^2 \tag{C.2}$$

Coefficients of the above equation for CS_2 are shown in the table C.1

Table C.1: The Coefficients used in the Eq. (C.2)

coefficient	value
a_0	40.366
$-10^2 a_1$	2.0017
$10^5 a_2$	-

The inverse of the reduced volume $1/v_r$ for the CS_2 system is equal to 0.681 at 193K and 0.641 for the temperature 309K. The calculated thermal conductivity coefficient (R_λ) from experimental data is equal to 1.67 [26].

Using the appropriate coefficients for $a_{\lambda i}$, giving in the table ($C.2$), we can calculate the reduced coefficient of experimental thermal conductivity λ^*_{exp}.

Table C.2: The Coefficients $a_{\lambda i}$

i	$a_{\lambda i}$
0	1.0655
1	-3.538
2	12.120
3	-12.469
4	4.562

By substituting the value of λ^*_{exp} calculated above value to the Eq. (C.3) we can define the thermal conductivity at the relevant temperature.

$$\lambda^*_{exp} = \frac{64\pi^{1/2}}{75} (2N)^{1/3} \left[\frac{M}{R^3 T}\right]^{1/2} \lambda v^{2/3} \tag{C.3}$$

where N, M, R, T, and v are Avogadro's number, density, gas constant, temperature and molar volume in SI units respectively.

Appendix D

This section is based on the unpublished note in [16].

D.1 Ewald summation

The total electrostatic potential energy is given by the sum over all pairs of particles in the infinite periodic system, excluding interactions between a particle and itself.

$$\Phi^e = \sum_{n=-\infty}^{\infty} \left(\sum_{i=1}^{N} \sum_{j>i}^{N} \frac{q_i q_j}{|\mathbf{r}_{ij} + \mathbf{L_n}|} \right) \tag{D.1}$$

This summation is very slowly convergent and it cannot be truncated to nearest image interactions only. In addition, the infinite sum is conditionally convergent, which means that the result may depend on the order in which the terms are added. Therefore, special methods must be used to compute the sum.

The most common method is the Ewald summation [15], which is described in the books by Allen and Tildesley and Heyes [10]. The Ewald summation method expresses the original sum as two sums. One of these is short ranged and is formulated so as to obey the minimum image convention. This term is rapidly convergent in real space. The remainder can be computed as a Fourier series and it is convergent in reciprocal space.

Since

$$\mathrm{erf}\,(x) + \mathrm{erfc}\,(x) = 1 \tag{D.2}$$

we can write the electrostatic energy for a molecular fluid with charged interaction sites as

$$\Phi^e = \sum_{n=-\infty}^{\infty} \left(\sum_{i=1}^{N} \sum_{\alpha=1}^{N_s} \sum_{j>i}^{N} \sum_{\beta=1}^{N_s} \frac{q_{i\alpha} q_{j\beta}}{|\mathbf{r}_{i\alpha j\beta} + \mathbf{L_n}|} \left(erf\left(\kappa |\mathbf{r}_{i\alpha j\beta} + \mathbf{L_n}|\right) + erfc\left(\kappa |\mathbf{r}_{i\alpha j\beta} + \mathbf{L_n}|\right)\right) \right) \tag{D.3}$$

where,

$$\mathbf{r}_{i\alpha j\beta} = \mathbf{r}_{j\beta} - \mathbf{r}_{i\alpha} \tag{D.4}$$

and treat the summation of both terms separately. Obviously, this decomposition of the electrostatic interaction is not unique, because other functions could be used to split the electrostatic energy in to a rapidly decaying and slowly decaying part, as pointed out by Heyes [18]. Multiplying the potential energy by an error function is equivalent to calculating the potential energy for the interaction between two Gaussian charge distributions rather than two point charges [10].

If the value of κ is chosen so that the minimum image convention can be applied to the real space term (for example so that κL/2=2), only one pair of images will be within the cutoff distance and the sum over all periodic cells reduces to the sum over pairs for which one of the atoms is within the **n**=0 cell and the real space component is written as

$$\Phi^r = \sum_{i=1}^{N} \sum_{\alpha=1}^{N_s} \sum_{j>i}^{N} \sum_{\beta=1}^{N_s} \frac{q_{i\alpha} q_{j\beta}}{d_{i\alpha j\beta}} erfc\left(\kappa d_{i\alpha j\beta}\right) \tag{D.5}$$

where,

$$d_{i\alpha j\beta} = |\mathbf{r}_{i\alpha\beta j} + \mathbf{L_n}| \tag{D.6}$$

$$\mathbf{L}_n = n_x L_x \mathbf{i} + n_y L_y \mathbf{j} + n_z L_z \mathbf{k} \tag{D.7}$$

$d_{i\alpha j\beta}$ is the minimum image separation of the pair $i\alpha j\beta$ that is within the cutoff distance r_c. Note that the self-interactions are excluded and double counting of pairs is avoided by beginning the sum over j at $j > i$.

Only intermolecular interactions are allowed in this expression. Electrostatic interactions between bonded atoms on the same molecule are usually excluded because the bonds are explicitly modeled using either constraint forces or specific bond potentials. For larger molecules containing non-bonded charged atoms, another term allowing for intramolecular interactions should be included. For larger values of κ, at a fixed value of the maximum pair separation L/2, the step of the complementary error function becomes sharper and the real space part of the energy becomes shorter ranged.

The electrostatic potential energy is given by the sum of the real space, Fourier, atomic self interaction correction and the intramolecular bonded atom correction [18].

$$\Phi^e = \Phi^r + \Phi^f - \Phi^s - \Phi^b \tag{D.8}$$

$$\Phi^r = \sum_{i=1}^{N_m}\sum_{\alpha=1}^{N_{s,i}}\sum_{j>i}^{N_m}\sum_{\beta=1}^{N_{s,i}} \frac{q_{i\alpha}q_{j\beta}}{d_{i\alpha j\beta}} erfc\left(\kappa d_{i\alpha j\beta}\right) \tag{D.9}$$

$$2\Phi^f = \frac{4\pi}{V}\sum_{k\neq 0}^{\infty} k^{-2} exp\left[-k^{-2}/4\kappa^2\right] \left|\sum_{i=1}^{N_m}\sum_{\alpha=1}^{N_{s,i}} q_{i\alpha} exp\left(i\mathbf{k}\cdot\mathbf{r}_{i\alpha}\right)\right|^2 \tag{D.10}$$

where,

$$\mathbf{k}_n = 2\pi\left(\frac{n_x}{L_x}\mathbf{i} + \frac{n_y}{L_y}\mathbf{j} + \frac{n_z}{L_z}\mathbf{k}\right) \tag{D.11}$$

$$2\Phi^f = \frac{4\pi}{V}\sum_{k\neq 0}^{\infty} k^{-2} exp\left[-k^{-2}/4\kappa^2\right] \sum_{i=1}^{N_m}\sum_{\alpha=1}^{N_{s,i}} q_{i\alpha} exp\left(-i\mathbf{k}\cdot\mathbf{r}_{i\alpha}\right) \sum_{j=1}^{N_m}\sum_{\beta=1}^{N_{s,i}} q_{j\beta} exp\left(i\mathbf{k}\cdot\mathbf{r}_{j\beta}\right) \tag{D.12}$$

$$\Phi^f = \frac{2\pi}{V}\sum_{k\neq 0}^{\infty} k^{-2} exp\left[-k^{-2}/4\kappa^2\right] \sum_{i=1}^{N_m}\sum_{\alpha=1}^{N_{s,i}} q_{i\alpha} exp\left(-i\mathbf{k}\cdot\mathbf{r}_{i\alpha}\right) \sum_{j=1}^{N_m}\sum_{\beta=1}^{N_{s,i}} q_{j\beta} exp\left(i\mathbf{k}\cdot\mathbf{r}_{j\beta}\right) \tag{D.13}$$

$$\Phi^s = \frac{\kappa}{\sqrt{\pi}} \sum_{i=1}^{N_m} \sum_{\alpha=1}^{N_{s,i}} q_{i\alpha}^2 \tag{D.14}$$

$$\Phi^b = \sum_{i=1}^{N_m} \sum_{\alpha=1}^{N_{s,i}} \sum_{\beta>\alpha}^{N_{s,i}} \frac{q_{i\alpha} q_{i\beta}}{d_{i\alpha i\beta}} erf\left(\kappa d_{i\alpha i\beta}\right) \tag{D.15}$$

The surface term is omitted, assuming metallic boundary conditions (infinite electrical permittivity) on the surface. A more convenient form is found by expressing the complex modulus in the Fourier term as

$$\left| \sum_{i=1}^{N_m} \sum_{\alpha=1}^{N_{s,i}} q_{i\alpha} exp\left(i\mathbf{k}\cdot\mathbf{r}_{i\alpha}\right) \right|^2 = \sum_{i=1}^{N_m} \sum_{\alpha=1}^{N_{s,i}} q_{i\alpha} exp\left(-i\mathbf{k}\cdot\mathbf{r}_{i\alpha}\right) \sum_{j=1}^{N_m} \sum_{\beta=1}^{N_{s,i}} q_{j\beta} exp\left(i\mathbf{k}\cdot\mathbf{r}_{j\beta}\right) \tag{D.16}$$

$$= \sum_{i=1}^{N_m} \sum_{\alpha=1}^{N_{s,i}} q_{i\alpha} Re\left[exp\left(-i\mathbf{k}\cdot\mathbf{r}_{i\alpha}\right) \sum_{j=1}^{N_m} \sum_{\beta=1}^{N_{s,i}} q_{j\beta} exp\left(i\mathbf{k}\cdot\mathbf{r}_{j\beta}\right) \right] \tag{D.17}$$

where we have used the fact that

$$Im\left[\sum_{i=1}^{N_m} \sum_{\alpha=1}^{N_{s,i}} q_{i\alpha} exp\left(-i\mathbf{k}\cdot\mathbf{r}_{i\alpha}\right) \sum_{j=1}^{N_m} \sum_{\beta=1}^{N_{s,i}} q_{j\beta} exp\left(i\mathbf{k}\cdot\mathbf{r}_{j\beta}\right) \right] = 0 \tag{D.18}$$

A further simplification can be made by using the symmetry of the Fourier term with respect to inversion of $\mathbf{k}$. Then only half of the terms need to be computed, and the result is multiplied by two to get the final result. The final result, as it is computed, is:

$$\Phi^f = \frac{2\pi}{V} \sum_{k\neq 0}^{\infty} k^{-2} exp\left[-k^{-2}/4\kappa^2\right] \sum_{i}^{N_m} \sum_{\alpha}^{N_{s,i}} q_{i\alpha} Re\left[exp\left(-i\mathbf{k}\cdot\mathbf{r}_{i\alpha}\right) \sum_{j=1}^{N_m} \sum_{\beta=1}^{N_{s,i}} q_{j\beta} exp\left(i\mathbf{k}\cdot\mathbf{r}_{j\beta}\right) \right] \tag{D.19}$$

where the sum over wavevectors now only goes over those nonzero wavevectors with positive x-components. This is efficiently computed by following Wheeler Fuller and Row-

ley [62] and defining

$$C_n = \frac{2\pi}{V} \frac{exp\left(-k^2/4\kappa^2\right)}{k^2} \tag{D.20}$$

and

$$S\left(\mathbf{k}\right) = \sum_{j=1}^{N_m} \sum_{\beta=1}^{N_{s,i}} q_{j\beta} exp\left(i\mathbf{k} \cdot \mathbf{r}_{j\beta}\right) \tag{D.21}$$

so that the computationally efficient expression for the Fourier series contribution to the internal energy is

$$\Phi^f = \sum_{i=1}^{N_m} \phi_i = \sum_{i=1}^{N_m} \sum_{\alpha=1}^{N_{s,i}} \phi_{i\alpha} = \sum_{i=1}^{N_m} \sum_{\alpha=1}^{N_{s,i}} \sum_{k\neq 0}^{\infty} C_n q_{i\alpha} Re\left[exp\left(-i\mathbf{k} \cdot \mathbf{r}_{i\alpha}\right) S\left(\mathbf{k}\right)\right] \tag{D.22}$$

It is also useful to define

$$\Phi^f = \sum_{k\neq 0}^{\infty} \phi_n \tag{D.23}$$

where

$$\phi_n = \sum_{i=1}^{N_m} \sum_{\alpha=1}^{N_{s,i}} C_n q_{i\alpha} Re\left[exp\left(-i\mathbf{k} \cdot \mathbf{r}_{i\alpha}\right) S\left(\mathbf{k}\right)\right] \tag{D.24}$$

The self-energy term accounts for the fact that the Fourier space energy includes the interaction energy between the Gaussian charge distribution and itself. These interactions should be excluded, because any given charge is not allowed to interact with itself. Such interactions are already excluded in the real space term, but they also need to be subtracted from the Fourier series term. The second correction term (the bonded pair term) accounts for the fact that the Fourier space energy also includes the energies of interaction between bonded pairs of atoms within a molecule and atoms interacting through bending and dihedral potential energy functions. These interactions are also normally excluded. The real space term already excludes them through a molecular interaction mask, but this does not apply to the Fourier space term, so this correction must be added.

D.1.1 Forces

Note: The following properties of the error function are useful here

$$erf\,(x) = \frac{2}{\sqrt{\pi}} \int_0^x e^{-t^2} dt \tag{D.25}$$

$$erfc\,(x) = \frac{2}{\sqrt{\pi}} \int_x^\infty e^{-t^2} dt \tag{D.26}$$

$$erf\,(x) + erfc\,(x) = 1 \tag{D.27}$$

$$\frac{d}{dx} erf\,(x) = \frac{2}{\sqrt{\pi}} e^{-x^2} \tag{D.28}$$

The total electrostatic force on site α of molecule i in the Ewald summation method for a molecular fluid can be expressed as the sum of three terms

$$\mathbf{F}^e_{i\alpha} = \mathbf{F}^r_{i\alpha} + \mathbf{F}^f_{i\alpha} + \mathbf{F}^b_{i\alpha} \tag{D.29}$$

which represent the real space contribution, the Fourier series contribution and a correction to the Fourier series contribution to account for charges within a molecule that are constrained or interacting through a specific bond force.

D.1.2 Real Space term

The real space contribution to the force on site α of molecule i due to interactions with other charged sites is truncated so that it satisfies the minimum image convention and is given by

$$\mathbf{F}_{i\alpha} = -\nabla_{i\alpha} \phi_i \tag{D.30}$$

$$\mathbf{F}^e_{i\alpha} = \mathbf{F}^{e,r}_{i\alpha} + \mathbf{F}^{e,k}_{i\alpha} - \mathbf{F}^{e,b}_{i\alpha} \tag{D.31}$$

The real space series contribution to the force is given by $\mathbf{F}_{i\alpha}^{e,r}$ and the the reciprocal space series contribution the force is given by $\mathbf{F}_{i\alpha}^{e,k}$. We have,

$$\frac{\partial}{\partial x}\left[\kappa\frac{erfc(x)}{x}\right] = \kappa^2 \quad \frac{x\left(\frac{-2}{\sqrt{\pi}}exp(-x^2) - erfc(x)\right)}{x^2} \tag{D.32}$$

where,

$$x = \kappa|\mathbf{r}_{i\alpha j\beta} + \mathbf{L_n}| \tag{D.33}$$

$$\mathbf{F}_{i\alpha}^{e,r} = \sum_{j>i}^{N}\sum_{\beta=1}^{N_{s,j}} \frac{q_{i\alpha}q_{i\beta}\mathbf{d}_{i\alpha j\beta}}{d_{i\alpha j\beta}^2}\left(\frac{erfc\left(\kappa d_{i\alpha j\beta}\right)}{d_{i\alpha j\beta}} + \frac{2\kappa}{\sqrt{\pi}}exp\left(-\kappa^2 d_{i\alpha j\beta}^2\right)\right) \tag{D.34}$$

The Fourier space term is

$$\mathbf{F}_{i\alpha}^{e,k} = -\frac{2\pi}{V}\sum_{k\neq 0}^{\infty}\mathbf{k}k^{-2}exp\left[\frac{-k^2}{4\kappa^2}\right]q_{i\alpha}Im\left[exp\left(-i\mathbf{k}\cdot\mathbf{r}_{i\alpha}\right)\sum_{i=1}^{N_m}\sum_{\beta=1}^{N_{s,i}}q_{i\beta}exp\left(i\mathbf{k}\cdot\mathbf{r}_{i\beta}\right)\right] \tag{D.35}$$

$$= -\frac{4\pi}{V}\sum_{k\neq 0}^{\infty}\mathbf{k}k^{-2}exp\left[\frac{-k^2}{4\kappa^2}\right]q_{i\alpha}Im\left[exp\left(-i\mathbf{k}\cdot\mathbf{r}_{i\alpha}\right)\sum_{i=1}^{N_m}\sum_{\beta=1}^{N_{s,i}}q_{i\beta}exp\left(i\mathbf{k}\cdot\mathbf{r}_{i\beta}\right)\right] \tag{D.36}$$

We can express this in a more efficiently computed form as

$$\mathbf{F}_{i\alpha}^{e,k} = -2\sum_{k\neq 0}^{\infty}\mathbf{k}C_n q_{i\alpha}Im\left[exp\left(-i\mathbf{k}\cdot\mathbf{r}_{i\alpha}\right)S\left(\mathbf{k}\right)\right] \tag{D.37}$$

This includes interactions between all charges. Again, a correction to allow for bonded atoms that do not interact electrostatically within a molecule must be added [17]:

$$\mathbf{F}_{i\alpha}^{e,b} = -\sum_{\beta\in bonded}^{N_{s,j}}\frac{q_{i\alpha}q_{i\beta}\mathbf{d}_{i\alpha j\beta}}{d_{i\alpha j\beta}^2}\left(\frac{erfc\left(\kappa d_{i\alpha j\beta}\right)}{d_{i\alpha j\beta}} - \frac{2\kappa}{\sqrt{\pi}}exp\left(-\kappa^2 d_{i\alpha j\beta}^2\right)\right) \tag{D.38}$$

where the summation extends over atoms excluded from interacting electrostatically with atom α within molecule i. There is no force due to the self-interaction term because the

self-interaction potential energy does not depend on the positions.

D.1.3 Pressure tensor

The Fourier series term of pressure tensor is given by:

$$V\mathbf{P}^{e,k} = \sum_{k\neq 0}^{\infty} C_n \left[1 - 2\mathbf{k_n}\mathbf{k_n}\left(\frac{1}{k_n^2} + \frac{1}{4\kappa^2}\right)\right] \sum_{i}^{N}\sum_{j}^{N} q_i q_j exp\left(i\mathbf{k}_n \cdot \mathbf{r}_{ij}\right) \tag{D.39}$$

which can also be written as

$$V\mathbf{P}^{e,k} = \sum_{k\neq 0}^{\infty}\sum_{i}^{N} C_n \mathbf{B}_n q_i Re\left[exp\left(i\mathbf{k}_n \cdot \mathbf{r}_i\right) S\left(\mathbf{k_n}\right)\right] \tag{D.40}$$

or, due to its similarity to the calculation of the internal energy,

$$V\mathbf{P}^{e,k} = \frac{1}{V}\sum_{k\neq 0}^{\infty} \phi_n \mathbf{B}_n \tag{D.41}$$

with

$$\phi_n = \sum_{i}^{N} C_n q_i Re\left[exp\left(i\mathbf{k}_n \cdot \mathbf{r}_i\right) S\left(\mathbf{k_n}\right)\right] \tag{D.42}$$

$$S\left(\mathbf{k_n}\right) = \sum_{i}^{N} q_i exp\left(i\mathbf{k}_n \cdot \mathbf{r}_i\right) \tag{D.43}$$

For a molecular fluid, the electrostatic interactions between bonded atoms are usually eliminated, and replaced by either bond constraints or specific bond forces. In the real space part of the pressure tensor, these terms are eliminated by applying an interaction mask to the pairs of atoms that are bonded. The Fourier space part as written above would include these contributions, so they must be excluded by adding the following term

to the Fourier space pressure tensor,

$$V\mathbf{P}^{e,k} = -\sum_{i}^{N_m}\sum_{\alpha}^{N_{s,i}} \mathbf{r}_{i\alpha}\mathbf{F}_{i\alpha}^{F,b} \tag{D.44}$$

The expression for the electrostatic contribution to the pressure tensor for a molecular fluid in the molecular representation given by Wheeler [17] following Alejandre [34]. It consists of the usual expression for the molecular pressure tensor due to the short ranged part of the electrostatic potential, plus the following expression for the Fourier space part

$$V\mathbf{P}^{(M)e,k} = \sum_{k\neq 0}^{\infty} \phi_n \mathbf{B}_n - \sum_{i}^{N_m}\sum_{\alpha}^{N_{s,i}} \mathbf{r}_{i\alpha}\mathbf{F}_{i\alpha}^{e,k} - \sum_{i}^{N_m}\sum_{\alpha}^{N_{s,i}} \mathbf{r}_{i}\mathbf{F}_{i\alpha}^{e,k} \tag{D.45}$$

$$= \sum_{k\neq 0}^{\infty} \phi_n \mathbf{B}_n - \sum_{i}^{N_m}\sum_{\alpha}^{N_{s,i}} \left(\mathbf{r}_{i\alpha}\mathbf{r}_{i}\right)\mathbf{F}_{i\alpha}^{e,k} \tag{D.46}$$

where

$$\mathbf{B_n} = 1 - 2\mathbf{k_n}\mathbf{k_n}\left(\frac{1}{k_n^2} + \frac{1}{4\kappa^2}\right) \tag{D.47}$$

This is essentially the expression given by Alejandre, Tildesley and Chapela [34], which corrects minor errors in those given by Heyes [18] and Nose and Klein [63]. However, note the order of the force and position vectors in the dyadic product in the last term is different from that given by Alejandre et al. This could be important when the antisymmetric part of the molecular pressure tensor is of interest.

Appendix E

E.1 Mathematical form of pore shape

We used the following form of exponential equation and rotate around the x-axis to get the desired shape of the silica pore.

$$r(x) = e \times exp(-5 \times (x - x_0)^2/1000) + f \tag{E.1}$$

here, x_0 is middle point of the x-direction and e and f are defined constants to get the correct shape. In this equation, e=7.5 and f=7.5 which gives the minimum diameter of the pore equals to $15\mathring{A}$ and the maximum equals to $30\mathring{A}$. Used calculus method to calculate the pore surface area and pore volume.

Bibliography

[1] D. J. Tildesley and P. A. Madden. An effective pair potential for liquid carbon-disulfide. *Molecular Physics*, 42(5):1137–1156, 1981.

[2] H. J. C. Berendsen, J. R. Grigera, and T. P. Straatsma. The missing term in effective pair potentials. *Journal of Physical Chemistry*, 91(24):6269–6271, 1987.

[3] L. T. Zhuravlev. Characterization of amorphous silica surface. *React. Kinet. Catal. Lett.*, 50(1-2):15, 1993.

[4] D. A. Stenger, J. H. Georger, C. S. Dulcey, J. J. Hickman, A. S. Rudolph, T. B. Nielsen, S. M. McCort, and J. M. Calvert. Coplanar molecular assemblies of amino- and perfluorinated alkylsilanes: characterization and geometric definition of mammalian cell adhesion and growth. *J. Am. Chem. Soc.*, 114:8435, 1992.

[5] R. Wang, K. Hashimoto, A. Fujishima, M. Chikuni, E. Kojima, A. Kitamura, M. Shimohigoshi, and T. Watanabe. Light-induced amphiphilic surfaces. *Nature*, 388:431, 1997.

[6] D. J. Evans and G. P. Morriss. *Statistical mechanics of nonequilibrium liquids*. Second Edition,Cambridge University Publications. Cambridge University Press, Cambridge, 2008.

[7] P. J. Daivis and D. J. Evans. Comparison of constant-pressure and constant volume nonequilibrium simulations of sheared model decane. *Journal of Chemical Physics*, 100(1):541–547, 1994.

[8] D. J. Evans and S. Murad. Singularity free algorithm for molecular-dynamics simulation of rigid polyatomics. *Molecular Physics*, 34(2):327–331, 1977.

[9] G. Ciccotti, M. Ferrario, and J. P. Ryckaert. Molecular-dynamics of rigid systems in cartesian coordinates a general formulation. *Molecular Physics*, 47(6):1253–1264, 1982.

[10] M. P. Allen and D. J. Tildesley. *Computer simulation of liquids*. Oxford Science Publications. Oxford University Press, New York, 1989.

[11] A. Baranyai and D. J. Evans. New algorithm for constrained molecular-dynamics simulation of liquid benzene and naphthalene. *Molecular Physics*, 70(1):53–63, 1990.

[12] R. Edberg, D. J. Evans, and G. P. Morriss. Constrained molecular-dynamics - simulations of liquid alkanes with a new algorithm. *Journal of Chemical Physics*, 84(12): 6933–6939, 1986.

[13] D. J. Evans and G. P. Morriss. Non-newtonian molecular dynamics. *Computer Physics Reports*, 1(6):297–343, 1984.

[14] G. P. Morriss and D. J. Evans. A constraint algorithm for the computer-simulation of complex molecular liquids. *Computer Physics Communications*, 62(2-3):267–278, 1991.

[15] P. P. Ewald. Die berechnung optischer und elektrostatischer gitterpotentiale. *Annalen der Physik*, 369(3):253, 1921.

[16] P. J. Daivis. Calculations of fourier space component of electrostatic interaction energy and forces. *Unpublished Note*, 2010.

[17] D. R. Wheeler and R. L. Rowley. Shear viscosity of polar liquid mixtures via non-equilibrium molecular dynamics: water, methanol, and acetone. *Molecular Physics*, 94(3):555–564, 1998.

[18] D. M. Heyes. *The liquid state: Applications of molecular simulations*. Wiley Publications. Wiley, New York, 1998.

[19] D. Wolf, S. R. Keblinski, and J. Eggebrecht. Exact method for the simulation of coulombic systems by spherically truncated pairwise. *Journal of Chemical Physics*, 110(17), 1999.

[20] E. E. Gdoutos, R. Agrawal, and H. D. Espinosa. Comparison of the ewald and wolf methods for modeling electrostatic interactions in nanowires. *Int. J. Numer. Meth. Engng*, 2010.

[21] P. Demontis, S. Spanu, and G. B. Suffritti. Application of the wolf method for the evaluation of coulombic interactions to complex condensed matter systems: Aluminosilicates and water. *Journal of Chemical Physics*, 114(18):7980, 2001.

[22] F. N. Mendoza, J. Lopez-Lemus, G. A. Chapela, and J. Alejandre. The wolf method applied to the liquid-vapor interface of water. *Journal of Chemical Physics*, 129(2): 24706, 2008.

[23] Q. Zhang, K. Chan, and N. Quirke. Molecular dynamics simulation of water confined in a nanopore of amorphous silica. *Molecular Simulation*, 35(15):1215–1223, 2009.

[24] D. J. Tildesley and P. A. Madden. Time correlation-functions for a model of liquid carbon-disulfide. *Molecular Physics*, 48(1):129–152, 1983.

[25] H. Stassen and W. A. Steele. Simulation studies of shear viscosity time correlation functions in liquid cs2. *Molecular Physics*, 96(8):1269–1280, 1999.

[26] M. J. Assael, J. H. Dymond, M. Papadaki, and P. M. Patterson. Correlation and prediction of dense fluid transport-coefficients .2. simple molecular fluids. *Fluid Phase Equilibria*, 75:245–255, 1992.

[27] M. J. Assael, J. H. Dymond, M. Papadaki, and P. M. Patterson. Correlation and prediction of dense fluid transport-coefficients .1. normal-alkanes. *International Journal of Thermophysics*, 13(2):269–281, 1992.

[28] C. Hoheisel. Transport-properties of molecular liquids. *Physics Reports-Review Section of Physics Letters*, 245(3):111–157, 1994.

[29] P. J. Daivis and D. J. Evans. Transport-coefficients of liquid butane near the boiling-point by equilibrium molecular-dynamics. *Journal of Chemical Physics*, 103(10): 4261–4265, 1995.

[30] R. B. Bird, R. C. Armstrong, and O. Hassager. *Dynamics of polymeric liquids,*. Vol.1. Wiley,, New York, 1987.

[31] P. J. Carreau, D. C. R. De Kee, and R. P. Chhabra. *Rheology of polymeric systems:Principles and applications*. Hanser Publications. Hanser, Munich, 1997.

[32] Guillot B. A reappraisal of what we have learnt duringg three decades of computer simulations on water. *Journal of Molecular Liquids*, 101(1):219–260, 2002.

[33] S. Balasubramanian, C. J. Mundy, and M. L. Klein. Shear viscosity of polar fluids: Molecular dynamics calculations of water. *Journal of Chemical Physics*, 106(24): 11190–11195, 1996.

[34] J. Alejandre and D. J. Tildesley. Molecular dynamics simulation of the orthobaric densities and surface tension of water. *Journal of Chemical Physics*, 102(11):4574–4583, 1994.

[35] M. A. Gonzalez and J. L. F. Abascal. The shear viscosity of rigid water models. *Journal of Chemical Physics*, 132(9):96101, 2010.

[36] J. Patravic. Molecular dynamics simulation of the orthobaric densities and surface tension of water. *Journal of Chemical Physics*, 123(17):174503–174510, 2005.

[37] K. R. Harris and L. A. Woolf. Temperature and pressure dependence of the viscosity of the ionic liquid 1-butyl-3-methylimidazolium hexafluorophosphate. *Chem. Eng Data*, 50(5):1851, 2004.

[38] A.A. Aleksandrov and M. S. Trakhtengerts. Viscosity of water at temperatures. *J. Chem. Phys.*, 27(4):660, 1973.

[39] J. Kestin, M. Sokolov, and W. A. Wakeham. Viscosity of liquid water int the range -8 ℃ to 150 ℃. *J. Phys. Chem. Ref. Data*, 7(3):941, 1978.

[40] H. Zhang and S. Han. Viscosity and density of water + sodium chloride + potassium chloride solutions at 298.15 K. *J. Chem. Eng. Data*, 41:516, 1996.

[41] S. F. Chen, R. C. Chan, S. M. Read, and L. A. Bromley. Viscosity of sea water solutions. *Desalination*, 13:37, 1973.

[42] G. Jones and S. Dole. The viscosity of aqueous solutions of strong electrolytes with special reference to barium chlorides. *J. Am. Chem. Soc.*, 51:2950, 1929.

[43] A. P. Lyubartsev and A. Laaksonen. Concentration effects in aqueous NaCl solutions. a molecular dynamics simulation. *J. Chem. Phys.*, 100(40):16410, 1996.

[44] D. E. Smith and L. X. Dang. Computer simulations of NaCl association in polarizable water. *J. Chem. Phys.*, 100(5):3757, 1994.

[45] Bahadur R., L. M. Russell, S. Alavi, S. T. Martin, and Buseck P. R. Void-induced dissolution in molecular dynamics simulations of NaCl and water. *J. Chem. Phys.*, 124:154713, 2006.

[46] Chowdhuri S. and A. Chandra. Molecular dynamics simulations of aqueous NaCl and KCl solutions: Effects of ion concentration on the single-particle, pair, and collective dynamical properties of ions and water molecules. *J. Chem. Phys.*, 115(8):3732, 2006.

[47] P. S. Crozier, D. Henderson, R. L. Rowley, and D. D. Busath. Model channel ion currents in NaCl-extended simple point charge water solution with applied-field molecular dynamics. *Bio. Phys. J.*, 81(6):3077, 2001.

[48] A. A. Chialvo, P. T. Cummings, H. D. Cochran, J. M. Simonson, and Mesmer R. E. Na^+ Cl^- ion pair association in supercritical water. *J. Chem. Phys.*, 103(21):9379, 1995.

[49] R. A. Horne. *Water and aqueous solutions.* Wiley-interscience, John Wiley & Sons Inc., 1972.

[50] J. Yang, J. Liu, J. Tong, W. Guan, D. Fang, and C. Yan. Systematic study of the simple predictive approaches for thermodynamic and transport properties of multi-component solutions. *Ind. Eng. Chem. Res.*, 49(16):7671, 2010.

[51] D. A. Muller, T. Sorsch, S. Moccio, F. H. Baumann, K. Evans-Lutterodt, and G. Timp. The electronic structure at the atomic scale of ultrathin gate oxides. *Nature*, 399:758, 1999.

[52] D. Argyris, N. R. Tummala, A. Striolo, and D. R. Cole. Molecular structure and synamics in thin water films at the silica and graphite surfaces. *J. Phys. Chem. C*, 112:13587, 2008.

[53] M. Rovere, M. A. Ricci, D. Vellati, and F. Bruni. A molecular dynamics simulation of water confined in a cylindrical SiO_2 pore. *J. Chem. Phys.*, 108:9859, 1998.

[54] Z. E. Hughes and J. D. Gale. A computational investigation of the properties of a reverse osmosis membrane. *J. Mater. Chem.*, 20:7788, 2010.

[55] P. Gallo, M. A. Rovere, and E. Spohr. Supercooled confined water and the mode coupling crossover temperature. *Phys. Rev. Lett.*, 85:4317, 2000.

[56] G. Rosengarten, H. Bhatta, and M. Sedlak. Biomimetic approaches to water purification. *Workshop Presentation*, 2007.

[57] S. Matthias and F. Muller. Asymmetric pores in a silicon membrane acting as massively parallel brownian ratchets. *Nature*, 424:53, 2003.

[58] W. Yang, P. J. Lopez, and G. Rosengarten. Diatoms: Self assembled silica nanostructures, and templates for bio/chemical sensors and biomimetic membranes. *Analyst*, 136(1):42, 2011.

[59] J. Puibasset and R. J. M. Pellenq. Grand canonical monte carlo simulation study of water structure on hydrophilic mesoporous and plane silica substrates. *J. Chem. Phys.*, 119(17):1614206, 2003.

[60] W. Humphrey, A. Dalke, and K. Schulten. *J. Mol. Graphics.*, 14:33, 1996.

[61] J. S. Babu and S. P. Sathiana. The role of activation energy and reduced viscosity on the enhancement of water flow through carbon nanotubes. *J. Chem. Phys.*, 134: 194509, 2011.

[62] D. R. Wheeler, N. G. Fuller, and R. L. Rowley. Non-equilibrium molecular dynamics simulation of the shear viscosity of liquid methanol: adaptation of the ewald sum to lees-edwards boundary conditions. *Mol. Phys.*, 92(55), 1997.

[63] S. Nose and M. L. Klein. Constant pressure molecular dynamics for molecular systems. *Molecular Physics*, 50(5):1055–1076, 1983.